

¹⁶⁶HOLMIUM POLY-L-LACTIC ACID MICROSPHERES

FACTORS CONTRIBUTING TO DEGRADATION OF $^{166}\text{HOLMIUM}$ POLY-L-
LACTIC ACID MICROSPHERES

By MACKENZIE TIGWELL, B.Sc

A Thesis Submitted to the School of Graduate Studies in Partial Fulfilment of the Requirements
for the Degree Master of Science

McMaster University © Copyright by Mackenzie Tigwell, September 2023

M.Sc Thesis – M. Tigwell: McMaster University – Department of Physics & Astronomy

MASTER OF SCIENCE (2023)

McMaster University Hamilton, Ontario (Physics & Astronomy)

TITLE: Factors Contributing to Degradation of Holmium-166 Poly-L-Lactic Acid Microspheres

AUTHOR: Mackenzie Tigwell, B.Sc. (McMaster University)

SUPERVISOR: Professor A. F. Armstrong

NUMBER OF PAGES: xii, 101

Lay abstract

This research studied Ho¹⁶⁶/PLLA microspheres, a promising treatment for tumours in the liver. The preparation of this treatment includes microspheres being neutron irradiated in the core of a nuclear reactor. Irradiation in-core leads to damage of microspheres. This research studied factors present in-core such as heat, gamma radiation, and thickness of lead shielding, for their impact on microsphere quality. Additionally, this research looked at the potential of reactive oxygen species causing damage once microspheres are suspended in liquid. Thresholds for damage were identified for temperature and gamma radiation exposure. Radiation interactions in liquid suggest possible damaging effects over time. Finally changing the thickness of lead shielding in core had significant impact on temperature, neutron flux, and microsphere quality.

Abstract

This research studied Ho^{166} /PLLA microspheres, a promising treatment for tumours in the liver. The Ho^{166} is generated through a neutron capture reaction during irradiation in a nuclear reactor. Previous work has found that neutron-irradiation in-core causes damage to microspheres and causes additional degradation to progress once suspended in media. The cause of this damage was not well understood and is the focus of this research. This research studied factors present in-core such as heat, gamma radiation, and impacts of lead shielding, for their impact on microsphere quality. Additionally, this research looked at the potential of reactive oxygen species causing damage once microspheres are suspended in liquid.

Thresholds for damage were identified to correlate with the glass transition temperature of poly-l-lactic acid. Exposure to gamma radiation induces heating, as well as structural changes to the polymer which shifts the temperature where the glass transition occurs. Damage formed from gamma radiation, independent of other variables, was seen at extreme accumulated doses. Notably, exposure to gamma radiation and heat did not cause a progression of damage over time. Samples exposed only to these factors remained stable in solution for extended periods. A theory was proposed that reactive oxygen species formed by the interaction of ionizing radiation with the suspending media may be causing the progression of damage over time. This factor would only be present for microspheres having undergone neutron capture reactions, forming radioactive holmium. Testing confirmed a potential impact of radiation interactions with the suspending media contributing to damage progression. Several thicknesses of lead shielding surrounding the sample chamber were tested in-core. There were significant impacts on temperature, neutron flux, and microsphere quality.

Acknowledgements

The research presented in this thesis would not have been possible without the support, encouragement, and mentorship of many important individuals.

Foremost I extend my gratitude to my graduate supervisor, Dr. Andrea F. Armstrong, for her incredible guidance and mentorship. Andrea has provided me with numerous unique opportunities and mentoring that will greatly impact the progression of my career. I am extremely grateful for her support and guidance over the past few years.

I would like to express my thanks for my committee members, Patrick Clancy and Kari Dalnoki-Veress. I appreciate the insights provided on my research and thesis. I know this project is of higher quality due to your involvement.

I want to thank my family for their support and encouragement. They have been an unwavering foundation for me during my graduate career. My completion of this program would not have been possible without them.

I would like to acknowledge the assistance of several groups at McMaster Nuclear Operations & Facilities. Particularly the McMaster Nuclear Reactor operators, hot cell technicians, technical services, and research & development team.

I also want to thank Lauren Mutton, an undergraduate student who volunteered to assist with data measurement.

Table of Contents

<i>Lay abstract</i>	<i>iii</i>
<i>Abstract</i>	<i>iv</i>
<i>Acknowledgements</i>	<i>v</i>
<i>Table of Figures</i>	<i>viii</i>
<i>List of Tables</i>	<i>x</i>
<i>List of Abbreviations</i>	<i>xi</i>
1. Introduction	1
1.1 Liver cancer	1
1.2 Options for treatment	1
1.2.1 Radiofrequency Ablation (RFA)	1
1.2.2 Transarterial Chemoembolization (TACE).....	1
1.2.3 Selective Internal Radiation Therapy (SIRT).....	2
1.3 SIRT Treatments	3
1.3.1 Thereasphere®.....	3
1.3.2 SIR-spheres.....	4
1.3.3 QuiremSpheres.....	4
1.4 Characteristics of QuiremSpheres	5
1.4.1 Ho-166.....	5
1.4.2 PLLA.....	5
1.4.3 Advantages over other SIRT products.....	6
1.5 QuiremSphere production	6
1.5.1 Neutron activation.....	6
1.5.2 Microsphere stability.....	7
1.6 Research objectives	8
2. Microsphere Activation and Assessment Procedures	9
2.1 Neutron Irradiation in MNR	9
2.2 Suspending Microspheres	10
2.3 Slide Preparation & Imaging	10
2.4 Damage Assessment	11
3. Investigation of the Effects of Gamma Radiation and Temperature on Microsphere Integrity	12
3.1 Introduction	12
3.2 Objectives	13
3.3 Experimental design -overview	13
3.4 Broad Sweep Test Batch	14

3.4.1 Method	14
3.4.2 Results & Discussion	15
3.5 Threshold Focused Batch.....	22
3.5.1 Method	22
3.5.2 Results & Discussion	23
3.6 Additional Tests	25
3.6.1 Short-Term Temperature Exposure.....	25
3.6.2 Dose-Rate Dependence	28
3.6.3 Prolonged Gamma Exposure.....	30
3.6.5 Thermal Analysis	31
3.7 Summary & Significance	34
4. Investigating the Role of Reactive Oxygen Species in Progression of Damage.....	35
4.1 Introduction.....	35
4.2 Objectives	35
4.3 Ho-166 MSM with Naïve Microspheres	36
4.4 Radioprotectant	39
4.5 Immediate vs. Delayed Suspension	44
4.6 Creating ROS with Co-60	46
4.7 Conclusions.....	49
5. Investigating the Impact of Shielding Thickness In-Core	50
5.1 Introduction.....	50
5.2 Apparatus & experiment design.....	50
5.3 Results	52
5.3.1 Temperature	52
5.3.2 Neutron Flux & Energy	53
5.3.3 Microsphere Activations	56
5.4 Discussion	60
5.5 Significance & Impact on Production.....	61
6. Conclusions.....	62
7. Bibliography.....	63
8. Appendix A -Data	70
Gamma-Temperature Microsphere Data.....	70
Pb Variable Thickness Rig.....	93

Table of Figures

- Figure 1.1: QuiremSpheres
- Figure 1.2: Damaged Microspheres
- Figure 2.1: Irradiation Device
- Figure 3.1: Polymer Chain Scission and Cross-Linking
- Figure 3.2: Initial Batch Experimental Variables
- Figure 3.3: Damage Levels of Control Batches
- Figure 3.4: Damage of Samples with No Gamma Exposure
- Figure 3.5: Damage of Samples with 50 kGy Gamma Exposure
- Figure 3.6: Damage of Samples with 100 kGy Gamma Exposure
- Figure 3.7: Damage of Samples with 200 kGy Gamma Exposure
- Figure 3.8: Damage of Samples with 400 kGy Gamma Exposure
- Figure 3.9: Damage of Samples with 600 kGy Gamma Exposure
- Figure 3.10: Damage of Samples with 600 kGy Gamma Exposure
- Figure 3.11: All Gamma Radiation Exposures Heated to 65 °C
- Figure 3.12: Average Damage Over Time of All Initial Samples
- Figure 3.13: Second Gamma Irradiation to 400 kGy
- Figure 3.14: Second Gamma Irradiation to 800 kGy
- Figure 3.15: Short Exposures to 60 °C
- Figure 3.16: Short Exposures to 65 °C
- Figure 3.17: Short Exposures to 70 °C
- Figure 3.18: Comparison of Temperature Damage by Exposure Time
- Figure 3.19: Comparison Damage for Different Dose Rates
- Figure 3.20: Damage by Dose Rate of 600 kGy Samples
- Figure 3.21: Flaking Microspheres
- Figure 3.22: DSC Control Results
- Figure 3.23: DSC High Dose Rate 600 kGy Results
- Figure 3.24: DSC Low Dose Rate 600 kGy Results
- Figure 3.25: DSC 1264 kGy Results
- Figure 4.1: Comparison of HoCl₃ Doped Sample Damage
- Figure 4.2: Frequency of Surface Dimpling
- Figure 4.3: Mechanical Damage of Samples with HoCl₃ with/out AA
- Figure 4.4: Mechanical Damage of Samples with HoCl₃ and (0.1-0.5M) AA
- Figure 4.5: Damage of Samples Suspended at High vs. Low SA
- Figure 4.6: Damage of Samples Suspended at High vs. Low SA
- Figure 4.7: Herniated Microsphere Damage
- Figure 4.8: Mild Ruptured Microspheres
- Figure 4.9: Severe Ruptured Microspheres
- Figure 4.10: Darkened Internal Microspheres
- Figure 5.1: Holmium Irradiation Apparatus Diagram
- Figure 5.2: Temperature Strip
- Figure 5.3: Fast Neutron Flux
- Figure 5.4: Cobalt Informed Thermal Neutron Flux
- Figure 5.5 Holmium Oxide Informed Thermal Neutron Flux
- Figure 5.6: Comparison of Thermal Neutron Flux by Pb Thickness

Figure 5.7: Microsphere Damage with 0.25 cm Pb

Figure 5.8: Microsphere Damage with 0.5 cm Pb

Figure 5.9: Microsphere Damage with 0.75 cm Pb

Figure 5.10: Microsphere Damage with 1.0 cm Pb

Figure 5.11: Microsphere Damage with 1.25 cm Pb

Figure 5.12: Achievable SA of Microspheres by Pb Thickness

List of Tables

- Table 3.1. Dose rates and accumulated dose of initial samples
- Table 3.2. Dose rates and accumulated doses of second sample set
- Table 3.3. Details of samples for dose rate testing
- Table 3.4. Sample damage comparison by dose rate
- Table 3.5. Damage assessment of 1264 kGy gamma irradiated sample
- Table 3.7. Measured glass transition temperatures
- Table 4.1 Activation products of HoCl_3
- Table 4.2 Sample concentrations of HoCl_3
- Table 4.3 Control batch material quantities
- Table 4.4. Batch makeup for samples including AA
- Table 4.5. Immediate vs. delayed suspension tests
- Table 5.1. Temperature results
- Table 5.2. Neutron flux values from CoAl wire testing

List of Abbreviations

HCC	Hepatocellular carcinoma
RFA	Radiofrequency ablation
TACE	Transarterial chemoembolization
DEB	Drug eluting beads
SIRT	Selective internal radiation therapy
TARE	Transarterial radioembolic therapy
Y-90	Yttrium-90
Ho-166	Holmium-166
PLLA	Poly-L-lactic acid
PLDA	Poly-D-lactic acid
EOI	End of irradiation
SPD	Self-powered detector
MSM	Microsphere suspension media
Co-60	Cobalt-60
AA	Ascorbic acid
DSC	Differential scanning calorimetry
T_g	Glass transition temperature
HoCl_3	Holmium chloride
SA	Specific activity

1. Introduction

1.1 Liver cancer

Malignancies in the liver are a major challenge in oncology care. Primary liver cancer was the 3rd most prevalent cause of cancer-related death in 2020 (World Health Organization, 2022). Hepatocellular carcinoma (HCC) is the most common primary cancer of the liver. This form of cancer tends to be diagnosed in late stages, limiting treatment options (American Cancer Society, 2022). It is common for cancers of the gastrointestinal tract such as rectal carcinoma to spread to the liver (Nijsen et al., 2001; M. a D. Vente, 2009). Of patients with colorectal cancer, 40-70% were found to have metastases in the liver (Wáng et al., 2015). Malignancies in the liver have high mortality rate, linked to limited effective treatment options and common late-stage diagnosis (American Cancer Society, 2022).

1.2 Options for treatment

Due to the difficulties in treating hepatocellular carcinoma, the most effective option for patients is to undergo surgery and transplant. Surgical resection is the only curative treatment option for HCC, and there are minimal life-prolonging alternative treatments (M. A. D. Vente et al., 2009). A very small percentage of liver metastases cases - approximately 10-15% - are eligible for surgical resection (Barros et al., 2014). Eligibility for surgical resection is dependent on tumor size, hepatic reserve, vascular invasion, and extrahepatic spread of the tumor. These compromising factors, in conjunction with limited donor organ supply, mean patients are typically only eligible for resection or transplant during the very early stages of HCC, well before most patients are diagnosed (Wáng et al., 2015). Unfortunately, traditional radiotherapy, chemotherapy, and immunotherapy have not been found to be effective at improving patient survival (Nijsen et al., 2001). An effective alternative treatment option is needed for patients with unresectable liver malignancies at intermediate/advanced stages (M. A. D. Vente et al., 2009).

1.2.1 Radiofrequency Ablation (RFA)

Radiofrequency Ablation (RFA) is the recommended treatment for patients with liver cancer in early stage who are not immediate candidates for surgical resection and transplant (Wáng et al., 2015). This treatment is highly effective and safe for patients who are eligible. In this treatment an electrode is introduced to the region of interest using a hollow needle and emits radio waves. The radio waves cause heating of the local tissue and induces cell death (Ikemoto et al., 2017). To minimize recurrence, a 5mm margin surrounding the tumor must be ablated. This successfully manages micrometastases and microvascular invasion present in that region. This treatment is only applicable in cases of local tumor management and can only be applied in early stages of liver cancer (Minami, 2014).

1.2.2 Transarterial Chemoembolization (TACE)

Transarterial Chemoembolization (TACE) is often presented as the first alternative treatment option for intermediate stage liver malignancies. It is only viable for patients that do not have vascular invasion, extrahepatic spread, and maintain adequate liver function (Raoul et al., 2019). This limits treatment to patients with primary liver cancer, hepatocellular carcinoma, diagnosed in the asymptomatic period (Raoul et al., 2019).

Conventional TACE is composed of intra-arterial lipiodol chemotherapy followed by embolization with Gelfoam particles. A new form of TACE utilizes drug eluting beads (DEB) containing doxorubicin, cisplatin, epirubicin or other anti-cancer drugs. DEB are non-resorbable hydrogels that are loaded in high concentrations with chemotherapy drugs (Burrel et al., 2012). Treatment is injected into artery feeding the tumor through the hepatic artery via a catheter. Microcatheters may be implemented to access small branches. The beads block blood supply to the tumor and prevent washout of the chemotherapy drugs (Wáng et al., 2015).

There are several drawbacks of TACE for treatment of liver metastasis beyond the limited number of patients who meet the eligibility criteria. The blockage of vasculature is often non-uniform and only last 72 hours. Conventional TACE has even more severe drawbacks, including the escape of chemotherapy drugs before adequate vascular blockage could be induced (Burrel et al., 2012). TACE is non-curative and only slightly increases patient survival. TACE also has the risk of treatment-induced liver failure, an extremely serious complication (Wáng et al., 2015). Additionally, TACE can stimulate neo-angiogenesis in some patients. This up-regulates local angiogenic factors and promotes regrowth of cancer tissues (Cabrera et al., 2011).

1.2.3 Selective Internal Radiation Therapy (SIRT)

Selective internal radiation therapy (SIRT) is a form of treatment that targets cancers in vivo that are not surgically removable. This is particularly amenable to malignancies in the liver. This treatment is also referred to as trans-arterial radioembolic therapy (TARE) or intra-arterial brachytherapy. Unlike surgically implanted brachytherapy sources, SIRT uses microscopic radioactive beads that are injected to the cancer site via a catheter. Although not a curative treatment, SIRT provides local tumor control, which increases the number of patients eligible for surgical resection, improves quality of life, and prolongs survival (Wáng et al., 2015).

The physiology of the liver provides a unique opportunity for SIRT. The liver is supplied with blood through two pathways, the portal vein and the hepatic artery. Healthy liver tissue receives the majority of blood via the portal vein; however, liver tumors almost exclusively are supplied via the hepatic artery (M. A. D. Vente et al., 2009). Vasculature hastily formed to support a growing tumour are structurally irregular. These vessels have larger diameter than healthy vessels (Nijsen et al., 2001). Medication to constrict vasculature is typically administered in conjunction with selective internal radiation therapy. This results in healthy liver vessels constricting but has minimal effect on cancerous vasculature. Blood flow to the tumour increases due to the resistance of constricted routes to the healthy liver tissue. At the same time, radioactive microspheres are administered directly into the liver via a catheter in the hepatic artery (de Azevedo et al., 2018), which then accumulate predominantly around the tumour. The microscopic beads become trapped in the vascular bed of the tumor, holding them in the appropriate location during treatment administration (Nijsen et al., 2001).

Selective internal radiation therapy using microspheres has two mechanisms of action: embolization, inducing hypoxia of the tissue, and radiotherapy, delivering high doses of radiation to a localized area. The blood vessels supplying the tumour are physically blocked as microspheres become lodged in the vasculature. Moreover, each microsphere contains an isotope that emits short-range radioactive particles and cause damage to nearby cancer cells (Barros et

al., 2014). This technique does not present issues prevalent in other treatments from absorption of toxic substances or damage to healthy tissue in the path of an external radiation beam (de Azevedo et al., 2018).

To prepare a SIRT therapy device, the chosen radionuclide is impregnated in microspheres made of glass or polymers. Radioisotopes that emit beta radiation are ideal candidates for in vivo radiotherapy, as they have appropriate path lengths to penetrate tissues several millimetres but no further. Beta particles damage cancerous cells through the formation of free radicals and other excited species which damage cell organelles and induce DNA strand breaks (de Azevedo et al., 2018). Several combinations of radionuclide and encapsulating material have been explored for use in SIRT for liver cancer.

Microsphere diameter must be optimized for SIRT, and early studies suggest a mean diameter of 40 μm is most appropriate. This size correlates well with the diameter of arteries being targeted and allows microspheres to reach tumor microvasculature. Microspheres of smaller diameter present issue due to distribution into non-targeted organs. Conversely, larger microspheres block vessels that are more proximal to the tumor location. This can induce particle reflux where microspheres are blocked from entering the target location and are forced to flow to untargeted tissues. Additionally, the highly localized radiation emissions are not provided at an ideal proximity to cancerous tissues. Microspheres with a diameter above 1000 μm have been shown to induce clogging of the catheter during injection (Wáng et al., 2015).

1.3 SIRT Treatments

1.3.1 Therasphere®

An early form of SIRT microspheres commercially available as TheraSphere® utilize an insoluble glass bead where yttrium-90 (Y-90) is an integral constituent of an aluminosilicate glass (Barros et al., 2014). The microspheres range in size from 20-30 microns with a mean diameter of 25 μm (Kulik et al., 2006; Wáng et al., 2015), and are suspended in a saline solution prior to injection. The microspheres concentrate in the cancerous tissue and deliver high energy beta particles. Y-90 has a 64.1-hour half-life and is exclusively a beta emitter (IAEA, 2018); its beta particles have a maximum penetration depth of 11 mm with a mean penetration of 2.25 mm (Wáng et al., 2015). TheraSphere has been used to apply SIRT in colorectal liver metastasis and HCC (Stubbs, 2021). The FDA granted TheraSphere Humanitarian Device status in 1999, and full approval for HCC and secondary malignancies in 2021 (FDA, 2021).

There are several drawbacks associated with this type of SIRT microsphere. First, the spheres will not break down in vivo due to the non-biodegradable glass form and stay in-vivo permanently. Some cases have shown migration of microspheres to other locations, including glass SIRT microspheres identified in a gastric ulcer biopsy of a patient previously treated with TheraSphere® (Arnold et al., 2019).

A bigger challenge is the difficulty with visualizing the location of the TheraSphere to ensure appropriate localization in the tumour, and to enable the clinicians to accurately calculate the dose the tumour is receiving. Once injected, Y-90 based microspheres have minimal methods for location tracing. Due to the pure-beta emission, no gamma rays can be captured to track treatment location with SPECT. Bremsstrahlung scintillation has been utilized but provides poor

image quality, not suitable for quantitative analysis (M. a D. Vente, 2009). The current standard is to use ^{99m}Tc -MAA (macro aggregated albumin) imaging for estimation of shunting to the lungs. ^{99m}Tc -MAA is a dissimilar molecule to the microspheres used in the treatment, which presents issues of accurate estimation of dose. Planar imaging of ^{99m}Tc -MAA for estimation of lung shunting was found to overestimate dose by up to 44% (Allred et al., 2018).

Finally, yttrium-90 is most easily produced through a strontium-90 radionuclide generator where the Sr-90 has been harvested from used nuclear fuel. However, for TheraSphere® the Y-90 must be generated directly through neutron irradiation of manufactured microspheres containing Y-89 (Westcott et al., 2016). Direct production of Y-90 via neutron capture of Y-89 is problematic due to very small reaction cross section, and therefore requires that TheraSphere be irradiated in a high-powered nuclear research reactor. This results in limited production capacity and high costs of Y-90 based SIRT microspheres (Hashikin et al., 2015).

1.3.2 SIR-spheres

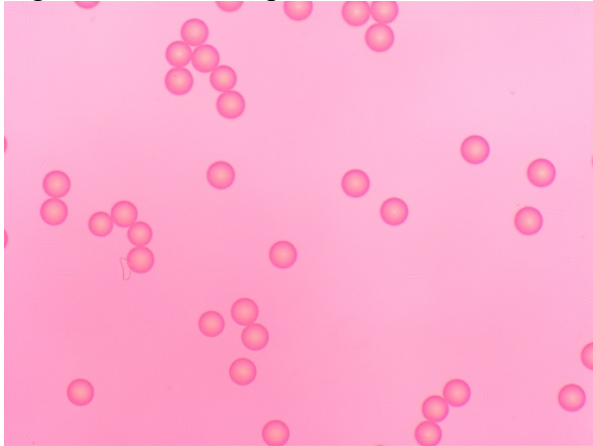
Sir-Sphere® represents a second iteration of Y-90 based SIRT microspheres to reach the market. The treatment is used to treat colorectal liver metastases (Arnold et al., 2019; Wáng et al., 2015). Unlike TheraSphere® where Y-90 is incorporated into glass, Sir-Sphere® utilize a biodegradable resin coated in Y-90 that is obtained from a $^{90}\text{Sr}/^{90}\text{Y}$ radionuclide generator, eliminating the need for a high flux nuclear reactor (Arnold et al., 2019). The diameter of these microspheres is slightly larger with an average size of 35 microns and range of 20-60 μm .

Sir-Spheres® have a lower specific activity (Bq/g) than TheraSphere® due to the smaller quantity of Y-90 present in each sphere. This requires larger numbers of microspheres to be injected to provide the same radiation dose. This increases the risk of exceeding vasculature capacity and triggering microsphere reflux (Arnold et al., 2019). There have been serious complications mainly in the form of ulceration including a life-threatening gastric ulceration from Sir-Spheres® depositing in non-targeted gastric mucosa (Sjoquist et al., 2010). These microspheres have the same restrictions on imaging in vivo as TheraSphere® making it difficult to quantitatively assess microsphere location.

1.3.3 QuiremSpheres

A more recent iteration of SIRT microspheres was developed by Quirem Medical B.V. to address the shortcomings of Y-90 based therapies. “QuiremSpheres”, a holmium-166 (Ho-166) based therapy, consist of a holmium-acetylacetonate (Ho-AcAc) core that is encapsulated within a poly-l-lactic-acid (PLLA) shell. Figure 1.1 shows a sample of QuiremSpheres suspended in liquid as seen by a light microscope. The polylactic acid makes the microspheres stable beyond the treatment period, but biodegradable over months, while having low immunoreactivity (de Azevedo et al., 2018). Rare earth metals such as holmium can accumulate in bones; by containing the holmium inside of a microsphere shell with non-absorbable material, this unwanted accumulation can be avoided (de Azevedo et al., 2018). QuiremSpheres® have an average diameter of 40 microns and a range of 20-50 μm (Nijsen et al., 2001). This is ideal to allow microspheres to embed in the tumour vasculature. Animal studies have confirmed an acceptable toxicity profile of these microspheres (M. A. D. Vente et al., 2009), with 3 clinical studies in humans complete (Reinders et al., 2022).

Figure 1.1: QuiremSpheres



Microscope image of undamaged QuiremSpheres.

In 2015, QuiremSpheres were awarded a CE mark by the European Union, and have been used in the clinic in several European countries since 2017 (Terumo, 2017). The use of Ho-166 as the treatment radioisotope in SIRT provides many benefits.

1.4 Characteristics of QuiremSpheres

1.4.1 Ho-166

The nuclear decay characteristics of Ho-166 make it a candidate for both imaging and treatment, presenting a significant advantage for selective internal radiation therapy compared to Y-90 based microspheres (Yamazaki et al., 2020). Holmium-166 decays via beta minus decay followed by occasional gamma ray emissions of 80 keV (6.51%) and 1379 keV (0.9%). This isotope has a half-life of 26.8 hours, which delivers treatment doses in a few days before decaying to stable Erbium-166. The beta minus emissions of 1.85 MeV (48.8%) and 1.77 MeV (49.9%) have a maximum range in soft tissue of 8.7 mm, which decreases the likelihood of causing damage to non-target tissues (Yamazaki et al., 2020).

1.4.2 PLLA

Poly-lactic-acid is an organic polymer that has been increasing in popularity for biomedical uses due to its biocompatibility with humans and biodegradability. It has already been explored for drug delivery systems, implants, tissue engineering, and more (Singhvi et al., 2019). In the US, the Food and Drug Administration has approved its use in biomedical applications and as such, has become a common choice to expedite new products to clinical trial.

Poly-lactic-acid has two different isomeric forms, either poly-L-lactic-acid (PLLA) or poly-D-lactic-acid (PLDA) (Tanase & Spiridon, 2014). The selection of a specific isomer or blend is connected to the desired application. The proportion of each isomer is linked to the chemical stability. PLDA breaks down significantly faster in the body than PLLA, making it unsuitable for long-term implants but highly useful in drug-release devices (Dedukh et al., 2021).

For SIRT, where microspheres must stay intact for several half-lives of Ho-166 to prevent any active fragments from dislodging from the tumor location and irradiation non-targeted tissue, a relatively stable form of PLLA is required. Thus, QuiremSpheres utilize poly-L-lactic-acid due

to the better chemical stability and higher glass transition temperature. Temperature is a critical factor due to the heating that occurs during production in-core. The glass transition temperature for PLLA occurs in the range of 60-65 °C and melting point of 160-170 °C (Androsch & Di Lorenzo, 2013; Bai et al., 2018).

1.4.3 Advantages over other SIRT products

The gamma emissions of Ho-166 can be used for nuclear imaging of tissues during treatment (de Azevedo et al., 2018) using a standard Single Photon Emission Computed Tomography (SPECT) scanner. Additionally, the paramagnetic properties of holmium make QuiremSpheres a candidate for MRI imaging (M. A. D. Vente et al., 2009). The lack of imaging was one of the major drawbacks of alternative SIRT products and allows for better treatment placement and tracking. Physicians can ensure microspheres are depositing dose in desired locations and conduct more accurate dosimetry calculations. The imageability allows small doses of microspheres to be used for eligibility assessment of patients prior to treatment. This removes the need for a dissimilar molecule such as ^{99m}Tc -MMA which is inaccurate for dose estimation.

The size of QuiremSpheres is ideal for embedding treatment in the targeted vasculature and minimizing reflux. The recent HEPAR primary clinical trial found patients received a median dose to the lungs of 1 Gy as a result of shunting. The study also found at 3 month after treatment, 19% of patients had a complete response, 35% had partial response, and 42% had stabilized disease (Reinders et al., 2022).

Like TheraSphere, the radioactive isotope Ho-166 is produced in situ. The stable isotope embedded in microspheres is holmium-165. The short half-life of Ho-166 delivers treatment doses in a few days, rather than weeks. The large cross section minimizes production time and allows for higher specific activity per sphere, reducing the total needed to deliver a dose effectively.

1.5 QuiremSphere production

Microspheres are made in Good Manufacturing Practice conditions via solvent evaporation of holmium-165. Quantities of 400-1000 mg are packaged into sterilized vials and distributed to nuclear facilities for activation. The microspheres are irradiated in a nuclear reactor to undergo neutron capture of Ho-165 which forms Ho-166 (M. A. D. Vente et al., 2009). The mass of microspheres and specific activity requested are unique to the patient who will be receiving the treatment. Activated samples for treatments are shipped to QA facilities then hospitals, while research samples are suspended and analyzed in a lab.

1.5.1 Neutron activation

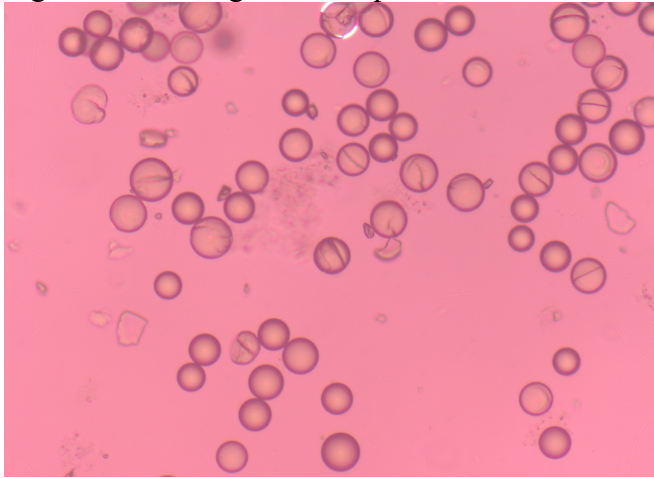
Ho-166 can be generated through neutron capture of Ho-165, which comprise 100% of naturally occurring holmium so there is no need for costly isotope enrichment (IAEA, 2018). Holmium-166 is an ideal isotope for this therapy due to the large cross section of Ho-165 ($\sigma = 64$ b), approximately 60x larger than that of Y-89 ($\sigma = 0.9$ b), making production possible even in low neutron flux facilities (Barros et al., 2014; IAEA, 2010). Specific activity suitable for patient doses (11-14 Bq/mg at administration) can be achieved in a few hours, depending on the flux of the reactor site. For example, treatments produced at the McMaster Nuclear Reactor can reach

adequate specific activity in 4-6 hours, even allowing for decay during trans-Atlantic shipping prior to patient administration.

1.5.2 Microsphere stability

Due to the organic nature of the poly-lactic-acid used to form the microspheres, the microspheres are sensitive to environmental conditions during production. Without carefully selected irradiation conditions, neutron irradiation can cause damage to microspheres leading to decomposition – breakage, leakage – that could result in harm to a patient. Damaged microspheres are shown in Figure 1.2 below. The degree of damage increases with length of irradiation and the severity of in-core conditions. This damage is caused by gamma exposure, temperature, fast neutrons, and side reactions of thermal neutron capture (M. A. D. Vente et al., 2009). Gamma exposure is of particular concern due to heating, formation of free radicals, and polymer damage.

Figure 1.2: Damaged Microspheres



Microscope image of microspheres that have been damaged during in-core irradiation.

Damage to the PLLA is dependent on irradiation conditions and length. The maximum length of irradiation in a particular activation facility is determined by the extent of damage caused to the microspheres from irradiation (M. A. D. Vente et al., 2009). Each production site is tested to characterize the specific activity of microspheres that can be produced in that location while maintaining microsphere integrity. Due to the extremely unique conditions within a production site, validation testing must be conducted for every site individually. Each production site is therefore approved to produce treatment doses to a unique maximum specific activity.

However, treatments must be produced to meet specific patient needs and treatment timelines. Each irradiation length and time is carefully calculated to account for activity decay during transport from the reactor to the patient. The specific activity at time of treatment is kept essentially constant from patient to patient; thus the required specific activity of microspheres at end of irradiation is dependent on the length of travel from the reactor to the hospital and the required activity for patient treatment (M. A. D. Vente et al., 2009). For example, a nuclear reactor that is located in close proximity to a processing/dispensing lab, that is also in close proximity to the hospital conducting the patient treatment, needs to produce a much lower

specific activity at end of bombardment compared to a facility like the McMaster Nuclear Reactor (MNR) that is supporting international (trans-Atlantic) treatments. At present, MNR is the only QuiremSpheres irradiation facility outside of Europe, typically resulting in a 48-60 h interval between end of irradiation and treatment administration; even within Europe, transport times can be > 24 h. Due to Ho-166's relatively short half-life, microspheres must be irradiated to 2-3x the activity needed for treatment, thereby increasing the length of time the microspheres must survive in the reactor core, and limiting the number of facilities that can provide these treatments.

1.6 Research objectives

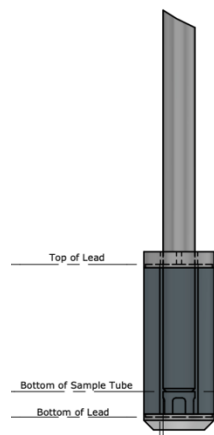
The purpose of this work is to better characterize the variables contributing to degradation of QuiremSphere during neutron activation and following suspension in biocompatible media. This understanding will allow for better informed site selection in nuclear facilities interested in producing this treatment. Additionally, this research will allow mitigation of damage through facility design choices. Several variables present in-core are being tested independently in order to gauge their relative importance, and, where possible, their interdependence. Some of these factors include gamma radiation exposure, temperature, reactive oxygen species production, and the effect of Pb shielding in-core to decrease radiation exposure.

2. Microsphere Activation and Assessment Procedures

2.1 Neutron Irradiation in MNR

Standard Ho-166/PLLA microsphere irradiation is conducted with a prepacked sample of microspheres in a polyethylene “Maria” screw-cap vial with predesignated puncture locations. Two positions in core of MNR, 9C and 9E, are validated for the neutron activation of patient treatments. A specialized irradiation device is used that holds the sample in position within an inner aluminum tube. An outer sheath of high purity lead (1.59 cm thickness) surrounds the inner tube. A diagram is provided below in Figure 2.1. A small gap between inner aluminum and outer lead allows the flow of pool water around the aluminum sample chamber, helping to cool samples during irradiation.

Figure 2.1: Irradiation Device



Technical diagram of irradiation device that holds samples while in-core

The length of irradiation is tailored to the desired specific activity of the microspheres. The activity at end of irradiation (EOI) must account for radioactive decay of samples during shipping and processing, prior to patient treatment. The flux in MNR fluctuates based on operating conditions, fuel arrangement, and the presence of additional samples. It is therefore necessary to measure the thermal neutron flux on the day of sample irradiation. This measurement can be completed with a short irradiation of a holmium oxide sample. The resultant radioactivity is measured in a standard nuclear medicine dose calibrator and used with the $^{165}\text{Ho}(n,\gamma)^{166}\text{Ho}$ reaction cross-section ($\sigma = 64 \text{ b}$) to calculate the current neutron flux in the desired position. The calculation uses Equation 1 below to solve for flux. Alternatively, a rhodium self-powered detector (SPD) can be used to measure neutron exposure. Several calibration measurements must first be taken to calculate a conversion factor between SPD measurement (in nA) and thermal neutron flux ($\text{n}/\text{cm}^2\cdot\text{s}$).

$$A = \phi\sigma N(1 - e^{-\lambda t}) \quad (1)$$

A =Activity (Bq)

ϕ = Neutron flux ($cm^{-2}s^{-1}$)

σ = Neutron capture cross section ($b = 10^{-24} cm^2$)

N = Number of target atoms

M = Molar mass (mol/g)

λ = Decay constant (s^{-1})

t = Time (s)

2.2 Suspending Microspheres

The suspension media for microspheres is a biocompatible Pluronic buffer prepared by Quirem Medical BV, hereafter referred to as microsphere suspension media (MSM). The MSM contains small quantities of phosphate and sodium.

PLLA/Ho-166 microspheres irradiated in-core were suspended as follows. A needle was inserted into one of the puncture locations. This acted as an air vent during the suspension process. A syringe fitted with a Leur-lock disposable needle was filled with 2.5-3.0 ml of MSM. This needle punctured the second location on the vial and dispensed the MSM into the vial. The liquid was syringed up and down for several minutes to mix with microspheres and break apart any chunks in the sample. This mixing took between 2-10 minutes on average, depending on the sample's rate of mixing. Once homogenously suspended in the MSM, a small aliquot was removed from the Maria vial into a 1.5 ml screwcap vial. This sample was taken to the lab for imaging and sample quality assessment. This method of suspension inside the irradiated vial was chosen to mitigate contamination risk. Dry microspheres act as a powder and are highly static, creating a high risk of external and inhaled contamination.

In the case of microspheres that underwent Co-60 irradiation and temperature testing only, a 1.5 ml screwcap vial housed the sample in lieu of a "Maria" vial. Since the Ho-165 in the microspheres had not become radioactive, less caution needed to be taken while suspending. Vial caps were unscrewed and a volume of 200-500 μ L of MSM was injected with a pipette. The mixture was then pumped with the pipette several times until the microspheres were uniformly distributed in the MSM.

2.3 Slide Preparation & Imaging

Slides were prepared by pipetting a 5 μ L aliquot of suspended microspheres onto the microscope slide. 5 μ L of additional MSM was added to distribute microspheres and improve imaging. A slide cover was placed over the 10 μ L of liquid. Samples were imaged using a Zeiss AxioCam digital microscope camera. For each sample, 5-6 images were captured with a 5x/0.13 objective lens; 8-10 images were then taken with a 10x/0.25 objective lens.

2.4 Damage Assessment

Damage was assessed visually by the author, who has several years of experience handling the QuiremSpheres and identifying damage. The total quantity of microspheres present in an image were counted with assistance of ImageJ software and manually confirmed for accuracy by the author. The microspheres with damage were then characterized and counted. Damage was reported as a percentage of total spheres. Several photos were analyzed for each sample at every timepoint, with 10-14 images selected for counting based on the need for an adequate quantity of microspheres present. Each damage assessment constituted ~250-800 microspheres being analyzed to provide adequate levels of uncertainty.

3. Investigation of the Effects of Gamma Radiation and Temperature on Microsphere Integrity

3.1 Introduction

Gamma radiation is a high energy electromagnetic wave. During irradiation in a nuclear reactor, a large spectrum of gamma radiation is present and interacts with samples. It is therefore critical to understand the impact of gamma radiation on these samples. Initial testing conducted by de Azevedo et al. exposed PDLLA-HoAcAc microspheres to 25 kGy of gamma rays from a cobalt-60 (Co-60) source. Co-60 emits pure gamma radiation, has a relatively long half-life of 5.3 years, and is readily available as a sealed source. It is a frequent choice for gamma exposure experiments. Co-60 irradiation was a proposed method for sterilization and did not present damage to the microspheres (de Azevedo et al., 2018). However, the total dose received during production is much higher than this amount and may therefore impact quality. The gamma fields are also unique to each position in-core and will vary based on core configuration, shielding, and other samples present in the surrounding area.

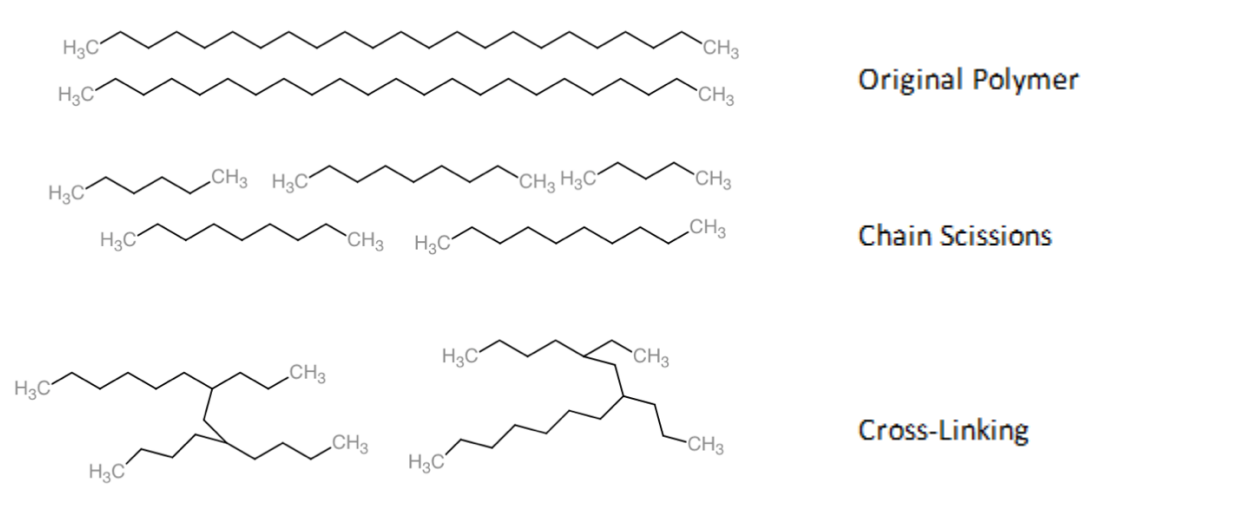
PLLA is an organic polymer that has a nanocrystalline solid form. Due to its nature, it experiences both a glass and melting transition of state. Glass transition occurs for polymers when chains are able to move past one another; increased thermal energy is the basis for this mobility. Below this temperatures materials act as a stable glass with regular crystalline structure. This is often referred to as the “plastic” state. When the temperature threshold for glass transition is reached, materials enter a viscoelastic state often referred to as the “rubber” state (Milicevic et al., 2010). Exact temperatures for phase transitions depend on polymer chain average molecular weight and isomer abundance. For PLLA the glass transition temperature has been measured to fall in the range 60-65 °C (Androsch & Di Lorenzo, 2013). The melting point occurs in the range 160-170 °C (Bai et al., 2018). Samples experience significant heating during in-core irradiations both due to gamma induced thermal heating and pool water temperatures.

Gamma radiation has been shown to induce chain scissions in polymers such as PLA. Chain scissions constitute a rupture in the C-C backbone structure of the polymer (Nascimento et al., 2011). Cutting the backbone of a polymer reduces the molecular weight, meaning the average chain length. This can cause irregularities in the crystalline structure and increase mobility of chains. Chains that can more readily slide past one another reduce the glass transition temperature and melting point of polymer materials. This process has been observed in PLLA most prominently at gamma doses below 200 kGy (Loo et al., 2005). If chain scissions occur in the microspheres, they will be more susceptible to temperature damage. Microspheres would melt at a lower temperature with chain scissions and this would impact the nuclear facilities capable of conducting neutron irradiations. Melted microspheres are not safe for treating patients since they will not properly distribute in vasculature.

Cross-linking refers to the inter-chain bonding of polymer chains and increases with gamma radiation exposure. This occurs simultaneously with chain scissions but becomes more frequent at high accumulated gamma doses. The rate of cross-linking from gamma radiation is dependent on total dose, photon energy, dose rate, and temperature during irradiation (Bednarek et al., 2020). Cross-linking occurs when chains form covalent bonds to nearby polymer segments creating a web effect, but with no addition to structural regularity. Cross-linking increases non-

uniformity in samples and chain branching (Loo et al., 2005). A visual depiction of polymer chain scissions and cross-linking is shown below in Figure 3.1. Research has suggested this effect becomes significant at doses greater than 250 kGy (Bednarek et al., 2020; Nascimento et al., 2011). Cross-linking of microspheres would delay hydrolysis and may be beneficial for increasing stability of samples during treatment. The heat-stability of microspheres during irradiation would be improved since the melting temperature increases, however the cross-linking does result in a more brittle material at room temperature.

Figure 3.1: Polymer Chain Scission and Cross-Linking



Depiction of polymer chains prior to and after chain scission or cross-linking.

3.2 Objectives

The purpose of this work is to assess the impact of gamma-induced polymer changes and temperature induced chain mobility. Both factors are present during in-core irradiations and are known to impact structure of poly-L-lactic-acid. To test the variables independent of other factors, gamma exposure was provided with a Co-60 source. Heating was separately conducted using a water bath for a length of time similar to an average irradiation. These factors were tested in conjunction due to expectation of gamma/temperature damage interdependence. This expectation is due to the structural effects on PLLA caused by gamma radiation and subsequent thermal property changes.

3.3 Experimental design -overview

These experiments sought to provide information about the effects of gamma radiation and temperature, as well as their combined effects.

Microspheres were irradiated in a 1.5 ml screw-cap vial using a ~10kCi cobalt-60 source at McMaster University. The hotcell housing the source includes several clamp stands where samples can be placed at desired radiuses from the source. The closest distance samples can be accurately placed has a dose rate of ~3.98 Gy/s. This provided gamma radiation in a range of accumulated doses and various dose rates.

Due to the extreme conditions in the reactor core it is difficult to measure accumulated gamma dose with traditional methods such as thermoluminescent dosimeters (TLD) chips. TLD chips are not suitable for detection in-core due to the high temperature. Since heat is used to un-trap electrons and discharge a measurement, the temperature in-core prevents electrons from being caught in the band gap (Donahue et al., 2012). This makes it difficult to quantify the amount of gamma radiation samples are exposed to in-core. In consequence, a wide range of gamma doses (0-800 kGy) were assessed for their impact on microsphere integrity.

The gamma dose rate was measured using a PTW model TN30010-1 ionization chamber and PTW Unidos model T10005 electrometer. During batch irradiations the samples were positioned radially from the cobalt source and irradiated for a designated amount of time. The samples received accumulated doses corresponding to their position. The dose rate received by each sample in this case was unique, relative to its position from the source. Although consistent dose rates when comparing accumulated dose would be ideal, it was not feasible due to limited availability of the Co-60 source.

Each vial was then emptied of microspheres onto a weigh paper. The microspheres were divided into 7 batches and placed into fresh vials. Temperature was applied using a hot water bath, held at a set temperature for 4 hours. One vial from each accumulated gamma dose was brought to each experimental temperature. This produced a sample with a unique combination of gamma radiation and temperature exposure. Samples were suspended in MSM and imaged at 24-hour intervals. Slides for images were prepared as described previously.

3.4 Broad Sweep Test Batch

3.4.1 Method

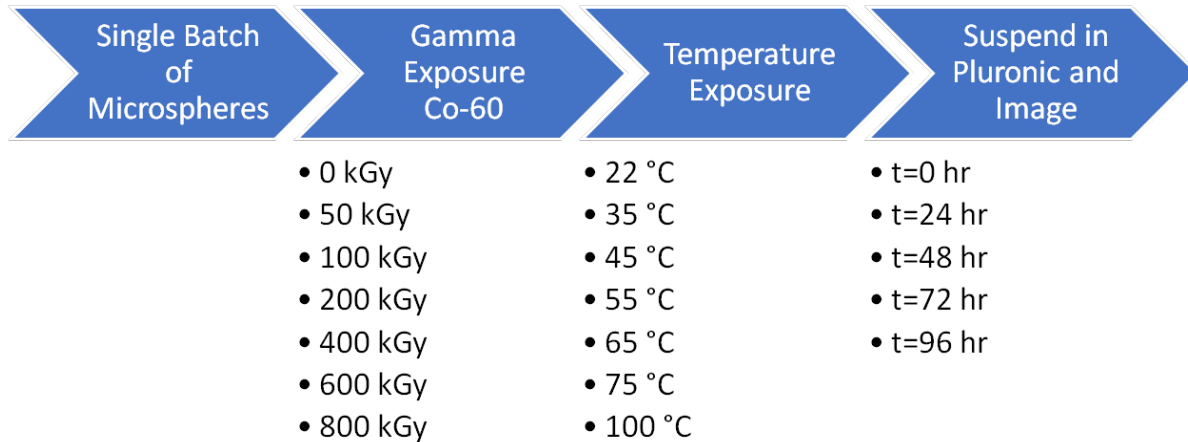
The first batch of irradiations was conducted in November 2021. This batch covered a large range of gamma exposures and temperatures to identify points of interest to be further analyzed in subsequent tests. Vials were irradiated for a fixed time of 120 hours and achieved accumulated doses of 50, 100, 200, 400, 600, 800 kGy. Dose rates were measured using PTW TN30010-1 ionizing chamber and PTW Unidos model T10005 electrometer. A control batch of microspheres with no exposure to gamma radiation was also tested along with this batch. These “0 kGy” microspheres were heated and suspended to provide data on temperature damage independent of gamma radiation. The dose rates and subsequent accumulated doses are presented in Table 3.1.

Table 3.1. Dose rates and accumulated dose of initial samples

Dose Rate (Gy/s)	Accumulated Dose (kGy)
NA	0
0.115	50
0.230	100
0.460	200
0.925	400
1.380	600
1.850	800

Samples were divided and heated to 21 (no heating applied), 35, 45, 55, 65, 75, and 100 °C for 4 hours. All samples therefore had a unique combination of gamma dose and temperature. An overview of the initial test is outlined in Figure 3.2 below.

Figure 3.2: Initial Batch Experimental Variables



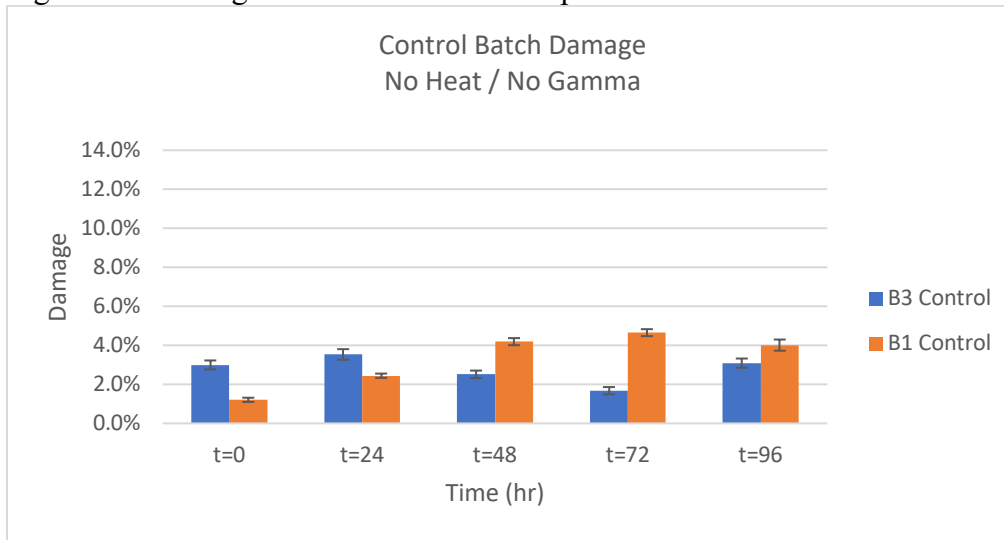
Order of microsphere testing with gamma and temperature exposures.

3.4.2 Results & Discussion

Full tables displaying sample damage, total counted, and damaged spheres is available in Appendix A -Data. Samples that received no heat exposure or gamma radiation constitute the ideal controls and provide insight into microsphere behaviour with no external impact. Data for two such samples – one from the experiment described above (“Batch 1”) and one from a subsequent experiment described in Section 3.6 (“Batch 3”) are displayed in Figure 3.3.

Samples had negligible progression of damage indicating time-dependent degradation does not occur in the 0-96 hr window when microspheres are exclusively exposed to the suspending MSM. The control samples had average damages of $3.3 \pm 0.1\%$ and $2.8 \pm 0.7\%$ during the assessment period. The minimum damage seen was $1.2 \pm 0.1\%$ and the maximum damage was $4.7 \pm 0.2\%$. Each data point represents damage assessed in 350-900 microspheres. This suggests microspheres should maintain damage levels below $\sim 4.7\%$ to constitute no impact from applied variables. Unimpacted microspheres are considered to be of adequate quality in these experiments.

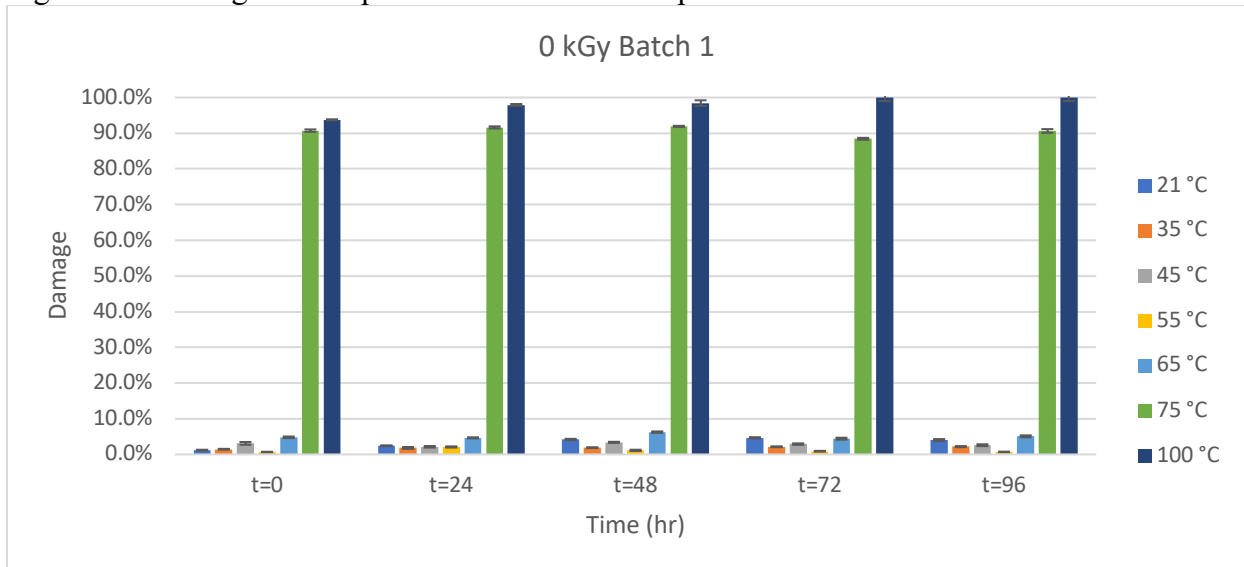
Figure 3.3: Damage Levels of Control Samples from Batches 1 and 3



Damage of naive samples suspended in MSM and assessed for 96 hours.

Sample data was tracked at 24-hour increments from suspension till 96 hours post-suspension. The data is shown organized by gamma radiation exposure in Figures 3.4-3.10 below.

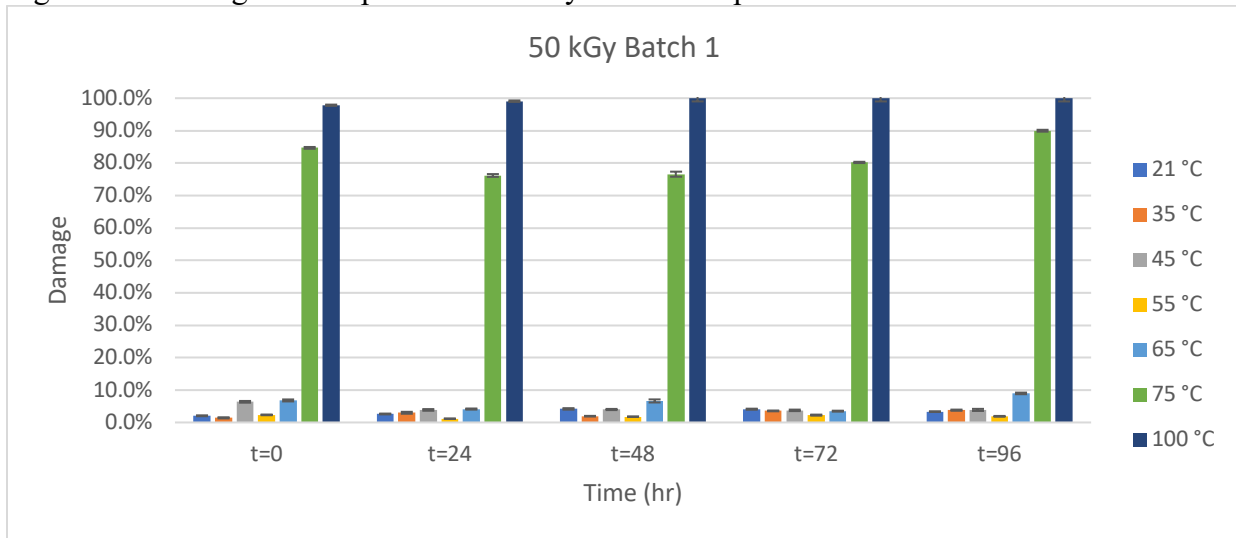
Figure 3.4: Damage of Samples with No Gamma Exposure



Damage of samples exposed to temperature only then suspended in MSM and assessed for 96 hours.

Microspheres exposed only to heating showed a drastic correlation of damage with applied temperature. The samples from 21-55 °C all remained below 4.7% damage. The 65 °C batch slightly exceeded this range and reached a maximum of $6.2 \pm 0.2\%$ which occurred at the 48-hour mark. Samples heated to 75°C and 100 °C had extreme levels of damage at all time points. There was no significant damage progression over time seen in any sample.

Figure 3.5: Damage of Samples with 50 kGy Gamma Exposure

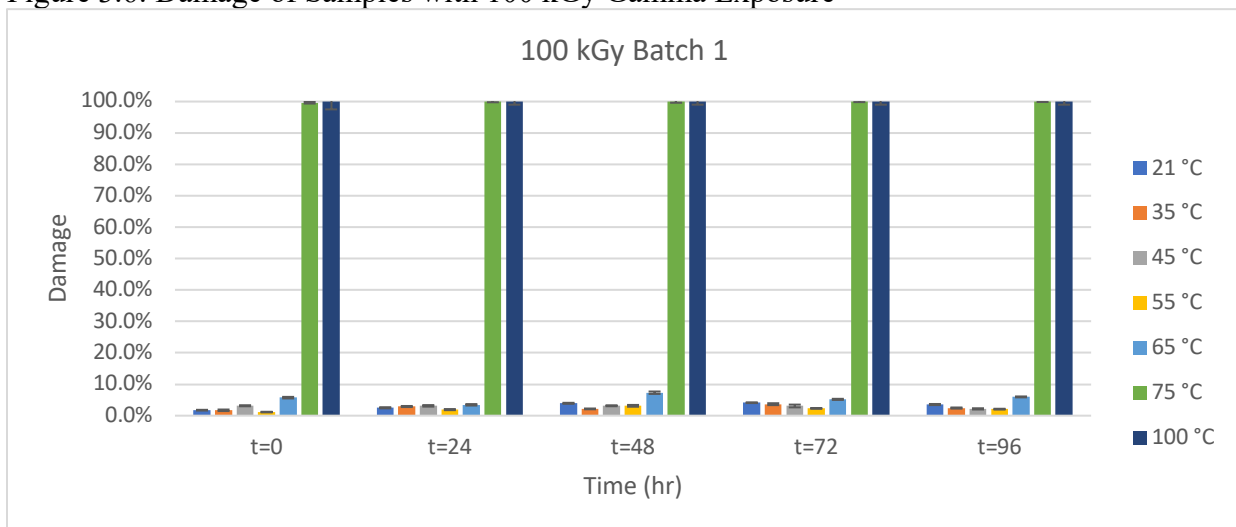


Damage of samples exposed to 50 kGy accumulated gamma radiation and temperatures up to 100 °C then suspended in MSM and assessed for 96 hours.

When exposed to 50 kGy there was no significant damage progression over time seen in any sample. Samples heated to 65 °C and above had moderate damage exceeding the 4.7% threshold. The 65 °C batch reached a maximum of $9.0 \pm 0.2\%$ which occurred at the 96-hour mark. Samples heated to 75°C and 100 °C had damage greater than 75%.

One outlier occurred in the 45°C batch at the time of suspension. The damage present was characterized at $6.4 \pm 0.3\%$ for this time check while all other data points fell below 4%. This outlier was identified as handling damage during the preparation of the slide for imaging. The sample at 45°C was therefore assumed to be adequate quality based on all other image assessments.

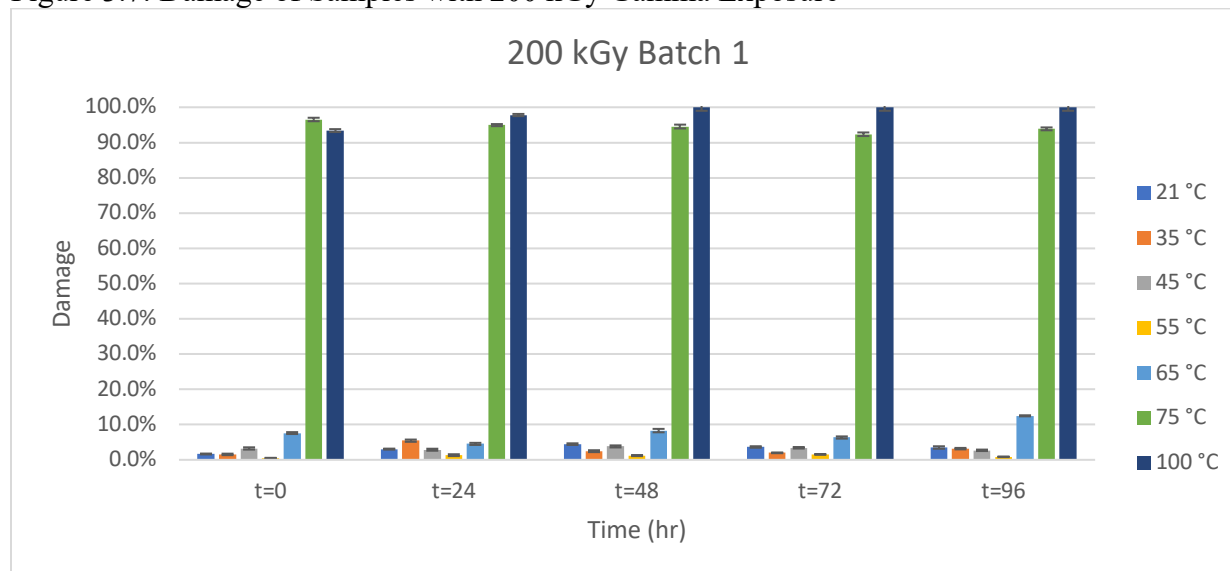
Figure 3.6: Damage of Samples with 100 kGy Gamma Exposure



Damage of samples exposed to 100 kGy accumulated gamma radiation and temperatures up to 100 °C then suspended in MSM and assessed for 96 hours.

When exposed to 100 kGy there was no significant damage progression over time seen in any sample. The samples from 21-55 °C all remained below 4.7% damage. The 65 °C batch reached a maximum of $7.3 \pm 0.4\%$ which occurred at the 48-hour mark, indicating slightly less damage than was seen in the 50 kGy samples.. Microspheres heated to 75°C and 100 °C had damage greater than 99%.

Figure 3.7: Damage of Samples with 200 kGy Gamma Exposure

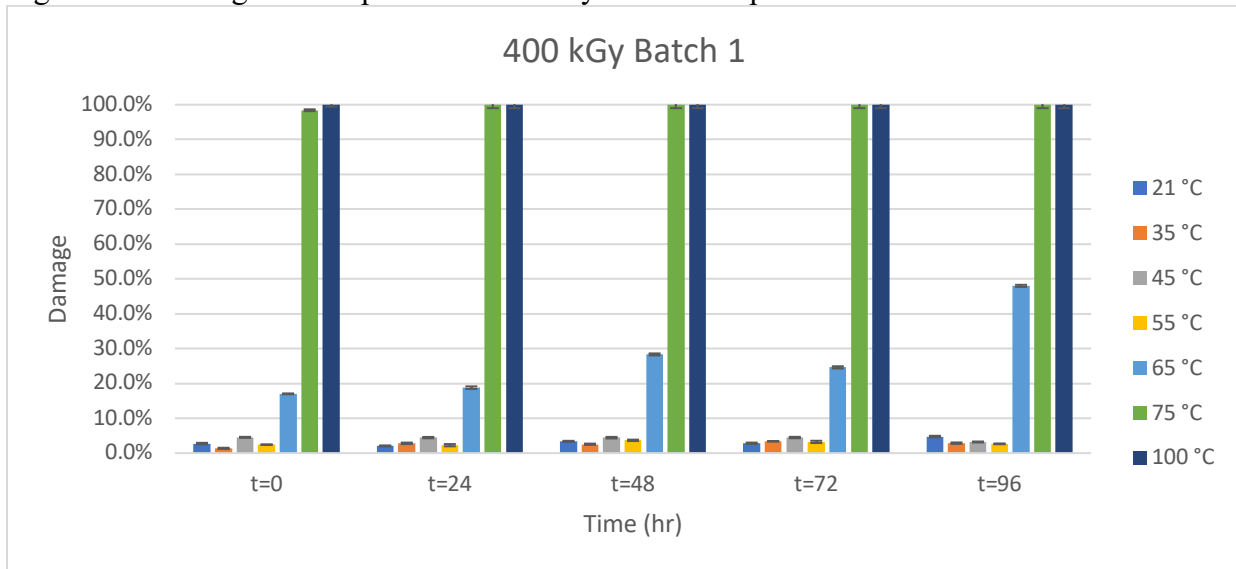


Damage of samples exposed to 200 kGy accumulated gamma radiation and temperatures up to 100 °C then suspended in MSM and assessed for 96 hours.

When exposed to 200 kGy there was no significant damage progression over time seen in any sample. Samples heated to 65 °C and above had damage exceeding the 4.7% threshold. As in the case of the 100 kGy and 200 kGy samples, the microspheres heated to 65 °C show mild to moderate damage that appears to worsen over time, reaching a maximum of $12.5 \pm 0.2\%$ damaged at the 96-hour mark. Samples heated to 75°C and 100 °C had damage greater than 92%.

One outlier occurred in the 35°C batch at the 24-hour mark. The damage present was characterized at $5.4 \pm 0.3\%$ for this time check while all other data points fall below 3.2%. This outlier was identified as handling damage during the preparation of the slide for imaging. The sample at 35°C was therefore assumed to be adequate quality based on all other image assessments.

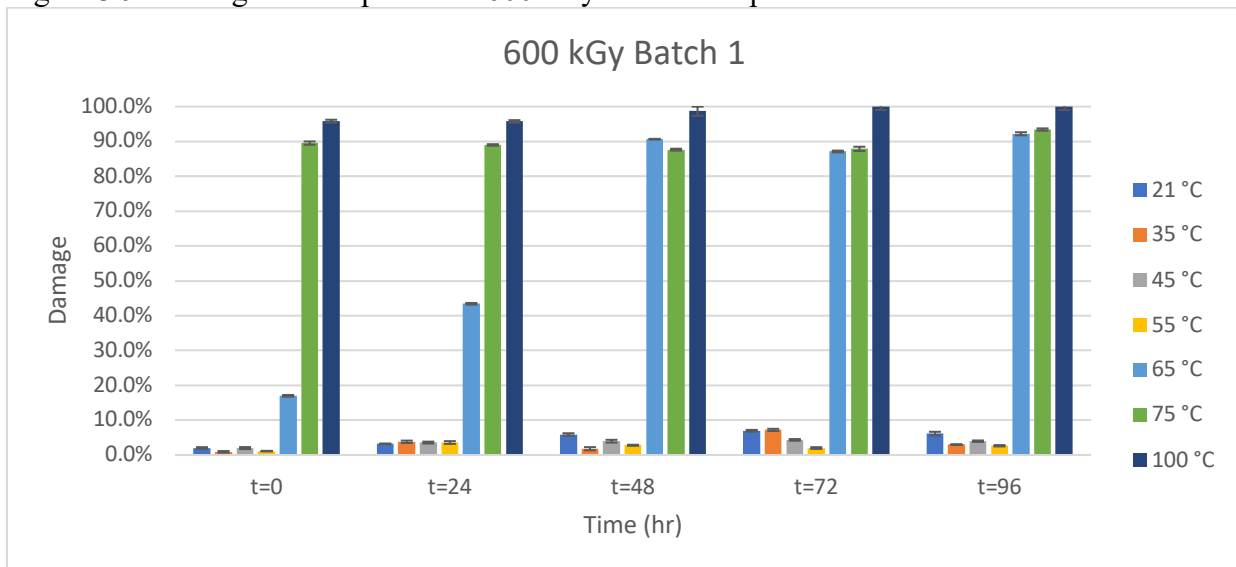
Figure 3.8: Damage of Samples with 400 kGy Gamma Exposure



Damage of samples exposed to 400 kGy accumulated gamma radiation and temperatures up to 100 °C then suspended in MSM and assessed for 96 hours.

When exposed to 400 kGy there was no significant damage progression in samples from 21-55 °C. Once again, the most interesting data comes from the samples heated to 65 °C, which displayed increasing damage during each measurement. For the first time, the 65 °C batch initially displayed substantial ($17.0 \pm 0.1\%$) damage and progressed to reach a maximum of $48.0 \pm 0.3\%$ which occurred at the 96-hour mark – significantly more damage than was seen in the 200 kGy samples. Samples heated to 75°C and 100 °C had damage greater than 98%. The samples from 21-55 °C all remained below 4.7% damage given uncertainty, clearly demonstrating that a threshold for damage exists ~ 65 °C.

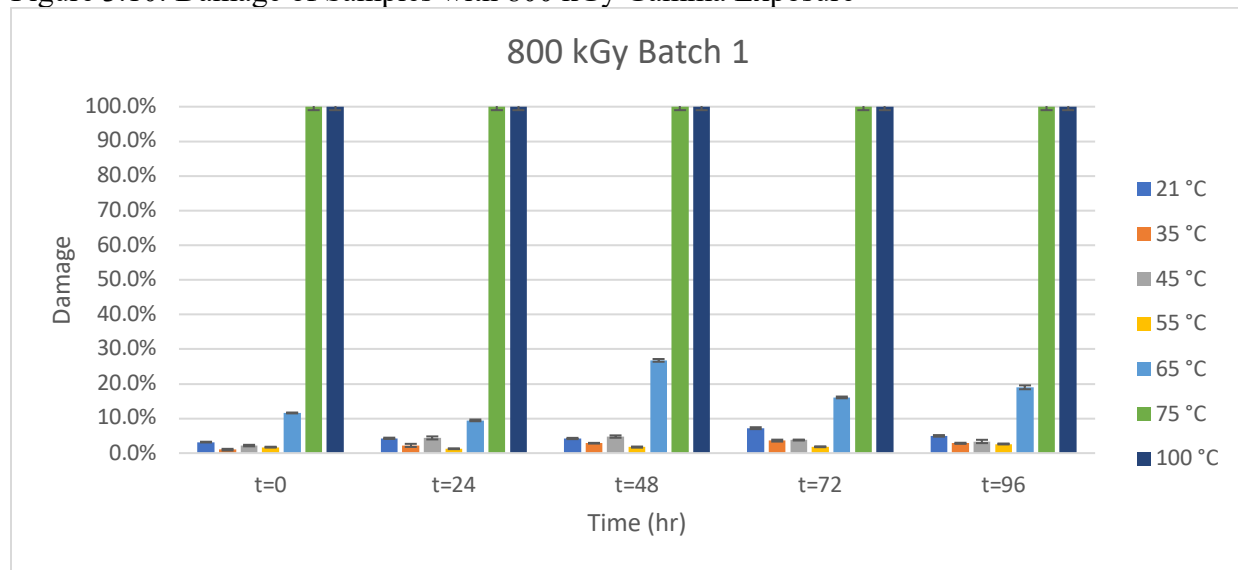
Figure 3.9: Damage of Samples with 600 kGy Gamma Exposure



Damage of samples exposed to 600 kGy accumulated gamma radiation and temperatures up to 100 °C then suspended in MSM and assessed for 96 hours.

When exposed to 600 kGy there was no significant damage progression in samples heated from 35-55 °C, with all samples remaining below 4.7% damage given uncertainty. Once again, samples heated to 65 °C displayed increasing damage over time, and increasing damage compared to the previous gamma exposure (400 kGy). The 65 °C batch initially displayed 17.0±0.2% damage and progressed to reach a maximum of 92.2±0.4% which occurred at the 96-hour mark. A slight increasing trend of damage was evident in 21 °C batch. In this batch, samples showed damage levels of 2.0±0.2%, 3.2±0.1%, 5.9±0.3%, 7.0±0.2%, and 6.2±0.5% at each time respectively. This 21 °C exceeded the threshold of 4.7% damage from 48 hours onward. As was seen throughout this experiment, samples heated to 75 °C and 100 °C had massive damage (> 87%).

Figure 3.10: Damage of Samples with 800 kGy Gamma Exposure



Damage of samples exposed to 800 kGy accumulated gamma radiation and temperatures up to 100 °C then suspended in MSM and assessed for 96 hours.

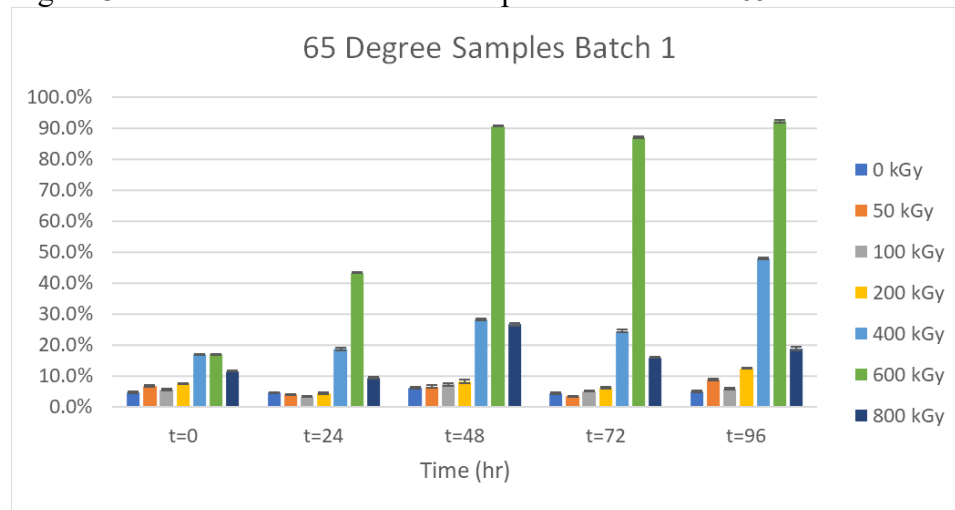
When exposed to 800 kGy there were no significant trends of damage progression over time in samples. The samples from 35-55 °C all remained below 4.7% damage given uncertainty. The 21 °C sample slightly exceeded the threshold of 4.7% damage from 72 hours onward. The 21 °C sample had damage levels of 7.0±0.3% at 72 hours and 5.0±0.2% at 96 hours. Samples heated to 75 °C and 100 °C showed damage in 100% of microspheres. However, the 65 °C batch deviated from the trends it displayed at lower gamma dosages. Rather than the microsphere quality worsening over time, the damage fluctuated from a minimum of 9.5±0.2% damage and to a maximum of 26.8±0.4% which occurred at the 48-hour mark, then declining to 16.1±0.3% and finally 19.0±0.6% at 96 hours. Moreover, while the extent of damage to the 65 °C samples increased with increasing radiation exposure from 200 kGy to 600 kGy, the percentage of microspheres damaged at 800 kGy is substantially less than what was seen at 600 kGy. This preliminary experiment revealed some important trends. Overall, samples at 55 °C and below, performed well regardless of gamma exposure. The samples at 75 °C and 100 °C had extreme levels of damage in all gamma exposures. The style of damage did present as more severe with the 400-800 kGy gamma doses.

With the exception of the 65 °C samples, the data for Batch 1 show minimal change in sample damage levels during the 96 hours. Accordingly, additional images of selected batches were captured in January 2022, over 2 months past initial suspension to better understand long-term time-dependent degradation. Samples not exposed to gamma radiation but heated to temperatures of 35, 55, and 65 °C had damage levels of $5.4 \pm 0.6\%$, $2.6 \pm 0.9\%$, and $3.7 \pm 0.5\%$ respectively – a change in damage compared to the 96 hour timepoint of +3.2%, +1.9% and -1.4%. These values show minimal change in samples over the 2-month period, and indicate that exposure to moderate temperature alone is not sufficient to cause significant time-dependent damage.

Samples exposed to the largest gamma dose of 800 kGy were also analyzed at these temperatures. Samples that received 800 kGy of dose then heated to 35, 55, and 65 °C had damage levels of $7.4 \pm 0.5\%$, $10.7 \pm 0.8\%$, and $24.0 \pm 0.6\%$ respectively at two months post-suspension, corresponding to increases of 4.6%, 8.1%, and 5.0% in the samples since the 96-hour imaging. This shows slight increases in damage during the long time period for batches exposed to extreme gamma doses, although the rate of damage formation is acceptably slow.

The data presented above demonstrate that 65 °C is a particular point of interest: accordingly, the values from all gamma exposure heated to 65 °C are presented in Figure 3.11. As described previously, across all gamma exposures the samples exceed the 4.7% damage threshold at this temperature, while the 600 kGy exposure resulted in notably more damage than all other samples including those exposed to 800 kGy. The 800 kGy sample had damage lower than both 400 kGy and 600 kGy exposures. The reason for these anomalies was not immediately apparent, though it was noted that 65 °C coincides with the glass transition temperature range for PLLA (60-65 °C).

Figure 3.11: All Gamma Radiation Exposures Heated to 65 °C

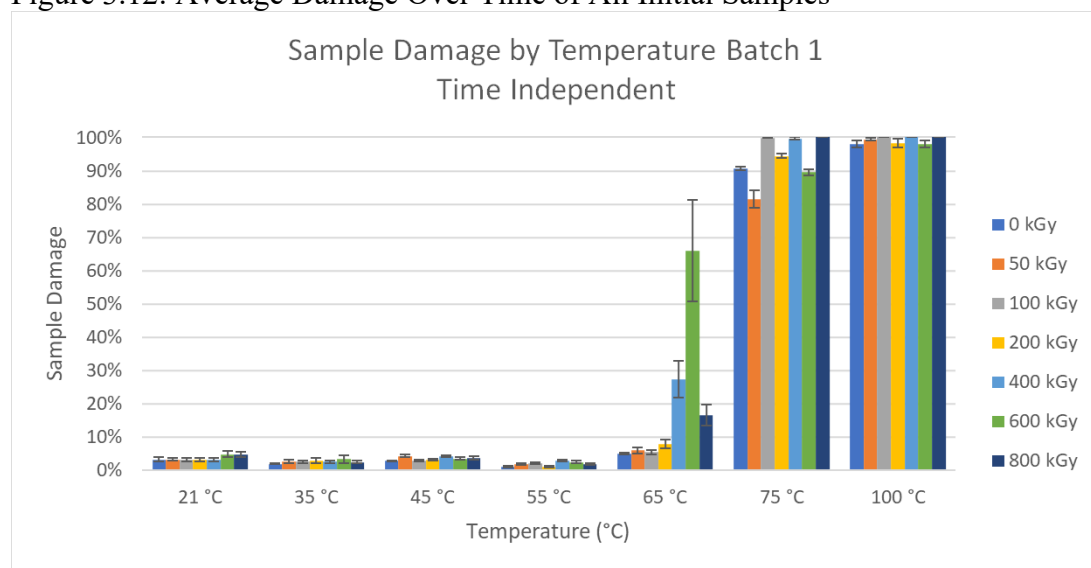


Damage of samples exposed to 0-800 kGy accumulated gamma radiation and heated to 65°C then suspended in MSM and assessed for 96 hours.

Due to minimal change in damage levels during the 96-hour window for the majority of samples, an average damage for each sample was calculated. This time-independent data allows for a better overview understanding of sample factors. This data is presented in Figure 3.12 below. The threshold for damage at 65 °C is again notable, and samples heated beyond this point have

extreme levels of damage regardless of gamma exposure. There appears to be minimal impact on damage from gamma exposure at low temperatures.

Figure 3.12: Average Damage Over Time of All Initial Samples



Average damage to samples (0-800 kGy) over the 96-hour imaging period. Temperatures range from 21-100 °C.

Representing the data in this way reinforces trends noted previously. All samples showed a damage threshold at the glass transition temperature for PLLA of 60-65°C. The severity of damage when samples were exposed to temperatures of 65°C correlated with gamma radiation exposure. The larger radiation exposures of 400-800 kGy performed significantly worse at the threshold temperature than samples with 0-200 kGy in all batches.

Low accumulated doses of radiation 50-400 kGy had no significant impact on sample damage occurrence at temperatures below the glass transition temperature. Once samples reach 65 °C all samples exceed control standards. At 65 °C samples of 0-200 kGy behaved similarly, while the 400 kGy displayed higher levels of damage than lower-dose batches.

Notably, microspheres exposed to gamma radiation for an accumulated dose of 600 kGy performed notably worse than other gamma doses in the range of 0-800 kGy. Samples at this radiation dose exceeded damage of 4.7% in samples that were exposed to no additional heat. This suggests a possible threshold for gamma exposure that should be further explored, alongside the 65 °C temperature threshold.

3.5 Threshold Focused Batch

3.5.1 Method

A second set of irradiations was conducted in September 2022 to provide data regarding points of interest identified in the initial tests. Vials were irradiated for 168 hours at 2 dose rates to achieve accumulated doses of 400 and 800 kGy. The dose rates and subsequent accumulated doses are presented in Table 3.2. These tests provided further data on the effects of high dose gamma radiation on QuiremSpheres. Batches were heated using a water-bath for 4 hours. Samples were tested at temperatures of 21 (no heating applied), 45, 55, 60, 65, 70, and 75 °C.

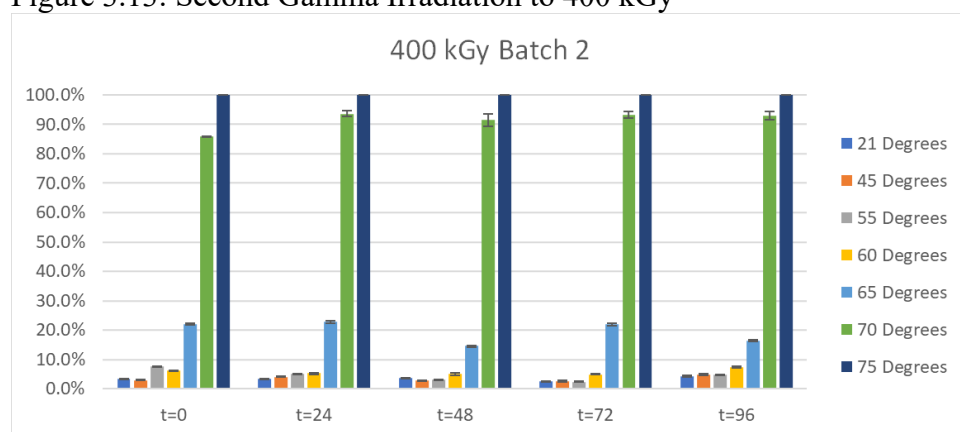
Table 3.2. Dose rates and accumulated doses of second sample set

Dose Rate (Gy/s)	Accumulated Dose (kGy)
0.662	400
1.323	800

3.5.2 Results & Discussion

This experiment focused on providing additional data on gamma doses from 400-800 kGy due to their trends previously seen in Batch 1. Temperatures focused on the range near 65 °C to better understand this threshold. Microsphere quality was tracked at 24-hour increments from suspension till 96 hours post-suspension. The data is shown organized by gamma radiation exposure in Figures 3.13-3.14 below.

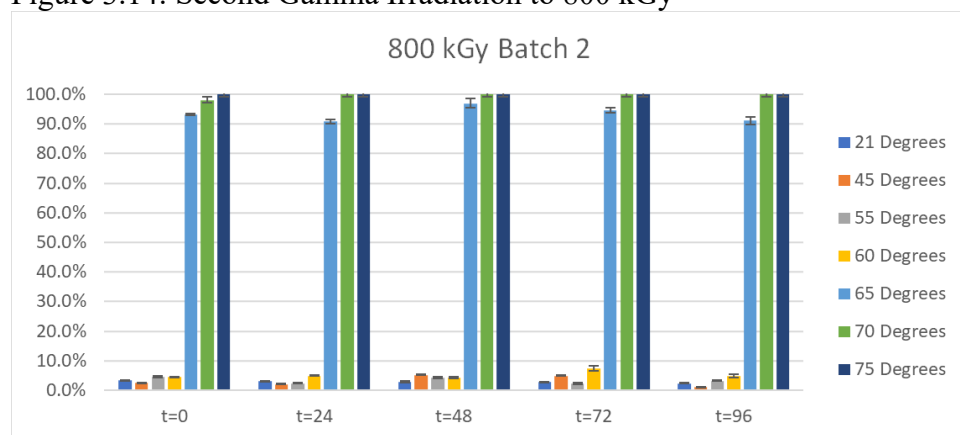
Figure 3.13: Second Gamma Irradiation to 400 kGy



Damage of samples exposed to 400 kGy accumulated gamma radiation and temperatures up to 75 °C then suspended in MSM and assessed for 96 hours.

At 400 kGy samples did not show any significant trends of increasing damage in samples over time. The samples at 21 and 45 °C remained below 4.7% damage at all time-points, as was seen for low-temperature samples in Batch 1. In this batch the 55 °C slightly exceeded the 4.7% threshold for damage at t=0 and t=24 with damage values of $7.6 \pm 0.1\%$ and $5.0 \pm 0.1\%$ respectively. By 60 °C samples ranged in damage from $5.0 \pm 0.3\%$ to $7.4 \pm 0.3\%$ during measurements. This slightly exceeds the 4.7% threshold but visually looks extremely close to acceptable quality, suggesting that the crucial temperature threshold for microsphere viability is above 60 °C. At 65 °C samples are significantly beyond the acceptable value and fluctuate in the range of $14.6 \pm 0.3\%$ to $22.8 \pm 0.4\%$. At 70 °C and 75 °C samples have damage in greater than 85% of microspheres, as was seen for ≥ 75 °C samples in Batch 1.

Figure 3.14: Second Gamma Irradiation to 800 kGy



Damage of samples exposed to 800 kGy accumulated gamma radiation and temperatures up to 75 °C then suspended in MSM and assessed for 96 hours.

The 800 kGy samples showed a significant change from the microspheres exposed to only 400 kGy. In this data set, all samples exposed to $T \geq 65$ °C showed severe damage (> at 65 °C; > 98% at 70 °C and 75 °C). When compared to the 400 kGy/65 °C sample, the 800 kGy/65 °C sample provides clear evidence for an interaction between temperature exposure and gamma exposure that causes degradation of the microspheres, presumably because of radiation-induced chain scissions that lower the melting point of the PLLA.

It is interesting to compare the results of this second 800 kGy/65 °C sample (Figure 3.14) with the damage exhibited in the Batch 1 samples exposed to 600 kGy/65 °C (Figure 3.9) and 800 kGy/65 °C (Figure 3.10). Based on the results from Batch 1 (Figure 3.10), which had the same temperature and gamma radiation exposure as the Batch 2 sample presented in Figure 3.14 – but instead, the catastrophic damage in Figure 3.14 is much more consistent with what is seen for the 600 kGy sample from Batch 1 (Figure 3.9). The reason for this is not immediately obvious; however, it may be noteworthy that the two 65 °C samples showing massive damage (Batch 1, 600 kGy, Figure 3.9; Batch 2, 800 kGy, Figure 3.14) were both irradiated with a dose rate of ~ 1.3 Gy/s (see Tables 3.1 and 3.2), while the largely intact microspheres of Figure 3.10 (Batch 1, 800 kGy) experienced a significantly higher dose rate of 1.85 Gy/s.

The 800 kGy samples did not show any significant trends of increasing damage in samples over time. The samples at 21 and 55 °C remained below 4.7% damage at all timepoints, while the 45 °C batch marginally exceeded the 4.7% threshold for damage at $t=48$ and $t=72$ with damage values of $5.3 \pm 0.2\%$ and $5.0 \pm 0.2\%$ respectively. Curiously, the 60 °C samples showed mild damage from $4.4 \pm 0.1\%$ to $7.4 \pm 0.8\%$ during measurements – similar to what was seen in the 400 kGy samples, despite the extensive destruction of the 65 °C sample at 800 kGy. .

These measurements aimed to specify the temperature threshold for damage. It was seen that at 60 °C, samples begin to show damage in excess of control batches. The additional damage at this temperature was found to be only marginally above the control value. At 65 °C the damage formation was visibly distinguishable from control quality when exposed to 400 kGy, but was catastrophic when exposed to 800 kGy. By 70 °C, samples experienced severe damage

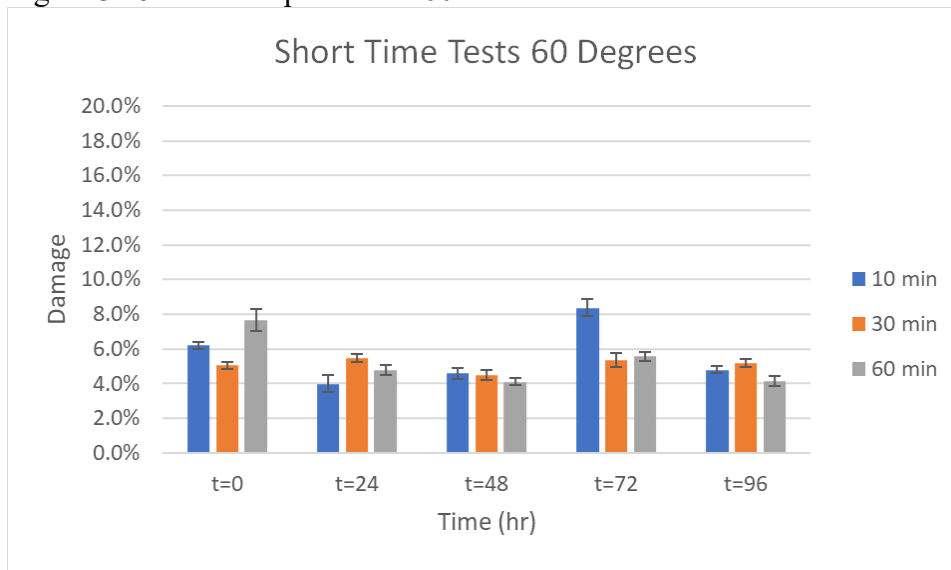
regardless of gamma dose received. This narrowed the damage threshold for temperature-induced degradation to 60-65 °C. Above 60 °C samples that received greater gamma exposure performed notably worse than lower gamma dose batches. This implies gamma-induced chain scissions are lowering thresholds for temperature-related damage.

3.6 Additional Tests

3.6.1 Short-Term Temperature Exposure

Additional tests were completed to complement the findings from previous batches and further study regions near damage thresholds. An experiment was designed to test the potential impact of microspheres exposed to temperatures near the damage threshold for short periods of time, during non-standard operations. To further assess the impact of temperature exposure on microsphere integrity, tests were completed with naive microspheres exposed to 60, 65, and 70 °C for short periods of time. These samples received no gamma radiation exposure. The samples were heated in a water bath for 10 minutes, 30 minutes, or 1 hour. The data from short temperature exposures are presented in Figures 3.15-3.17. The damaged percentage is displayed on a 0-20% axis rather than 0-100% axis to magnify any trends present.

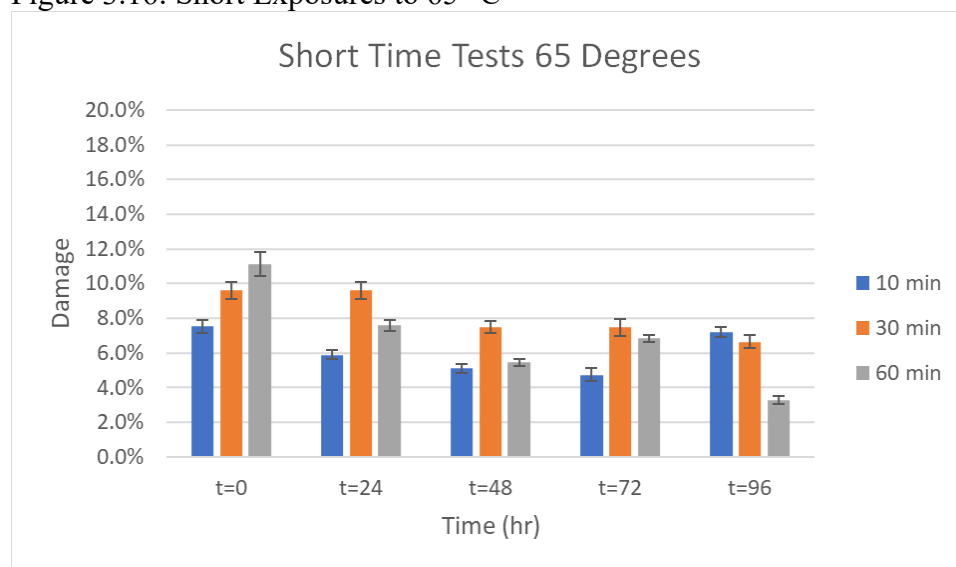
Figure 3.15: Short Exposures to 60 °C



Damage of samples exposed to 60 °C for (10 min, 30 min, 1 hour) then suspended in MSM and assessed for 96 hours.

When exposed to 60 °C all samples exceeded the 4.7% damage threshold during three or more timepoints. There was no trend identified for increased damage with increased length of temperature exposure in these samples. The average damage over time for 10 min, 30 min, and 60 min exposure was $5.6 \pm 1.7\%$, $5.1 \pm 0.3\%$, $5.2 \pm 1.4\%$ respectively. The range of uncertainty for each batch overlaps, indicating that there is no statistically significant difference in heat-induced damage for these short exposure times.

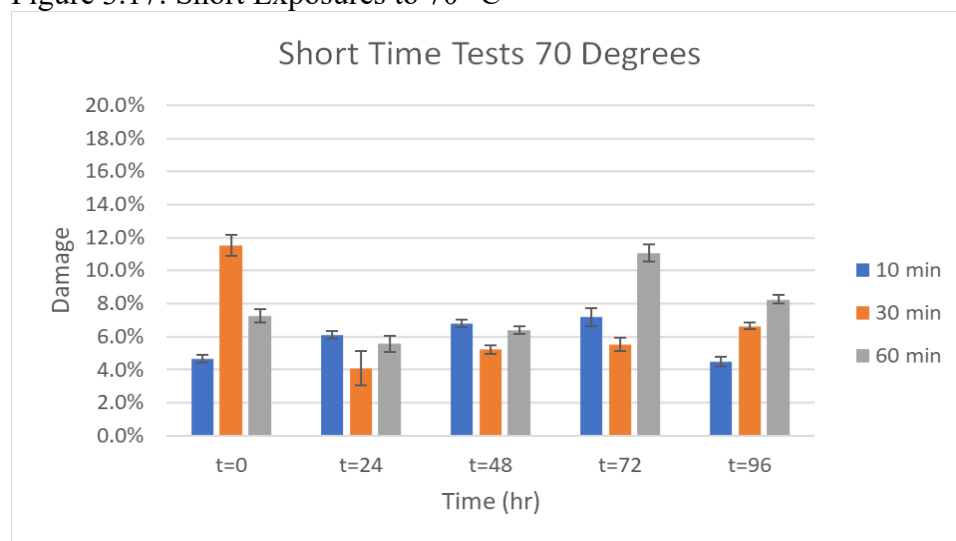
Figure 3.16: Short Exposures to 65 °C



Damage of samples exposed to 65 °C for (10 min, 30 min, 1 hour) then suspended in MSM and assessed for 96 hours.

When exposed to 65 °C all samples exceeded the 4.7% damage threshold. There was no trend identified for increased damage with increased length of temperature exposure in these samples. This further shows that temperature independent of other variables is not responsible for degradation over time. The average damage during the testing window for 10 min, 30 min, and 60 min exposure was $6.1 \pm 1.2\%$, $8.2 \pm 1.3\%$, $6.8 \pm 2.9\%$ respectively. The range of uncertainty for each batch overlaps, suggesting the severity of damage does not worsen at 65 °C with length of exposure. Additionally this data shows that 65 °C cannot be tolerated by microspheres even for very short period and must not occur at all during microsphere production, neutron irradiation, suspension, or administration.

Figure 3.17: Short Exposures to 70 °C

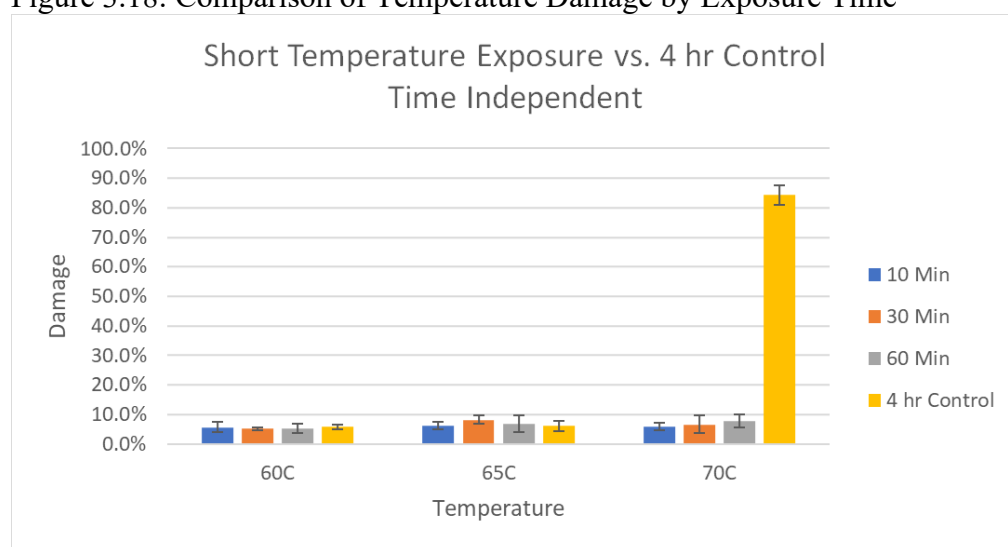


Damage of samples exposed to 70 °C for (10 min, 30 min, 1 hour) then suspended in MSM and assessed for 96 hours.

When exposed to 70 °C all samples exceeded the 4.7% damage threshold. This batch had significant fluctuation in damage for each sample during imaging. Trends are difficult to assess due to this. The average damage for 10 min, 30 min, and 60 min exposure was $5.8 \pm 1.2\%$, $6.6 \pm 2.9\%$, $7.7 \pm 2.1\%$ respectively. The range of uncertainty for all batches overlap. Statistics regarding the average for the 30-minute sample become skewed by the $t=0$ outlier which has damage 4.9% higher than the second greatest value in this sample.

The damage present in all samples was graphed along with a control sample heated for the standard 4 hours. The time-averaged values are presented below in Figure 3.18. The control shows similar levels of damage at 60 °C and 65 °C but by 70 °C the control sample damage is notably greater than any short heating test.

Figure 3.18: Comparison of Temperature Damage by Exposure Time



Average damage over 96 hours of samples exposed to 60-70 °C for (10 min, 30 min, 1 hour) then suspended in MSM and assessed.

At 60 °C all samples occur in the range of uncertainty of the control batch. At 65 °C the range of uncertainty overlaps for all samples. This suggests no significant effects at these two temperatures from length of exposure.

At 70 °C the average damage at 10 minutes, 30 minutes, 60 minutes, and 4 hours increases with values of $5.8 \pm 1.2\%$, $6.6 \pm 2.9\%$, $7.7 \pm 2.1\%$, and $84.3 \pm 3.2\%$ respectively. This suggests length of exposure at 70 °C does have an impact on sample damage since exposures below 60 minutes were tolerated significantly better than 4 hours.

Even for short exposures of as little as 10 minutes to temperature slightly above the glass transition, the damage present in samples exceeded that of control samples. This represents a significant and intolerable threshold for temperature-induced damage. This helps explain why Batch1/65 °C had increased damage with greater doses of gamma radiation. For greater gamma exposures, even minor differences in chain scissions reduce the glass transition enough to significantly worsen temperature effects. These findings reiterate that facilities conducting

neutron irradiations, where temperature exposure is most likely to occur, must carefully avoid temperature fluctuations that would exceed this threshold, even if excursions are short lived.

3.6.2 Dose-Rate Dependence

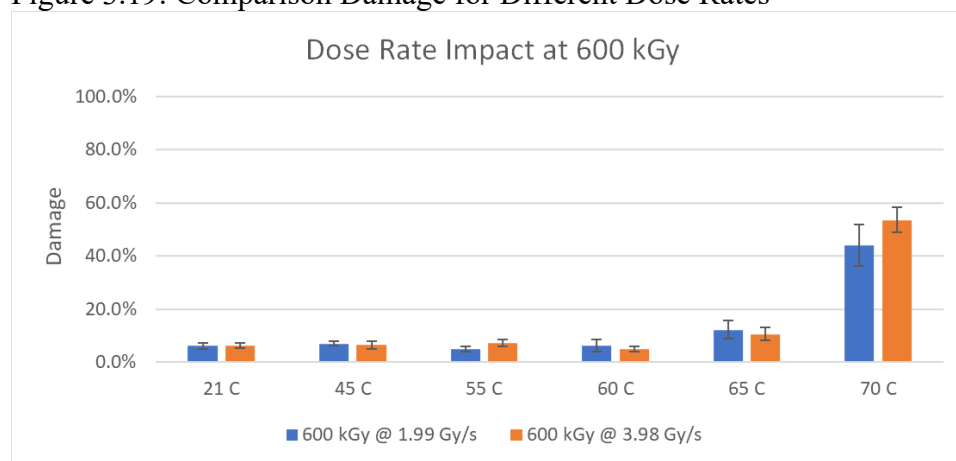
A third set of Co-60 irradiations were conducted to test the potential dose rate dependence of sample damage. This mainly focused on samples irradiated to an accumulated dose of 600 kGy due to a possible threshold identified in the previous testing. The first 600 kGy sample displayed time-dependent damage at 65 °C and performed worse than the Batch 1 800 kGy. The difference between Batch 1 and Batch 2 800 kGy is very notable and may be explained by a dose rate impact on the ratio of chain scissions to cross-links. To check the impacts of dose rate on sample damage, two samples were irradiated to a total accumulated dose of 600 kGy with significant differences in dose rate. These samples were further compared with previous 600 kGy sample from the original test batch. The dose rates for each sample are indicated in Table 3.3.

Table 3.3. Details of samples for dose rate testing

Dose Rate (Gy/s)	Total Dose (kGy)	Irradiation Batch
3.98	~600	Batch 3A
1.99	~600	Batch 3B
1.38	~600	Batch 1

The resulting damage is presented below in Figure 3.19. The average damage for each temperature has an overlapping range of uncertainty between the two dose rates tested. No trends of increasing damage over the 96-hour window were statistically significant. Rather all samples fluctuated, but more significant fluctuation ranges occurred in samples heated to higher temperatures. There is no significant trend in damage linked to the dose rate when tested at the aforementioned dose-rates.

Figure 3.19: Comparison Damage for Different Dose Rates



Average damage over 96 hours for samples exposed to 600 kGy total accumulated dose from gamma radiation, achieved with different dose rates then suspended in MSM and assessed at room temperature.

At all temperatures tested both samples exceed the 4.7% damage threshold. This occurs even at 21 °C when no heating is applied. This contrasts the Batch 1 irradiation to 600 kGy (1.38 Gy/s)

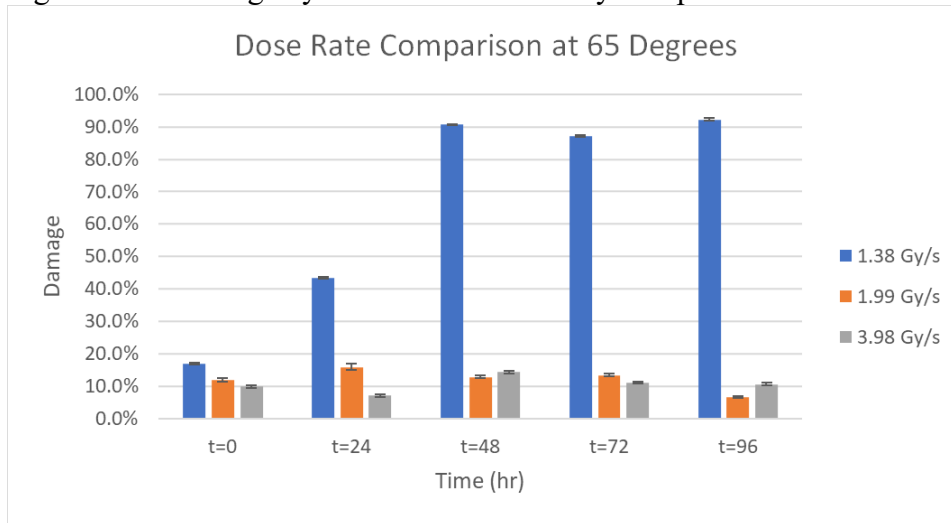
where samples at 35-55 °C maintain damage levels below 4.7%. The temperatures 21, 45, and 55 °C are shown below in Table 3.4.

Table 3.4. Sample damage comparison by dose rate

Temperature	1.38 Gy/s	1.99 Gy/s	3.98 Gy/s
21 °C	4.9±2.1%	6.1±1.1%	6.2±1.0%
45 °C	3.6±0.9%	6.9±0.8%	6.4±1.4%
55 °C	2.4±0.9%	4.9±0.9%	7.1±2.6%

The lowest dose rate performs better at lower temperatures, but this trend does not continue at the threshold temperature of 65 °C. The data set for each dose rate at 65 °C is presented in Figure 3.20 below.

Figure 3.20: Damage by Dose Rate of 600 kGy Samples



Damage of samples exposed to 600 kGy total accumulated dose from gamma radiation, achieved with different dose rates then suspended in MSM and assessed for 96 hours at room temperature.

At this temperature there is a trend of increasing damage only in the lowest dose-rate sample. The lower dose rate also has significantly greater levels of damage when heated to this temperature. This suggests a possible protective effect from cross-linking induced at higher dose rates, as cross-linking is known to occur more frequently at higher dose rates. Due to the increase of the glass transition temperature for cross-linked polymers, this effect could make microspheres more resistant to temperature exposure, particularly the 65 °C threshold. The possibility of increased cross-linking at higher dose rates may also explain the Batch 1 data set that showed microspheres heated to 65 °C survived better when exposed to 800 kGy (at 1.85 Gy/s) compared to 600 kGy (at 1.32 Gy/s).

Additional testing of dose rates to achieve 600 kGy were conducted and showed samples exposed 1.99 Gy/s and 3.98 Gy/s presented similar in levels of damage in samples. There was no significant difference between the damage levels at these dose rates. The original dose rate of 1.38 Gy/s from Batch 1 irradiation performed marginally better at low temperatures. However, 600 kGy samples heated to 65 °C performed worse with a slower rate of gamma exposure. This

suggests there is some cross-linking occurring with higher dose rates but not significant enough to overcome the damage induced by chain scissions, which exceeds acceptable levels and is therefore not useful in producing samples of treatment quality.

3.6.3 Prolonged Gamma Exposure

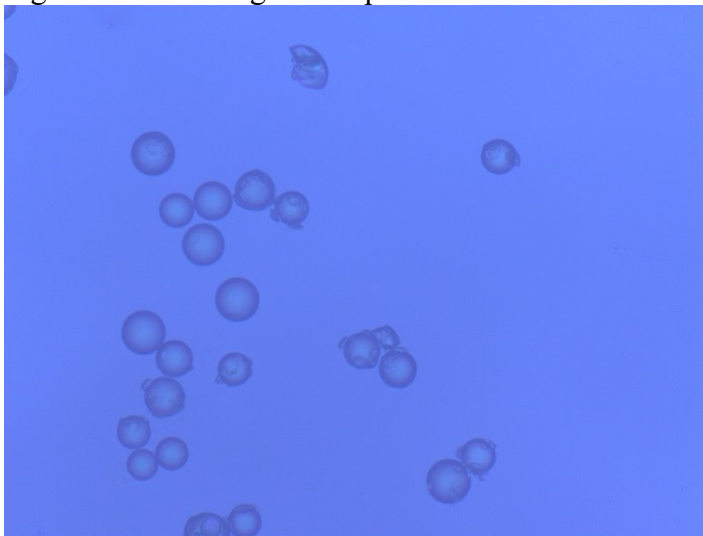
A sample was irradiated to an ultra-high accumulated gamma dose to provide trend information on accumulated gamma dose impacts. A single sample was irradiated with the Co-60 source to an accumulated gamma radiation dose of 1264 kGy at a dose rate of 1.05 Gy/s. The microspheres were suspended and imaged at room temperature; no heat was applied to test gamma induced damage exclusively. The sample was imaged from 0-48 hours only. No imaging was conducted past 48 hours due to the severe damage present in the sample. The data is presented in Table 3.5 below.

Table 3.5. Damage assessment of 1264 kGy gamma irradiated sample

21 C / 1264 kGy	Total	Damaged	Damaged Fraction	Uncertainty
t=0	329	35	10.6%	0.003
t=24	188	135	71.8%	0.005
t=48	87	71	81.6%	0.01

There is a significant increase in damage from suspension to each imaging point. The damage that developed was unique in style. An image from t=24 is below as Figure 3.21. The formation of damage appeared like segmentation of layers in microspheres and significant flaking sections.

Figure 3.21: Flaking Microspheres



Unique damage form showing flaking of PLLA coating.

When suspended the sample immediately had damage more than double that of the control levels. The damage rapidly progressed and by 48 hours had reached 81% damage. The damage presented uniquely as severe peeling on the surface of microspheres. This clearly shows that gamma radiation at extreme doses can impact quality independent of other variables.

3.6.5 Thermal Analysis

Differential Scanning Calorimetry (DSC) was performed on four microsphere samples to characterise the glass transition temperature (T_g) of the PLLA coating and identify any shifts of T_g based on radiation exposure. Three microsphere samples exposed to different gamma radiation doses were selected along with a control non-irradiated batch. This thermal analysis was conducted on a DSC Q100 V9.9 Build 303 at the Brockhouse Institute for Materials Research at McMaster University using a thermal range of 0-100 °C at a scan rate of 10 °C/min. The samples tested are outlined below in Table 3.6.

Table 3.6. Samples undergoing differential scanning calorimetry

Total Dose (kGy)	Dose rate (Gy/s)	Name
0 (control)	NA	Control
600	3.98	High Dose Rate 600 kGy
600	1.99	Low Dose Rate 600 kGy
1264	1.05	Prolonged Gamma Sample

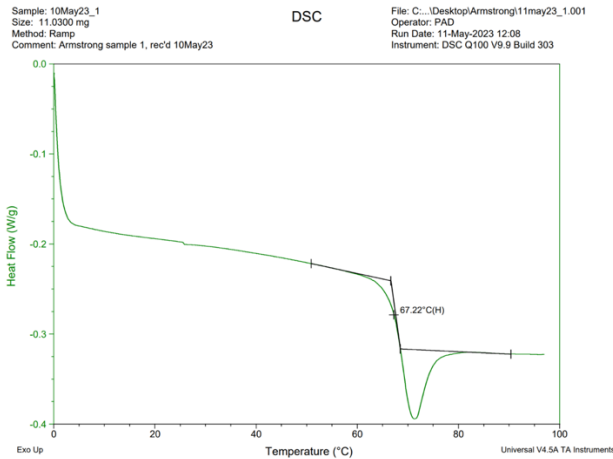
The glass transition temperature for each sample was determined using the half-height method by staff scientists at the Brockhouse Institute for Materials Research. The thermal data for each microsphere sample are presented below as Figures 3.22-3.25, while their empirically determined glass transition temperatures are listed in Table 3.7.

Table 3.7. Measured glass transition temperatures

Total Dose (kGy)	Dose rate (Gy/s)	Name	Glass Transition Temperature °C
0 (control)	NA	Sample 1	67
600	3.98	Sample 2	58
600	1.99	Sample 3	59
1264	1.05	Sample 4	54

There is a trend of decreasing glass transition temperature with increased gamma radiation exposure. The difference from samples with no gamma exposure to the sample exposed to 1264 kGy is ~13 °C.

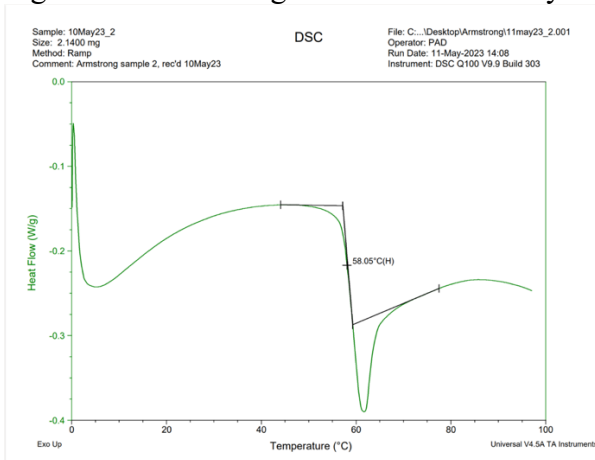
Figure 3.22: DSC Control Results



Differential scanning calorimetry results for naive microspheres.

Control samples of naive microspheres show a transition temperature of 67.2 °C.

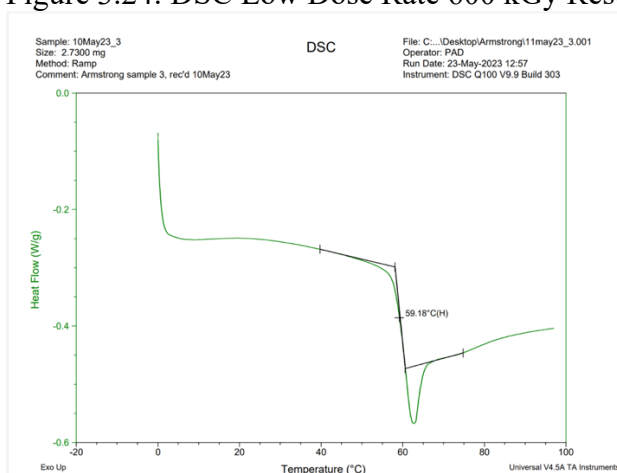
Figure 3.23: DSC High Dose Rate 600 kGy Results



Differential scanning calorimetry results for microspheres irradiated to 600 kGy at 3.98 Gy/s.

Samples exposed to 600 kGy at 3.98 Gy/s have a transition temperature of 58.0 °C.

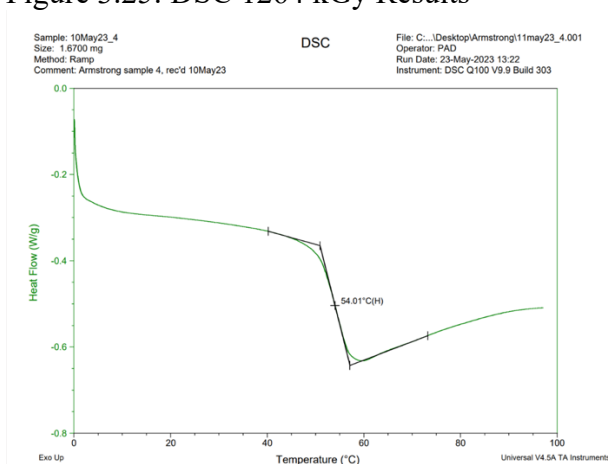
Figure 3.24: DSC Low Dose Rate 600 kGy Results



Differential scanning calorimetry results for microspheres irradiated to 600 kGy at 1.99 Gy/s.

Samples exposed to 600 kGy at 1.99 Gy/s have a transition temperature of 59.2 °C.

Figure 3.25: DSC 1264 kGy Results



Differential scanning calorimetry results for microspheres irradiated to 1264 kGy at 1.05 Gy/s.

Samples exposed to 1264 kGy at a dose rate of 1.05 Gy/s have a transition temperature of 54 °C.

Thermal analysis found the glass transition temperature for the poly-l-lactic-acid coating of the microsphere decreased for samples exposed to larger doses of gamma radiation. Samples at 600 kGy had a T_g more than 8 °C below the control. The sample at 1264 kGy of exposure had an even lower transition temperature, 13 degrees below the control. This suggests major changes in the polymer structure of microspheres when exposed to radiation. The decrease in T_g shows that chain-scissions, rather than cross-linking, is the predominant interaction occurring during gamma exposure. Had cross-linking been more frequent than chain scissions, the value of T_g would increase.

3.7 Summary & Significance

This testing identified major damage thresholds for temperature and gamma radiation exposure. It also explored the impact of the dose rate of gamma radiation on the microsphere integrity. Each variable independently displayed a threshold of damage. In combination there were unique interdependences of damage. Temperature has an independent threshold for damage at 60-65 °C while gamma radiation exposure has a threshold between 800-1264 kGy. In combination, gamma doses above 400 kGy significantly worsened damage at temperatures ≥ 60 °C.

The independent temperature threshold of 60-65 °C corresponds to the glass transition temperature for PLLA. This temperature caused damage in samples even during brief exposures. Gamma exposure worsened temperature damage in this range but only showed an independent damaging effect in the 1264 kGy sample, suggesting a threshold exists between 800-1264 kGy. High fields of gamma radiation lower the glass transition temperature of PLLA through chain scissions of the polymer, explaining the interdependence of damage. Gamma radiation therefore increases the sensitivity to temperature. Tentative evidence suggests a possible gamma dose-rate threshold near 1.3 Gy/s where samples performed notably worse. The impact of dose-rate may indicate changes in the ratio of chain scissions vs. cross-linking occurring due to the gamma radiation. Another significant finding in these tests was the lack of damage progression over time in the majority of samples. Very few samples experienced increasing damage during the imaging period, notable trends of increasing damage were only identified in 65 °C batches at 400 and 600 kGy and the extreme gamma exposure of 1264 kGy at 21°C

To minimize sample damage the exposure to both temperature and gamma radiation should be reduced. Gamma radiation should be shielded using high purity lead around the irradiation site in core. Ideally the dose of gamma radiation received by samples should be below 200 kGy accumulated during the length of irradiation. Tests performed in this research showed samples exposed up to 200 kGy behaved the same as samples with no gamma exposure. The temperature experienced by samples during production, transport, and suspension must remain below 60 °C; or in cases of very high gamma doses, even lower. Even short fluctuations in temperature that exceed these thresholds is not tolerable by microspheres. The main exposure to temperature occurs during sample irradiation in core where there is gamma-induced heating and high temperatures of pool water. To maintain adequately low temperatures, it is suggested to have water circulation immediately surrounding the sample chamber to act as a heat-sink. In some cases, active cooling may be necessary.

4. Investigating the Role of Reactive Oxygen Species in Progression of Damage

4.1 Introduction

Reactive oxygen species (ROS) are a group of highly reactive molecules that are typically formed from the excitation or reduction of molecular oxygen. ROS include both free radicals and oxidizing agents that are readily converted into radicals. Because free radicals contain one or more unpaired electron(s) (Bayr, 2005), they react rapidly with chemical bonds, and can cause significant damage to both organic and non-organic materials. Common ROS include hydrogen peroxide, hydroxyl, superoxide, and singlet oxygen (Ray et al., 2012). ROS exist in small quantities naturally in living systems and are generated and mitigated through various metabolic processes or other chemical reactions. ROS primarily damage materials via oxidation reactions (Alizadeh et al., 2015).

Relevant to this work is the production of reactive oxygen species by ionizing radiation. Water molecules undergo radiolysis when energy from a photon or charged particle is deposited, breaking chemical bonds of the molecule (Alizadeh et al., 2015). The cleavage of the bonds by ionizing radiation breaks H₂O into compounds such as hydroxyl, hydrogen peroxide, and superoxide; subsequent reactions diversify the species through secondary or tertiary oxidations. Many of these highly reactive chemicals are capable of bonding to atoms in organic polymers such as PLLA, thereby disrupting its original properties.

Ho-166 emits two forms of ionizing radiation, beta negative particles and gamma photons. Both emissions can cause radiolysis of water molecules (Alizadeh et al., 2015). It is therefore possible that when Ho-166/PLLA microspheres are suspended in MSM the radiation emissions from the Ho-166 have the potential to generate ROS from water molecules in the MSM.

Previous Research conducted by Zielhuis et al. (2006) found Ho-166/PLLA microspheres to be stable prior to suspension, even after in-core neutron bombardment. Once in suspending media, only microspheres containing holmium and exposed to neutron bombardment degraded during a 52-week study. Microspheres exposed to gamma radiation, or not containing holmium, remained stable in MSM. However, prior to suspension, the Ho-166 radiation emissions do not have significant quantities of oxygen-based molecules to generate ROS. The suspending medium, being predominantly water, provides adequate target molecules for production of ROS, as well as mobility to interact with the microspheres. We would therefore expect damage caused by these free radicals to begin to appear only after suspension.

The increase of degradation over time is of particular interest for these microspheres. The rate of degradation determines the timeline restrictions between treatment processing in a dispensing laboratory and subsequent patient administration. Factors that facilitate degradation should be mitigated when possible, to expand the geographic area of treatable patients. This is of particular importance due to increasing incidence of liver malignancies in countries that do not have nuclear facilities capable of producing these treatments.

4.2 Objectives

Given the data discussed in Chapter 3, where no time-related degradation was observed for gamma-irradiated microspheres, even at extreme radiation exposures (600-800 kGy, absent sample heating), it seems likely that reactive oxygen species may contribute to degradation

increasing with time post-suspension. Once radioactive microspheres are suspended in MSM, we expect ROS to be generated in direct proportion to the sample activity. Although the ROS production rate is expected to slow with sample decay, the samples are continuously exposed to ROS. As damage to chemical bonds cannot be repaired spontaneously outside of a living system, the damage present in a sample of microspheres should increase over time and should be visible by microscopy.

Damage caused by free radicals such as ROS can be mitigated by an environment rich with antioxidants. These compounds readily react with ROS to neutralize them by donating an electron (Bayr, 2005). The ROS scavenging nature of antioxidants can be utilized to counteract ROS-induced damage in environments with high levels of free radicals or producing factors (Yoshino & Kashiwakura, 2017). This suggests the addition of a free radical scavenger to the suspending medium would reduce damage to microspheres generated by ROS oxidative reactions. Therefore, we elected to expose naïve microspheres to ROS with and without a radioprotectant to see if we could observe different rates of degradation.

4.3 Ho-166 MSM with Naïve Microspheres

Testing the potential impact of ROS on microspheres independent of other variables required an external source for ROS production. Microspheres activated by neutron bombardment are exposed to a wide range of potentially damaging factors that would confound experiment results. It was therefore decided to conduct an initial test with naïve microspheres in MSM with a separate radioactive source capable of generating ROS.

To replicate the radiation emissions generating ROS in MSM, a solution with Ho-166 was produced to add to samples of non-radioactive microspheres. Holmium chloride was selected due to its ability to dissolve readily and form an aqueous solution. Holmium chloride (HoCl_3) powder was weighed into a Maria vial and bombarded with neutrons at the McMaster Nuclear Reactor for several hours. This formed radioactive Ho-166 along with small quantities of Cl-36 and Cl-38. Cl-38 has a short half-life of 37.24 minutes and quickly decays from the sample. Cl-36 is long lived and therefore produces minimal radioactive emissions during the testing window (IAEA, 2018). To minimize the activity emissions from short-lived chlorine isotopes, the HoCl_3 sample was left overnight to provide adequate time to decay. To illustrate the approximate activity values, Table 4.1 shows the activation products and approximate activity for a 50 mg sample irradiated for 5 hours at MNR in site 9C.

The Holmium Chloride irradiations were conducted with the following specifications. The first test irradiated 106.4 mg of HoCl_3 prepacked in a maria vial for 3:45 in MNR site 9C. The second test irradiated 24 mg for 4 hours in 9C. The third test irradiated 108.5 mg for 4 hours total, completed between 9C (3 hours) and 9E (1 hour). The irradiated HoCl_3 was suspended in a small volume of MSM.

Table 4.1 Activation products of HoCl₃

Isotope	Natural Abundance	Cross Section (b)	Activation Product	Half-Life	Activity (MBq)	Activity EOB + 18 (MBq)
Cl-35	75.5%	42	Cl-36	300000 (y)	1.5e-4	1.5e-4
Cl-37	24.5%	0.8	Cl-38	37.24 (m)	333	6e-7
Ho-165	100%	64	Ho-166	26.8 (hr)	10730	6740

Data sourced from CIAAW 2021 and IAEA 2001

To minimize risk of contamination or loss of material, the holmium chloride samples were dissolved inside the Maria vial via injection of MSM. The Ho-166 solution was then used to suspend ~20 mg naïve microspheres. Adding additional unaltered MSM to samples provided control on the exact concentration of radioactivity in volume. Seven samples of microspheres were suspended in active MSM (2.0-5.3 MBq/μL) from three different HoCl₃ activations; a control sample was also prepared using non-active HoCl₃ (see Table 4.2).

Table 4.2 Sample concentrations of HoCl₃

Concentration (MBq/μL)	Activity (MBq)	Mass HoCl ₃ (mg)	Volume MSM (μL)
0 (control group)	0	18	140
2.02	212	4.9	105
3.3	215	5.0	65
3.8	155	3.6	40
3.9	565	10.5	145
4.04	295	13.9	73
5.08	305	14.4	60
5.25	315	14.8	60

All samples in this chapter were imaged at 24-hour time intervals for 72-96 hours. The number of damaged microspheres seen in digital microscope images during each timepoint was assessed and characterized as a percentage of the total microspheres in view.

Precipitate was visible in the solution during microscopy and hindered clear imaging and assessment of microsphere quality. To address this, additional protocols were needed when preparing slides for imaging. A 5 μL aliquot from the sample vial was removed and diluted in 50 μL of pure MSM. From the diluted vial, 5 μL was pipetted onto a microscope slide. An additional 5 μL of MSM was dropped on top to spread the sample and further dilute precipitate. A slide cover was added, and imaging proceeded according to standard practices.

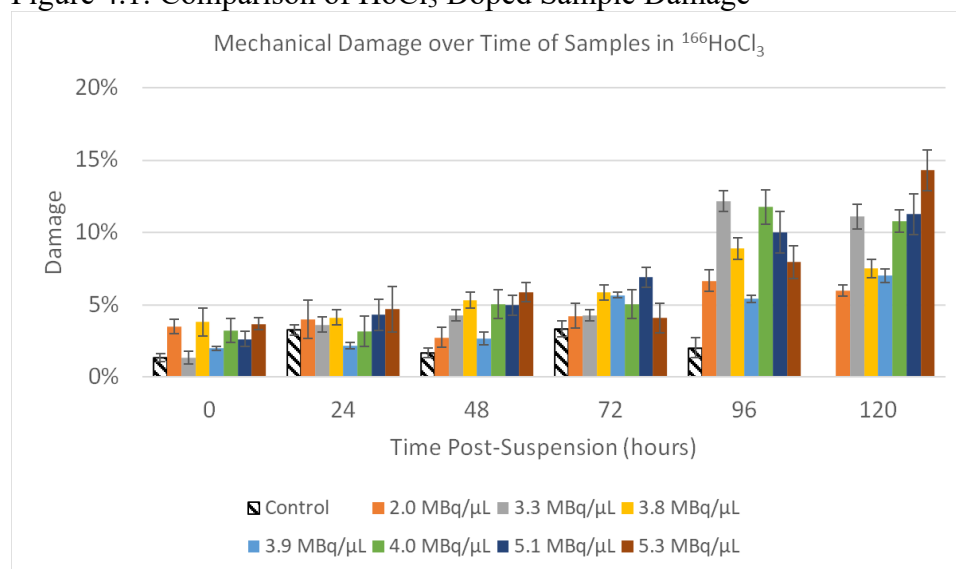
Microspheres suspended in MSM containing dissolved HoCl₃ displayed a unique form of surface damage. Microspheres appeared dimpled, having small divots or craters distributed across the surface. This appeared on all samples including the control batch with non-radioactive HoCl₃ present in the MSM. The quantity of microspheres displaying this damage increased with time post-suspension.

To assess damage imparted to microspheres due to radioactivity-generating ROS, the mechanical damage forms such as cracks and broken spheres was counted separately from surface dimpling. Based on comparison of control samples to irradiated sample, the mechanical damage provided a more accurate assessment of damage linked to ROS at each timepoint.

Full tables displaying sample damage, total counted, and damaged spheres are available in Appendix A –Data.

All batches initially had damage below 4% frequency. The radioactive samples at the time of suspension demonstrate similar damage levels to the control batch. The mechanical damage for samples at each timepoint is displayed below in Figure 4.1. The control batch with non-active holmium chloride maintains a consistent level of damage from suspensions to 96 hours. As time post-suspension increases, the mechanical damage of samples containing Ho-166 worsens. The deviations from the control batch becomes more evident at each timepoint. At the 72-hour mark, all radioactive samples have exceeded 4% damage.

Figure 4.1: Comparison of HoCl₃ Doped Sample Damage



Damage of samples exposed to HoCl₃ in MSM up to 120 hours. Control sample was only imaged until 96 hours and is therefore not presented in the 120-hour timepoint.

The samples do not show a correlation between activity concentration and damage levels in these tests. The 3.3 MBq/μL displayed higher levels of damage than the majority of samples at 96 and 120 hours. However, the 3.9 MBq/μL had significantly less than almost all other samples, most notable at the later time points. It should be noted that the range of activity concentrations used was small due to practical and licensing constraints, which may have made it difficult to detect concentration-dependent effects.

There were mild increases of damage in samples with radioactive Ho-166 during the 120 hours. However, no significant correlation was observed between the concentration of radioactivity and the damage of microspheres. This suggests the hypothesis of ROS contributing to degradation over time may be correct, but ROS production may be saturated or relatively similar in the range of activity concentrations tested. Patient doses have activity concentrations in the range of 8-12

MBq/ μL , significantly higher than the concentrations tested here. Due to the disparity, ROS may have a much more drastic impact on degradation of patient treatments.

The addition of aqueous dissolved HoCl_3 added variables and presented some logistic challenges, limiting testing parameters and accuracy. The control batch, containing non-radioactive HoCl_3 provided some insight into impacts directly imparted by the ionic concentration and precipitate present in solution. The addition of HoCl_3 resulted in precipitate which hindered clear imaging of microspheres. We suspect this material was HoPO_4 based on the phosphate content in the MSM solution. The precipitate hindered the accurate assessment of microsphere quality and lead researchers to “wash” samples prior to imaging to remove some precipitate.

Due to practical limitations of irradiation length and licensing, the HoCl_3 had a relatively low specific activity. This limited the range of activity concentrations that could be tested. This also meant samples had large ionic concentrations of these elements with only small activity concentrations. The mass added to achieve the desired activity concentration varied with each sample and may therefore impact the resultant damage.

Mechanical damage was characterized separate from surface dimpling (discussed in Section 4.3 and 4.4) and used to assess the potential of ROS induced degradation post-suspension. The samples with radioactive Ho-166 present in the MSM displayed increasing damage over time, which supports the hypothesis that radiation emitted by the microspheres causes time-dependent degradation in neutron activated materials. This study did not, however, show a correlation between the concentration of radioactivity and the severity of damage in samples. This is likely due to the narrow range of activity concentrations tested in this study. A larger range should be assessed to conclude if a dependence does exist. A higher specific activity of HoCl_3 would minimize the total mass required to test activity concentrations: reducing precipitate formation and external ionic concentration.

4.4 Radioprotectant

Having examined naïve microspheres with Ho-166, we now looked at whether this damage could be mitigated with a radioprotectant. To test if it was reactive oxygen species specifically leading to microsphere damage instead of other radiation-induced interactions, a free radical scavenger was added to the sample suspending media in a second set of experiments. The chosen antioxidant was L-ascorbic acid (AA) due to its biocompatible nature in humans and water solubility. Ascorbate is better known as vitamin C and is an important characteristic in human diet (Foyer, 1993). For these tests Fluka Analytical grade L-Ascorbic Acid was used.

A stock solution of 1 mol/L was created by dissolving 0.525 g (3 mmols) of L-ascorbic acid in 3 mL of MSM. This stock was then used to dissolve a neutron activated HoCl_3 sample (109.6 mg, 6.7 GBq). A volume of 214 μL was removed and used to suspend naïve microspheres for testing. A control batch was made with similar quantities of non-irradiated holmium chloride and ascorbate dissolved in MSM and added to naïve microspheres. The quantities of each material are listed in Table 4.3.

Table 4.3 Control batch material quantities

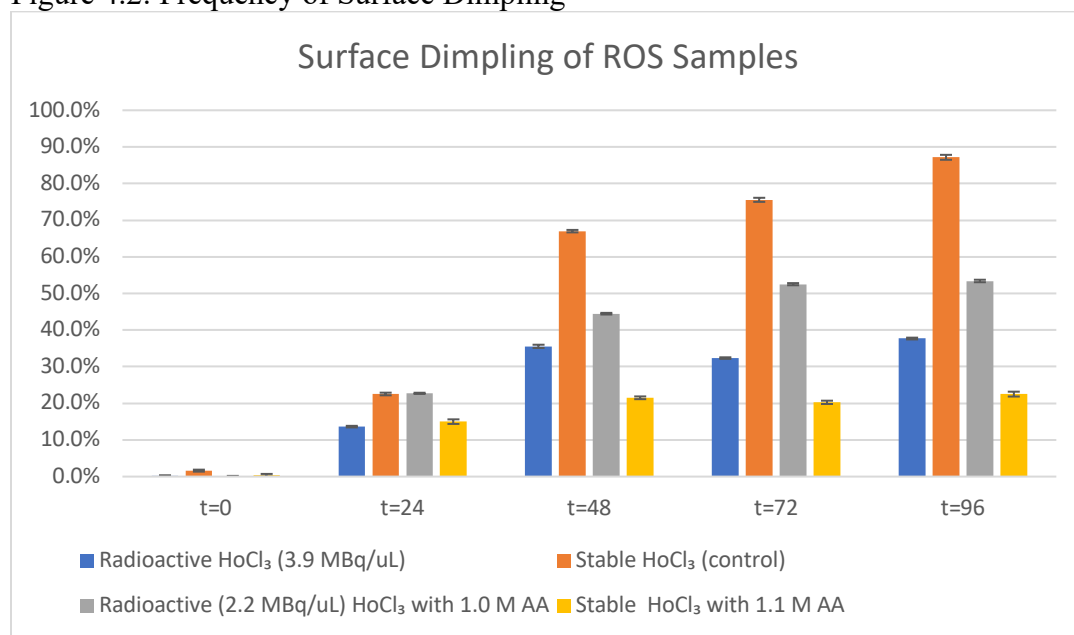
	Final Radioactivity Concentration (MBq/ μ L)	Final Ascorbic Acid Concentration (mol/L)	Mass HoCl_3 (mg)	Mass L-Ascorbic Acid (mg)	MSM volume (μ L)	Microspheres (mg)
Control	0	1.1	8.0	36.7	180	22.4
Initial	2.2	1.0	7.7	~37	~214	~20

Similar to the previous samples, these batches of microspheres began exhibiting surface dimpling. Prior to the experiments described in this chapter, this type of damage had not been previously observed in Ho-166/PLLA microspheres during any routine or non-standard microsphere activation. The dimpling increased with time (see Figure 4.2). The damage occurred in all samples, both radioactive and stable.

This new form of damage may be the result of two potential interactions. First, the dimpling may be developing due to physical abrasion with the precipitate leaving surface indentations. Alternatively, the dimpling may indicate an ionic concentration gradient is swapping material out of the PLLA matrix and subsequently shrinking the radius.

To quantify data linked to the presence of radioactivity generating ROS, the surface dimpling was characterized separately from mechanical damage. Surface dimpling for the initial AA samples and HoCl_3 -only samples is shown below in Figure 4.2. Surprisingly, the greatest damage was seen for the control sample that had no radioactive material. However, this may be artificially higher than the other samples since microspheres were only placed in one category. Microspheres with mechanical damage may also have shown surface dimpling but were counted in the mechanical damage category.

Figure 4.2: Frequency of Surface Dimpling

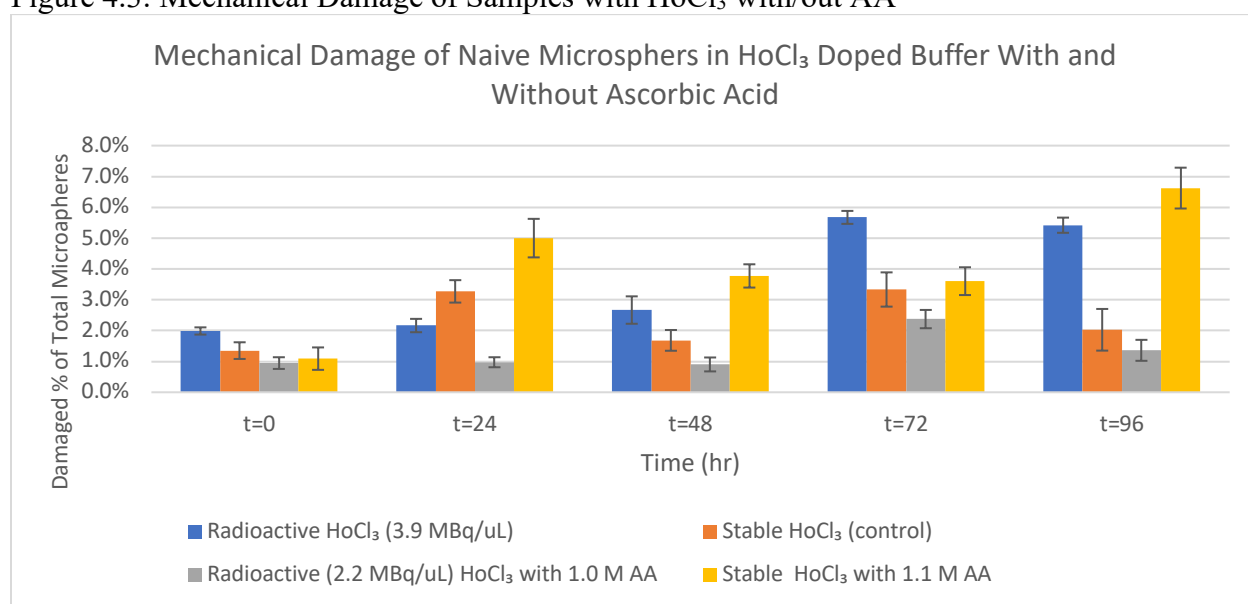


Surface dimpling of samples exposed to HoCl_3 in MSM with or without AA.

As surface dimpling is a novel phenomenon and does not appear to be related to the typical mechanical damage that is associated with microsphere failures in a clinical setting, we elected to focus on the mechanical damage as a means of quantifying damage to samples used in these ROS experiments.

The initial test of AA added to samples suspended in MSM doped with HoCl_3 both active and non-active were compared to the previous samples not containing AA. The results are presented in Figure 4.3 below. Looking specifically at the samples exposed to radioactivity with (grey bars) and without (blue bars) a radioprotectant, it appears that the addition of ascorbic acid was successful in limiting damage to microspheres: the untreated sample (blue) consistently showed a statistically significant higher level of damage than the protected sample (grey).

Figure 4.3: Mechanical Damage of Samples with HoCl_3 with/out AA



Mechanical damage of samples exposed to HoCl_3 in MSM with or without AA up to 96 hours.

However, there were some unexpected findings as well. The greatest level of damage was found in the sample treated with radioprotectant, and with non-radioactive holmium chloride (yellow bars). This increase of damage may be associated with oxidative stress, similar to samples exposed to sources of reactive oxygen species. The high concentration of AA in MSM may have caused damage by the extreme ratio of unpaired free radical scavengers. The radioactive sample with a 1 M free radical scavenger performed extremely well, with consistently low levels of damage (<3%). In comparison to a similar radioactive sample without AA (blue), the radioactive AA batch (grey) maintained adequate quality while the non-AA sample had rising damage levels as time increased.

Samples containing radioactive HoCl_3 dissolved in the MSM had increasing mechanical damage during the imaging period (see Figure 4.1), which is normal for microspheres neutron irradiated in-core. We took this to mean the degradation of samples over time is linked to radiation interactions in the suspending media. A similar test was conducted containing radioactive HoCl_3

in MSM with the addition of ascorbic acid to a concentration of 1 M (see Figure 4.3). The samples radioactive holmium without radioprotectant worsened over the imaging period. The similar radioactive batch that included 1 M ascorbic acid stayed at a consistent level of damage during the testing. At each timepoint the radioactive sample with AA maintained damage levels below the control batch with minimal fluctuations. The sample with radioprotectant performed better than both radioactive and control tests with the addition of HoCl_3 in similar concentrations. This means the addition of a free radical scavenger can reduce damage resulting from interactions of radiation with the suspending media. This effect shows potential to mitigate sample degradation in-transport to patients by the addition of AA.

A control sample containing ascorbic acid (1.1 M) and non-active holmium chloride performed worse than expected (see Figure 4.3). This suggests a damaging effect of ascorbic acid at this concentration when exposed independent of a radiation source. The sample displayed high levels of both mechanical damage and surface dimpling. The presence of high volumes of free radical scavengers in an environment without ROS being generated may have created an imbalance of electron donor molecules, resulting in reactions with the PLLA. A balance of free radicals and free radical scavengers are necessary to prevent oxidative stress (Lobo et al., 2010). The mechanical damage exceeded that of the HoCl_3 control and radioactive test as well as the radioactive holmium with AA. This was unexpected and means the addition of a free radical scavenger such as AA, has the ability to damage PLLA if not balanced with free radicals. We suspect the difference of damage between samples with radioactive holmium generating ROS independent of a free radical scavenger and samples with ascorbic acid independent of a free radical source, are due to the ionic concentrations. However, the mechanism for damage is suspected to be similar.

To test the effect different concentrations of free radical scavengers had on damage mitigation, several samples were suspended with unique activity and radioprotectant concentrations. A second stock was prepared of 0.75 mol/L by dissolving L-ascorbic acid (0.0658 g, 0.037 mmols) in MSM (500 μL). This was used along with irradiated HoCl_3 (108.3 mg, 6.4 GBq) dissolved in MSM (2 ml) to suspend naive microspheres. These tests included 0.5, 0.25, and 0.1 M ascorbic acid concentration. The activity concentrations are approximately 20% of those tested previously. Data on each sample is described in Table 4.4 below.

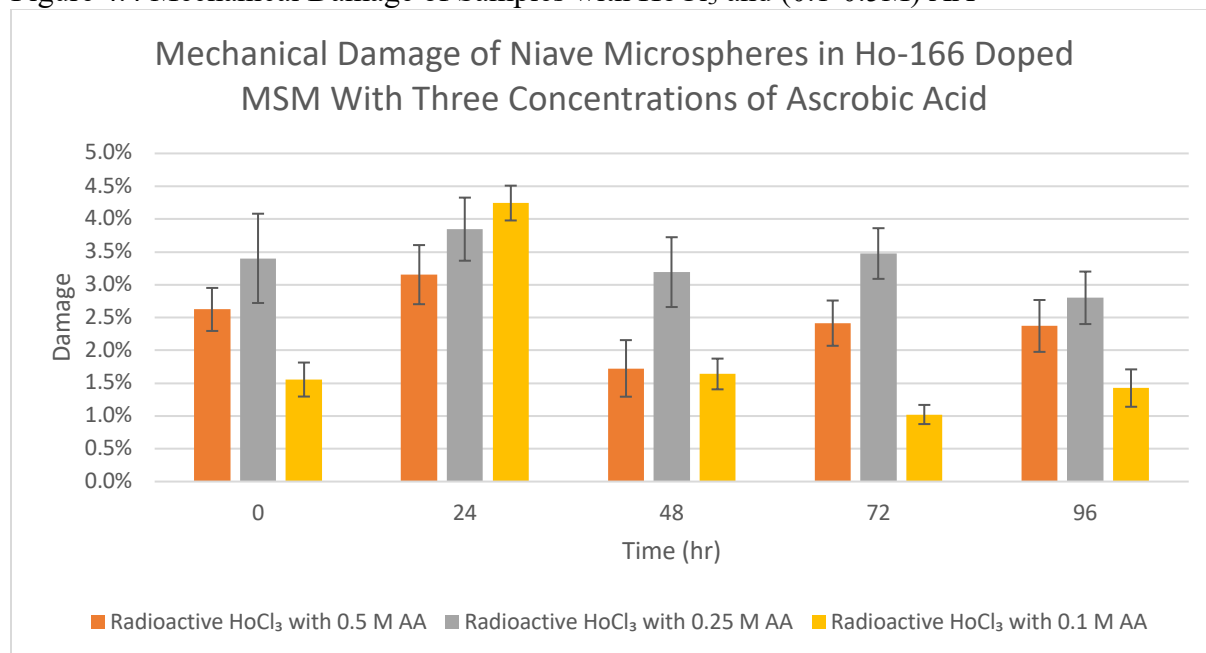
Table 4.4. Batch makeup for samples including AA

Final Volume (μL)	Final Radioactivity Concentration ($\text{MBq}/\mu\text{L}$)	Ascorbic Acid Concentration (mol/L)	Volume Ho-166 Solution added (μL)	Volume 0.75 M ascorbate stock added (μL)	Pure MSM added (μL)	Microspheres (mg)
30	0.4	0.50	10	20.0	0	4.0
50	0.5	0.25	10	16.7	23.3	5.7
70	0.5	0.10	15	9.3	45.6	8.7

For all tests the samples were imaged at 24-hour intervals until 96 hours post-suspension. Samples were “washed” in the same process as described in 4.4.1.

The second tests of ascorbic acid mitigating effect utilized 3 different concentrations of AA present in the MSM. These tests aimed to assess if increased free radical scavenger concentration would correlate with decreased microspher damage. The results from these experiments are presented in Figure 4.4. Considering uncertainties, sample quality remained consistent during the imaging period with the exception of the 24-hour check. All samples had an increased level of damage at 24 hours which may indicate some damage from handling while imaging that day. Samples all displayed adequate quality levels during these tests.

Figure 4.4 Mechanical Damage of Samples with HoCl_3 and (0.1-0.5M) AA



Mechanical of samples exposed to HoCl_3 in MSM with concentrations of (0.1, 0.25, 0.5) AA up to 96 hours.

The second round of tests with ascorbic acid aimed to analyze concentration impact of the radioprotectant. These tests assessed concentrations of AA in the range of 0.1-0.5 M in samples containing radioactive Ho-166 (see Figure 4.4). These samples had significantly lower levels of radioactivity due to licencing limitations and therefore less ROS production. The concentration of these samples is two orders of magnitude below what a patient dose would be and therefore cannot directly reflect on degradation of patient samples.

All samples maintained quality similar to control batches during the imaging period. These findings suggest, but cannot guarantee, the addition of the AA mitigated damage. However, the small activity levels may not be sufficient to impart significant damage initially. The lowest concentration of AA performed best of these three tests. We presume this concentration aligned best to the quantity of ROS generated by the radioactivity, providing free radical scavenging without extreme excess contributing to oxidative stress itself. This would mean the optimal concentration of radioprotectant to mitigate ROS induced damage would depend on the radioactivity of the sample.

4.5 Immediate vs. Delayed Suspension

Given the licensing constraints that limit the amount of free Ho-166 that can be handled in the laboratory, an additional experiment was designed to explore potential ROS effects. Two Maria vials each containing ~400 mg microspheres were exposed to neutron flux simultaneously in a standard production site of McMaster Nuclear Reactor. The vials were stacked one on top of the other in the irradiation tube, a configuration that has been validated for the production of clinical quality microspheres, and is therefore known to generate microspheres that can survive in suspension media for > 72 h after suspension. This produced two samples with identical time in-core – and therefore identical temperature, gamma, and neutron exposures.

One of the samples was suspended in MSM very soon after irradiation ended while still at a high specific activity (see Table 4.5), while the second sample was only suspended in MSM after several half-lives, when only kBq quantities of Ho-166 remained. Theoretically, frequent decay events in the high specific activity sample should generate a large amount of ROS, resulting in damage to the microspheres that accrued over time. In contrast, only minimal ROS should be generated in the low SA sample (processed after several days decay).

The damage present in high SA and low SA samples from the same irradiation were compared (see Figure 4.5). The test was conducted twice with irradiation lengths of 4 hours and 6 hours. The position (top or bottom) was switched in the tests for the immediate or delayed suspension sample to ensure tests were not indicating damage from a geometric position.

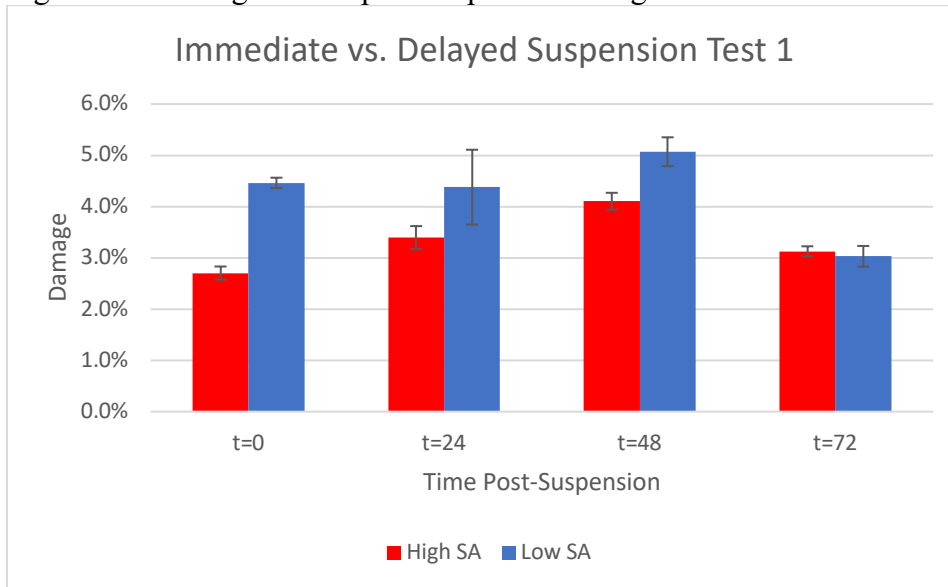
Table 4.5. Immediate vs. delayed suspension tests

Double Stack Test ID	Test 1. MNR #168973		Test 2. MNR #169084	
	High SA	Low SA	High SA	Low SA
Sample Activity at Suspension	2453 MBq	0.79 MBq	3870 MBq	0.35 MBq
Date of Suspension	Jan 17, 2023	Jan 30, 2023	Feb 13, 2023	Feb 28, 2023
Stack Position	Bottom	Top	Top	Bottom
Irradiation Length	4 hours	4 hours	6 hours	6 hours
Microsphere Mass (mg)	387.6	390.2	391.5	390.8
Specific Activity at Suspension (MBq/mg)	6.3	~2e-3	9.9	~9e-4

Contrary to expectation, the microsphere samples did not show significant differences in damage progression between those suspended with a high specific activity vs. suspended after decaying for several half-lives. During test 1 the high activity sample showed less damage than the sample suspended after decay, though damage was minimal in all cases (see Figure 4.5). The damage present in samples fluctuates during the imaging period but the 72-hour checkpoint for both samples appeared higher quality than previous datapoints. This does not suggest the specific activity at suspension increases the progression rate of damage. This suggested that ROS generated by radioactive decay of Ho-166 inside the microspheres is not the main driver of time-dependent degradation. Alternatively, it could be that the different positioning of the Maria vials

within the irradiation tube caused different heat/radiation characteristics that affected the results of the experiment.

Figure 4.5: Damage of Samples Suspended at High vs. Low SA

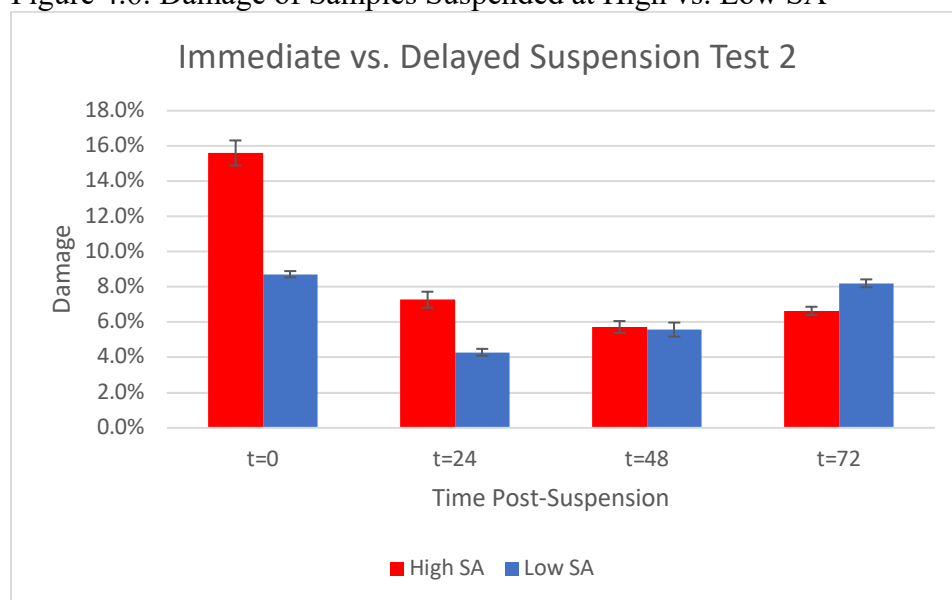


Microsphere damage compared between samples irradiated simultaneously for 4 hours but suspended immediately vs. after several half-lives.

A second experiment was therefore conducted, this time suspending the “top” soon after end of irradiation and allowing the bottom sample to decay to low specific activity. Compared to the initial double-stack irradiation, this experiment attempted to analyze a higher specific activity at end of irradiation (9.9 MBq/mg vs 6.3 MBq/mg) to emphasize any potential effects on ROS formation. The comparison of damage is presented in Figure 4.6 below.

During the second test the high SA sample initially displayed significantly greater levels of damage than the decayed sample, consistent with the theory that increased SA corresponds to increased ROS, and therefore increased microsphere damage. However, the damage level decreases and comes more in line by 48 hours. At 72 hours the cold sample has a higher damage percentage. Neither sample show an increasing trend of damage over time. During all imaging points both samples are above acceptable damage levels. Extreme fluctuations in damage in the high SA sample may be the result of rough handling during the t=0 imaging session. The sample appeared much more stable at all other imaging timepoints and stayed within a 3% window between 24-96 hours. This does not support the original theory that radiation emissions from the activated microspheres would create ROS and subsequently degrade over time. Future work should analyze a longer timeframe to assess if there is deviation between the samples past 72 hours.

Figure 4.6: Damage of Samples Suspended at High vs. Low SA



Microsphere damage compared between samples irradiated simultaneously for 6 hours but suspended immediately vs. after several half-lives.

The suspension of one sample soon after activation (2.3-3.8 GBq) and one ~13 half-lives after activation (0.2-0.8 MBq), allowed for direct observation of the impact of activity, and therefore ROS generation, on time-dependent damage. None of the double stack test samples showed a continually increasing trend of damage over the 72 hours. Rather all samples fluctuated in damage quantity during the time checks. Stability of samples within the first 48 hours is required for samples used for patient treatments. It is therefore unsurprising to have samples maintain low damage levels during this time if the irradiation is below the validated limits. The limitation of this test is that it cannot restrict damage incurred to the PLLA microsphere from the beta and gamma emissions directly. The exposure of decayed samples to their own radiation emissions are significantly greater due to the extended time between irradiation and suspension.

4.6 Creating ROS with Co-60

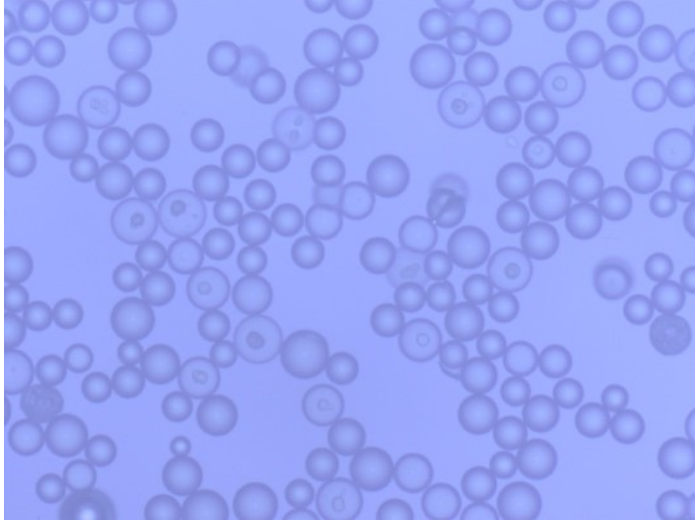
A final experiment was designed in an attempt to elucidate the effects of ROS on microspheres. As in the previous chapter, a Co-60 source was used as the radiation source to avoid the complications described above with cold holmium chloride, or exposure of the microspheres to poorly understood conditions in the reactor core.

Six samples of microspheres were prepared for gamma exposure, this time with the microspheres already suspended with MSM. Samples were irradiated to 400, 600, or 800 kGy, with and without ascorbic acid (AA) added at a concentration of 1 mol/L to act as a radical scavenger and mitigate ROS-induced damage. After gamma exposure, the microspheres divided, heated, and suspended in additional media as described in Chapter 3.

Samples in pure MSM and not exposed to any temperature performed significantly better than all other wet tests, with damage in the range of 6-17% at 24 hours. This meant all samples exceeded the 4.7% threshold by 24 hours into imaging. However, the style of damage was of interest. The

samples that received 400 and 800 kGy of dose presented standard forms of damage at room temperature. The 600 kGy displayed a unique form of damage that appeared like small protrusions from the sphere surface. Figure 4.7 shows a the 600 kGy sample irradiated in MSM and kept at room temperature.

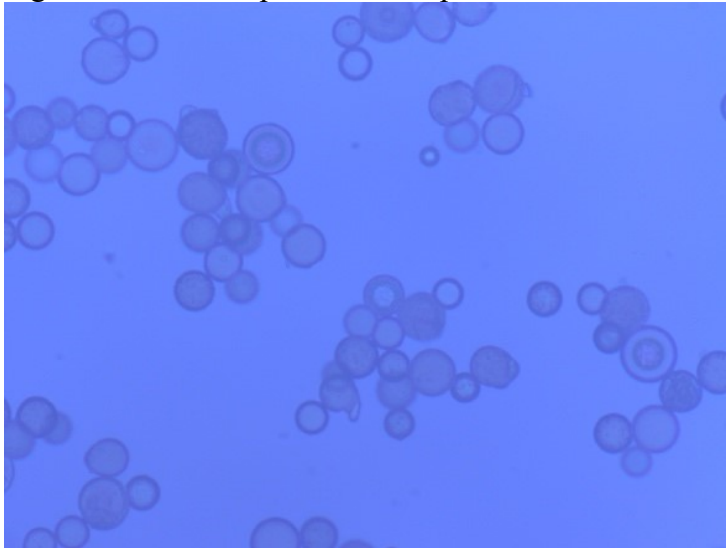
Figure 4.7: Herniated Microsphere Damage



Unique damage form showing protrusion of PLLA coating.

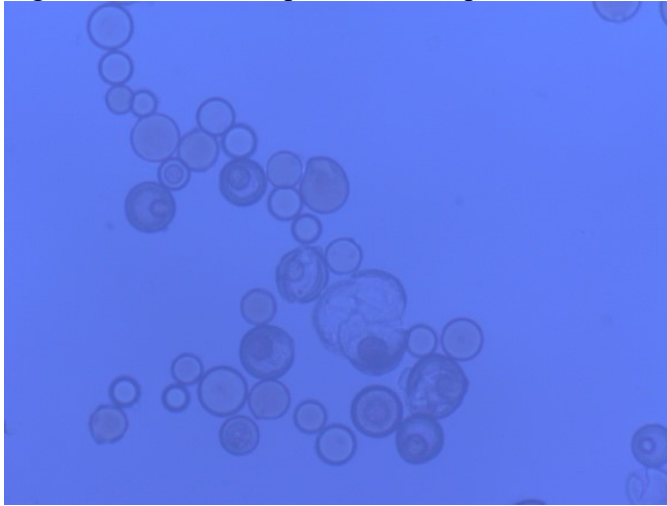
When heat was applied to these samples the level of damage escalated severely. Damage was greater than 75% in all samples. A new form of damage presented as an internal ball within the sphere. At more extreme levels the outer shell surrounding the internal ball would grossly expand and occasionally split. This damage is shown in Figure 4.8 from the 400 kGy sample in MSM heated to 55 °C. A more severe stage of this damage is presented in Figure 4.9 from the 600 kGy sample at 55 °C.

Figure 4.8: Mild Ruptured Microspheres



Unique damage form showing microsphere outer expansion and rupture.

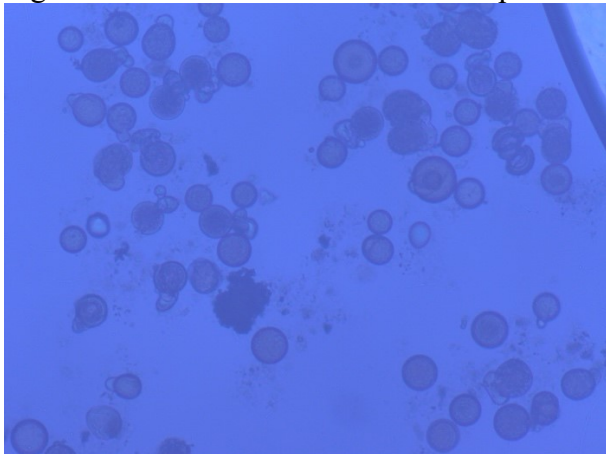
Figure 4.9: Severe Ruptured Microspheres



Unique damage form showing microsphere outer expansion and rupture.

Similarly, samples irradiated while suspended in MSM with ascorbic acid had extreme levels of damage. The samples with added ascorbic acid performed worse than those with MSM alone. At room temperature all samples exceed the 4.7% threshold. The addition of heat caused samples to display extreme surface dimpling and damage. The samples appear to be shedding small shards of PLLA coating. Similar internal balls form in many samples or have a darkened internal content with the standard coating. Several microspheres became oblong in nature rather than spherical. Figure 4.10 shows many of these damage characteristics. The image is taken from the 400 kGy batch heated to 65 °C.

Figure 4.10: Darkened Internal Microspheres



Unique damage form showing microsphere with inner dark balls forming and exterior shedding.

The severe increase in damage when samples were suspended in MSM during gamma irradiations and exposed to temperature suggests radiation interaction with liquid may cause

sensitivity to temperature. This may signal reactive oxygen species being produced in MSM and causing polymer chain scissions.

4.7 Conclusions

This chapter investigated the potential contributions of reactive oxygen species to degradation of samples over time. The findings from samples suspended with Ho-166 in the solution suggest the radiation emissions interacting with MSM do contribute to microsphere degradation. Samples with >2 MBq/ μ L of radioactive holmium showed slight trends of damage increasing over time, supporting the proposed hypothesis. The addition of ascorbic acid, a free radical scavenger improved sample quality when radioactive holmium was present. This similarly points to the production of ROS as a source of damage. These findings are significant in their suggestion of a mitigation strategy for damage developing in samples once suspended in MSM. However, in the absence of a radiation source, ascorbic acid had a damaging effect on microspheres. The addition of a radioprotectant would therefore need to be optimized for levels of radioactivity in patient doses and require further study.

The lack of significant differences of damage in samples that were suspended immediately or following a decay period did not provide support for or against the hypothesized damage. Neither sample showed increasing levels of damage during the first 72 hours. Additional tests with longer irradiation times, creating higher specific activity and surpassing validated limits, should be conducted to draw conclusions. The gamma irradiation of microspheres suspended in liquid created an environment that could generate large quantities of ROS during a discrete time (only generated during gamma exposure). The samples had devastating levels of damage and suggest ROS being produced in MSM may be capable of directly damaging microspheres. This experiment also shows a critical need for microspheres to be dry during radiation exposure. It is difficult to extrapolate from the data gathered in these tests due to the plethora of additional factors microspheres are exposed to in-core that may play a part in degradation over time. However the findings suggest ROS may be a factor contributing to degradation of patient doses once suspended in MSM.

These findings suggest processing labs that suspend microspheres and perform quality testing prior to patient injection should be as close to the patient location as possible. The minimization of travel distance between processing lab and hospital reduces the time microspheres are degrading in MSM. The severe reaction of microspheres to gamma radiation exposure while suspended also advises the procedures and style of travel that can be tolerated between processing lab and hospital. International shipping on airplanes may be accompanied by x-ray scanning of packages by border protection services. X-rays, similar to gamma radiation, have the potential to generate a large volume of ROS in MSM and cause severe damage. Similarly, suspended microspheres cannot tolerate sterilization with gamma rays, a common method for sanitizing hospital equipment. Most critical, is if the QA has been conducted prior to this point and unsafe treatments may unknowingly be administered to patients. Further research is needed to understand this impact fully, but a conservative approach should be taken based on these preliminary results.

5. Investigating the Impact of Shielding Thickness In-Core

5.1 Introduction

The results presented in the previous chapters indicate that both temperature and gamma radiation can affect the quality of holmium PLLA microspheres. However, there are wide ranges of gamma energies emitted from the core of a nuclear reactor. Therefore, samples irradiated in-core not only experience neutron flux, but also gamma radiation. Gamma radiation deposits energy in matter, resulting in heat generation. The gamma-induced heating and chain scissions/crosslinking cause damage to polymer samples. The heat production can be counteracted with direct contact to coolant or reduction of gamma exposure. At least one study indicates that the heat generated by gamma radiation is the predominant contributor to sample temperature during irradiation in the nuclear reactor (Alqahtani et al., 2022).

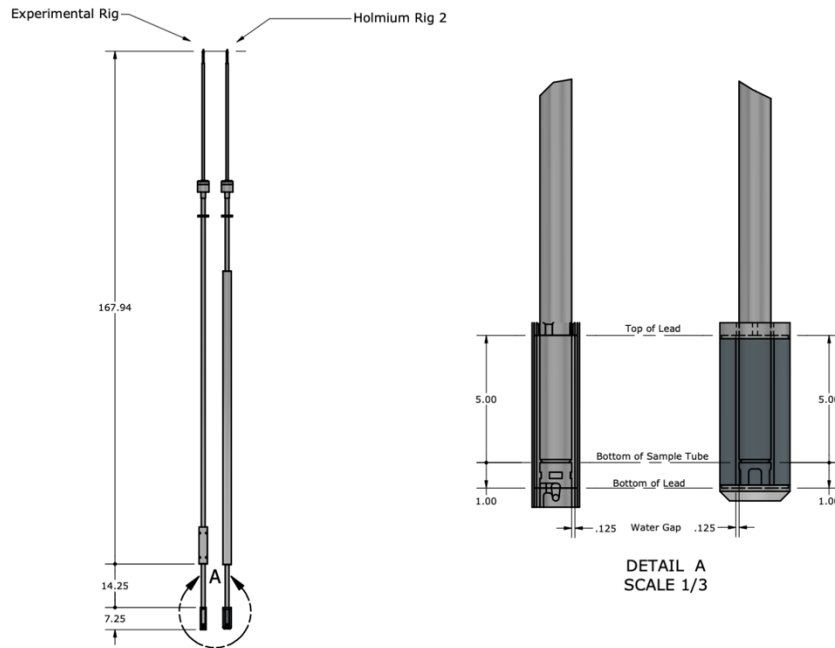
High purity lead is frequently used to shield ionizing radiation, particularly photons such as gamma or x-rays. Lead has a high linear attenuation for photons, making it an effective shield even at small thicknesses. The effectiveness of lead in shielding radiation is linked to its high atomic weight and high density (Moharram et al., 2020). To reduce the gamma radiation interacting with samples, lead shielding can be used.

When scientists at McMaster Nuclear Reactor first attempted to irradiate QuiremSpheres in-core, the test was conducted in a “RIFLS” tube positioned in 9C for 4 hours. This sample rig had no lead shielding to reduce the gamma exposure. The microspheres melted into a solid mass, a severe form of damage (Heysel et al., 2018). Further experiment led to the commissioning of an irradiation tube with lead lining the sample chamber. Microspheres irradiated with Pb shielding had significantly less damage. Longer irradiations can be tolerated by samples in-core when shielded with Pb (Heysel et al., 2018). The initial Pb-lined chamber was designed to allow the largest thickness of lead within the site geometry. However, no research was conducted to optimize the Pb thickness or understand its underlying impact on samples.

5.2 Apparatus & experiment design

To better understand the effect of Pb shielding on samples, an experimental irradiation device was designed. The test apparatus mirrored the overarching design of the current MNR irradiation rig apart from the sample chamber shield. The cooling channel, sample position and in-core position within MNR (9C) were kept consistent. The specifications of both rigs can be seen in Figure 5.1 below. The test rig was designed with 5 detachable lead shields, ranging in thickness from 0.25-1.25 cm in increments of 0.25 cm. This apparatus enables in-core irradiations where the only variable changed is the thickness of the Pb, and therefore the gamma radiation (and gamma heating) experienced by the sample.

Figure 5.1: Holmium Irradiation Apparatus Diagram



Technical drawing of experimental apparatus to allow attachments of Pb shielding compared with the original irradiation tube used for QuiremSpheres activations.

Several variables were studied regarding the conditions in the sample chamber including thermal neutron flux, fast neutron flux, temperature, and microsphere quality. Temperature was tested using a non-reversible denaturing strip from Digi-Sense. Type A strips with a range of 37-65 °C and Type B strips with a range of 71-110 °C were irradiated in the sample chamber for 30 minutes.

A cobalt (1%) aluminum (99%) wire was irradiated for 30 minutes then measured with a HPGe detector. The activation products of Co-60 and Na-24 were characterized and used to calculate thermal and fast neutron flux (see equation 2). The thermal neutron flux was calculated from the $^{59}\text{Co}(n,\gamma)^{60}\text{Co}$ reaction. This reaction has a thermal neutron capture cross section of 37.2 (0.02 eV) barns. This is significantly greater than the fast neutron capture cross section for Co-59 of $6.9\text{e-}4$ (14 MeV) barns (Nakagawa et al. 2005). The activation of Co-59 to Co-60 through this reaction therefore occurs almost exclusively from thermal neutron capture and can provide insight to thermal neutron flux. The fast neutron flux was calculated from the $^{27}\text{Al}(n,\alpha)^{24}\text{Na}$ reaction. This reaction has a threshold energy of 3.2 MeV, and increases in cross-section with neutron energy to a maximum neutron capture cross section of 1.25 barns at 13.5 MeV (Zolotarev, 2009). Measurement of Na-24 production is therefore used to measure the flux of fast neutrons.

To assess the thermal neutron flux, and rate of Ho-166 formation, a sample of ~50 mg holmium oxide was irradiated in the sample chamber for 30 minutes then measured for activity in a dose calibrator. The activity was used to calculate thermal neutron flux and neutron capture rates of holmium (see equation 2). Due to the large energy spectrum of neutrons in-core, this provided a direct comparison of activation yields of holmium.

Finally, samples of ~400 mg of microspheres were irradiated in the test rig to reach various levels of specific activity (20-40 MBq/mg). The microspheres were decayed for several days before being suspended and imaged according to previously specified procedures. These tests were completed for each of the Pb attachments and compared. Initial tests aimed to produce microspheres are 25 and 40 MBq/mg. Based on the results at these baseline measurements, additional irradiations were conducted to find the highest specific activity that resulted in microspheres of quality suitable for patient treatment.

5.3 Results

5.3.1 Temperature

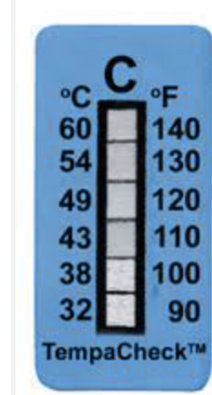
The temperature for each thickness of Pb shielding is presented in Table 5.1 below. As expected, the temperature within the sample tube decreases with additional lead shielding: attenuation of gamma radiation by the lead limits the amount of gamma-induced heating that occurs. The temperature decreases by ~17 °C from the thinnest to thickest Pb attachment. This is a notable reduction. The thinnest (0.25 cm) Pb shield reduced temperatures to the range of 60-65 °C which aligns with the glass transition temperature of PLLA. Reaching the glass transition temperature has been linked to significant damage to microspheres and polymer instability. However, the temperature strips used will slightly underestimate the heating of samples due to the self-insulating effect of PLLA and high neutron cross section. Because of this, a conservative margin should be used to ensure adequate heat reduction in samples.

Table 5.1. Temperature results

Pb Thickness (cm)	Minimum Temperature °C	Unreached Temperature °C
0.25	60	65
0.50	54	59
0.75	54	59
1.00	46	49
1.25	43	46

Note that two temperatures are reported for each test. The temperature strips do not provide a continuous reading; instead, they respond in increments of a few degrees Celsius. Once a temperature threshold is reached, the box denatures. The values provided are therefore the highest temperature exceeded, and the lowest temperature not exceeded, based on the next unchanged temperature step (see Figure 5.2). The strip therefore gives researchers a range between the exceeded and unexceeded temperatures where the temperature could fall.

Figure 5.2: Temperature Strip



A permanently denaturing temperature test strip in the range of 32-60 °C.

5.3.2 Neutron Flux & Energy

CoAl wire samples were measured for 10 minutes in position P2 (2.5 cm from detector) using an Ortec GMX series coaxial HPGe detector with DSPEC Plus signal processing to measure gamma emissions at 1173.2 (Co-60, 99.85%), 1332.5 (Co-60, 99.98%), 1368.6 (Na-24, 99.99%) and 2754.0 (99.86%) keV. The counts were efficiency corrected with a previously obtained efficiency curve for the position used. The efficiency factor is calculated according to the following equation where x is the photon energy in keV.

$$y = 4.734x^{-0.864} \quad (1)$$

x = Energy (keV)

y = Detector Efficiency

Values were corrected for decay from the end of irradiation. The activity, mass, time in-core, and neutron capture cross sections were used to calculate neutron flux with the following equation.

$$A = \phi\sigma N(1 - e^{-\lambda t}) \quad (2)$$

A = Activity (Bq)

ϕ = Neutron Flux ($cm^{-2}s^{-1}$)

σ = Neutron capture cross section ($b= 10^{-24} cm^2$)

N = Number of Target Atoms

λ = Decay constant (s^{-1})

t = Time (s)

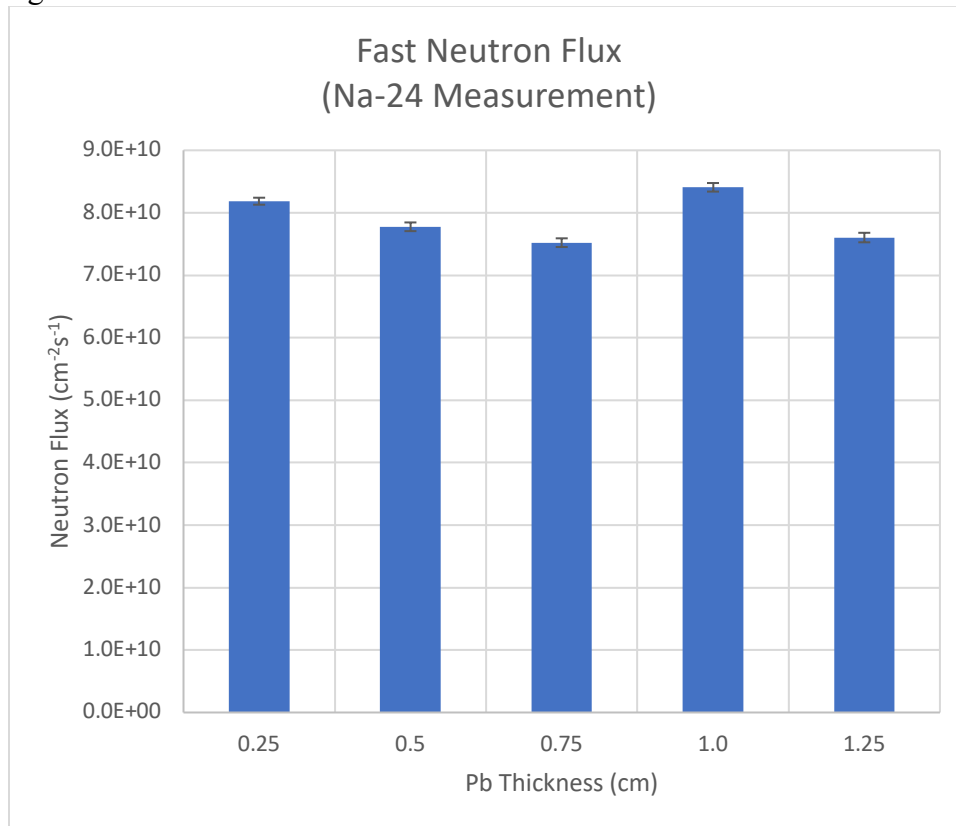
The thermal and fast neutron flux was calculated from the $Co^{59}(n, \gamma) Co^{60}$ and $Al^{27}(n, \alpha) Na^{24}$ reactions respectively. The uncertainty was propagated from the uncertainty of counts on the APTEC software used to characterize the emission peaks. The thermal and fast neutron flux as calculated from the CoAl wire is listed in table 5.2 below.

Table 5.2. Neutron flux values from CoAl wire testing

Pb Thickness (cm)	Thermal Neutron Flux ($\text{cm}^{-2}\text{s}^{-1}$)	Relative Uncertainty	Fast Neutron Flux ($\text{cm}^{-2}\text{s}^{-1}$)	Relative Uncertainty
0.25	1.32E+13	0.5%	8.19E+10	0.7%
0.50	1.07E+13	0.6%	7.78E+10	0.9%
0.75	9.29E+12	0.6%	7.52E+10	0.9%
1.00	9.81E+12	0.6%	8.41E+10	0.8%
1.25	1.42E+13	0.5%	7.60E+10	1.0%

The fast neutron flux as a function of Pb thickness is presented in Figure 5.3 below. There is no obvious reason for these fluctuations in fast neutron flux; however, it follows a general decreasing trend prior to spiking at the 1.0 cm lead attachment.

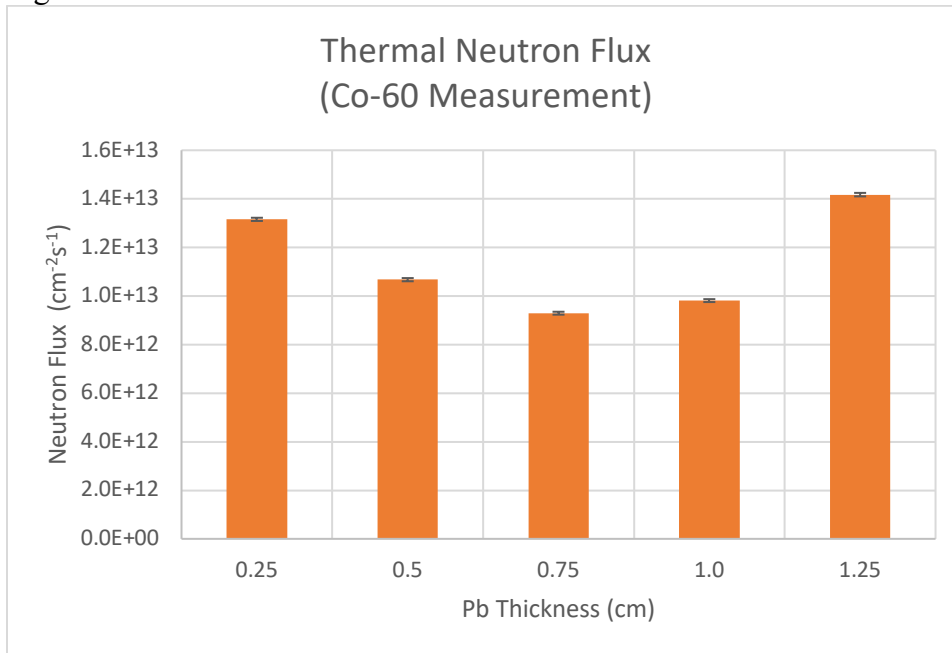
Figure 5.3: Fast Neutron Flux



Empirically determined values for fast neutron flux in each Pb attachment.

In contrast to the fast flux measurements, that showed only moderate (and random) changes with different Pb attachments, the thermal neutron flux measurements from the cobalt reaction displayed a parabola trend. The neutron flux decreased, achieving a minimum at the 0.75 cm mark with a thermal flux more than 40% less than what was seen for the thickest Pb attachment. The flux then increased slightly at 1.0 cm and had a very large increase at 1.25 cm. This contrasts the 11% difference between maximum and minimum values for fast neutron flux. The thermal flux is represented below in Figure 5.4.

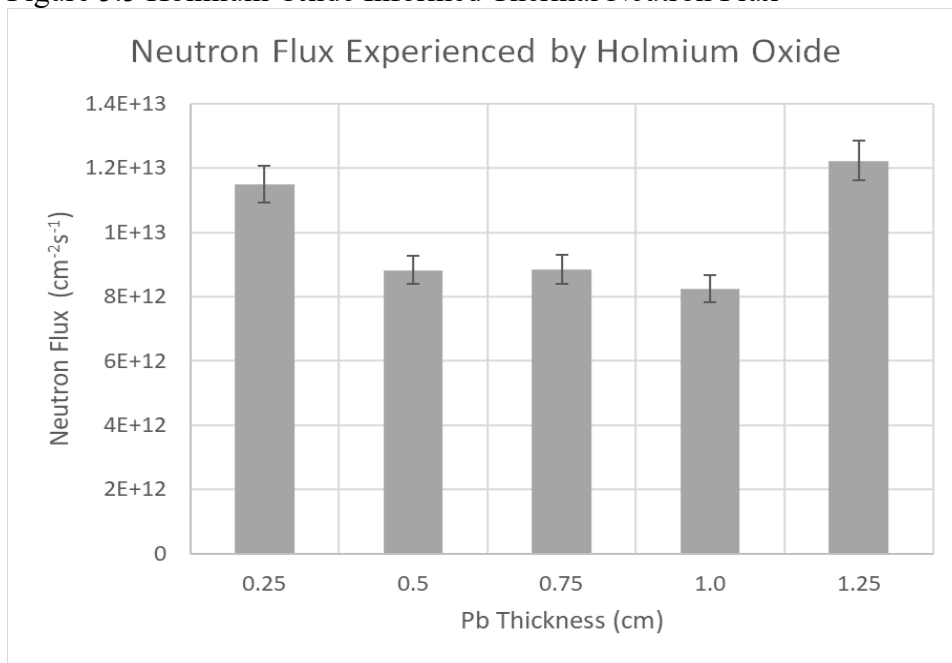
Figure 5.4: Cobalt Informed Thermal Neutron Flux



Empirically determined values for thermal neutron flux in each Pb attachment.

As there is no obvious reason for the trend shown in Figure 5.4, the holmium oxide sample data was analyzed and assessed for patterns. Each sample was measured in a standard nuclear medicine dose calibrator and corrected for decay to end of irradiation. The activity and mass were used to calculate the thermal neutron flux experienced by the sample. The neutron flux measurements are presented below in Figure 5.5.

Figure 5.5 Holmium Oxide Informed Thermal Neutron Flux

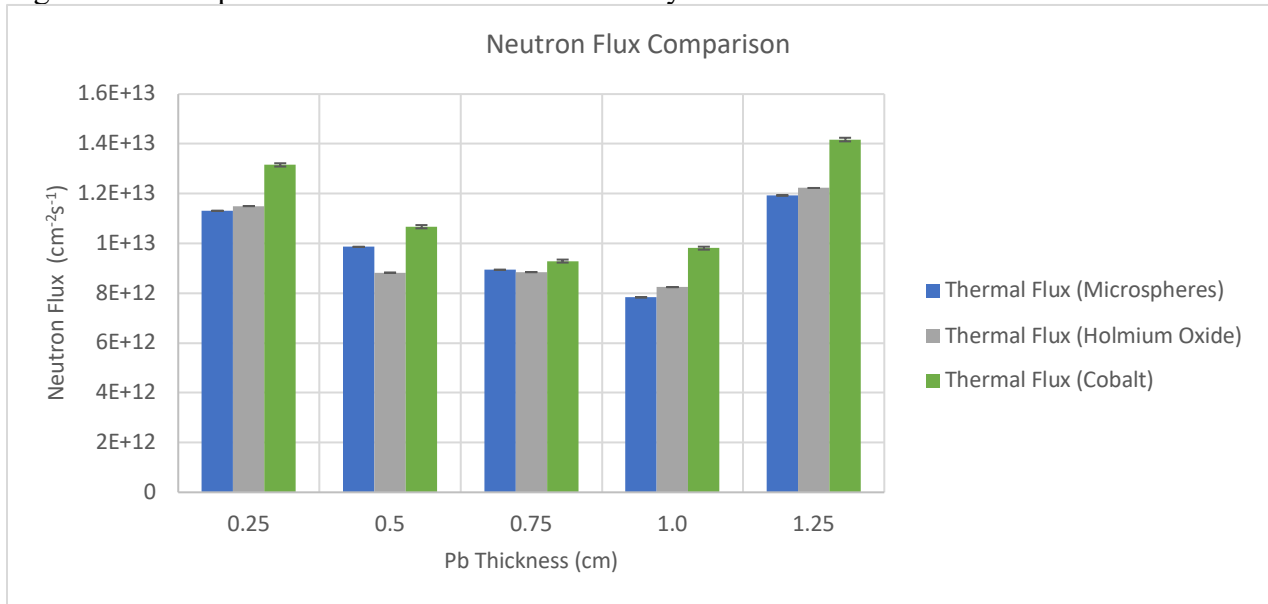


Empirically determined values for thermal neutron flux in each Pb attachment.

The neutron flux values from holmium oxide measurements generally align well with the thermal neutron values from Co-60 data and supports the trend observed. The 1.25 cm attachment has the highest flux value and the lowest occurs for the 1.0 cm attachment. The difference of 0.25 cm in shielding, from 1.0 to 1.25 cm, resulted in an increase of 49% in the neutron flux experienced by samples.

The overall neutron flux measurements – including data from the microsphere irradiations described in the next section – are consolidated in Figure 5.6 below. The microsphere-informed thermal neutron flux is an average of 4-5 measurements for each data point presented. The ratio of fast neutrons to thermal neutrons had a large change in the 1.0 cm attachment. This attachment has the greatest amount of fast neutrons while simultaneously having one of the lowest thermal neutron flux measurements. Possible reasons for this observation are presented in the Section 5.4.

Figure 5.6: Comparison of Thermal Neutron Flux by Pb Thickness



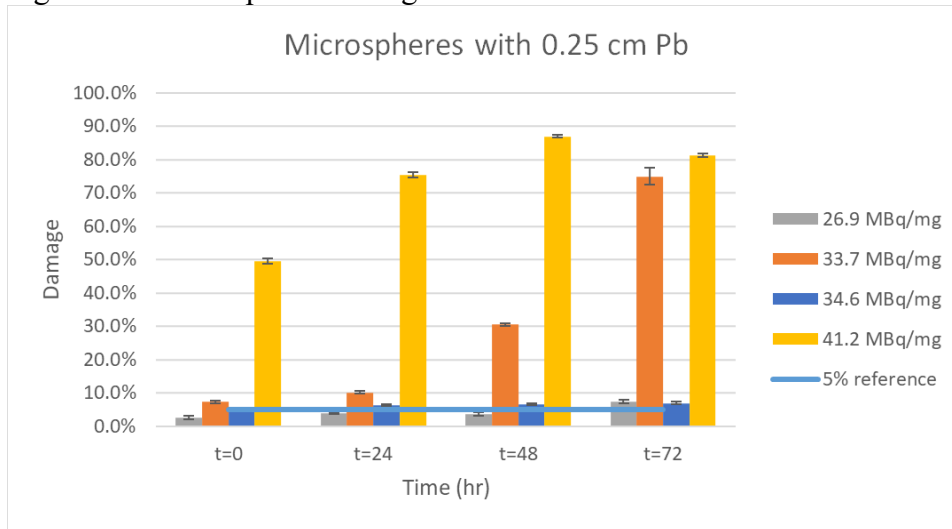
Empirically determined values for thermal and fast neutron flux in each Pb attachment from all tests.

5.3.3 Microsphere Activations

For each Pb thickness, several samples of microspheres were irradiated and analyzed from suspension to 72 hrs. The damage was compared for each specific activity (SA) to understand the highest achievable SA that resulted in adequate sample quality. Acceptable quality was characterized as damage below 5% up to and including 48 hours after time of suspension. Full tables displaying sample damage, total counted, and damaged spheres is available in Appendix A -Data.

Samples irradiated in core with the 0.25 cm Pb attachment are presented below in Figure 5.7 below. The samples at $41 \pm 5\%$ MBq/mg and $34 \pm 5\%$ MBq/mg had significant damage increase over the 96-hour period. Only the $27 \pm 5\%$ sample passed the quality control (QC) criteria described previously.

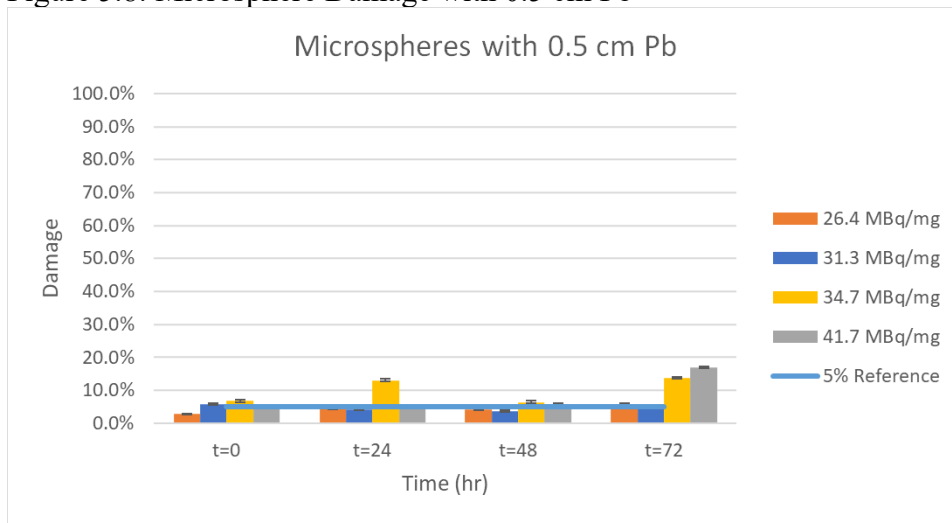
Figure 5.7: Microsphere Damage with 0.25 cm Pb



Damage trends for microspheres shielded in core with 0.25 cm Pb at various specific activities over 72 hours.

Samples irradiated with 0.5 cm of Pb had similar passing and failing SA as the 0.25 cm attachment. Although the damage exceeding the threshold is much lower for this attachment. The 26.4 ±5% MBq/mg sample passes QA but the 31.4 ±5% MBq/mg failed by a very small margin. The results of all samples in the 0.5 cm attachment are presented in Figure 5.8 below.

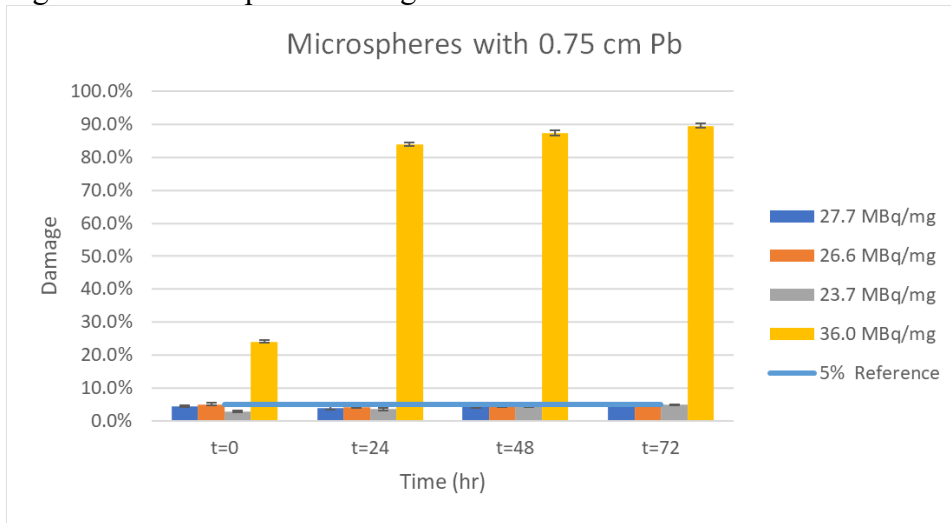
Figure 5.8: Microsphere Damage with 0.5 cm Pb



Damage trends for microspheres shielded in core with 0.5 cm Pb at various specific activities over 72 hours.

Samples irradiated in the 0.75 cm Pb attachment passed QA with a max SA of 27.6 ±5% MBq/mg. The SA of 26.6 ±5% MBq/mg and 23.7 ±5% MBq/mg also passed. The sample at 36.0 ±5% MBq/mg had significant damage immediately upon suspension. The damage for samples in this attachment is presented in Figure 5.9 below.

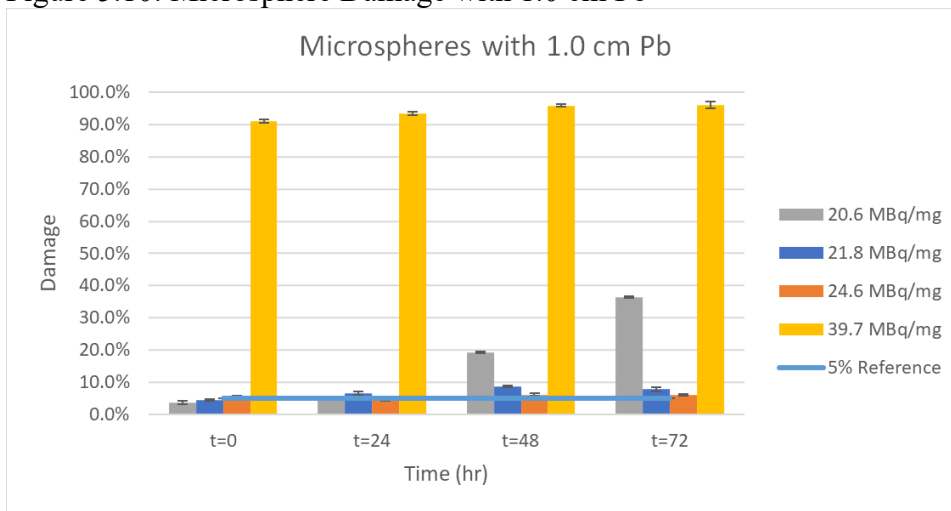
Figure 5.9: Microsphere Damage with 0.75 cm Pb



Damage trends for microspheres shielded in core with 0.75 cm Pb at various specific activities over 72 hours.

Samples in the 1.0 cm Pb attachment had unexpected results. All samples tested had unacceptable levels of damage, even with SA as low as $20.6 \pm 5\%$ MBq/mg. The damage for the 1.0 cm samples is presented in Figure 5.10 below. The poor microsphere quality and unexpected neutron flux values may indicate a flaw in the Pb piece.

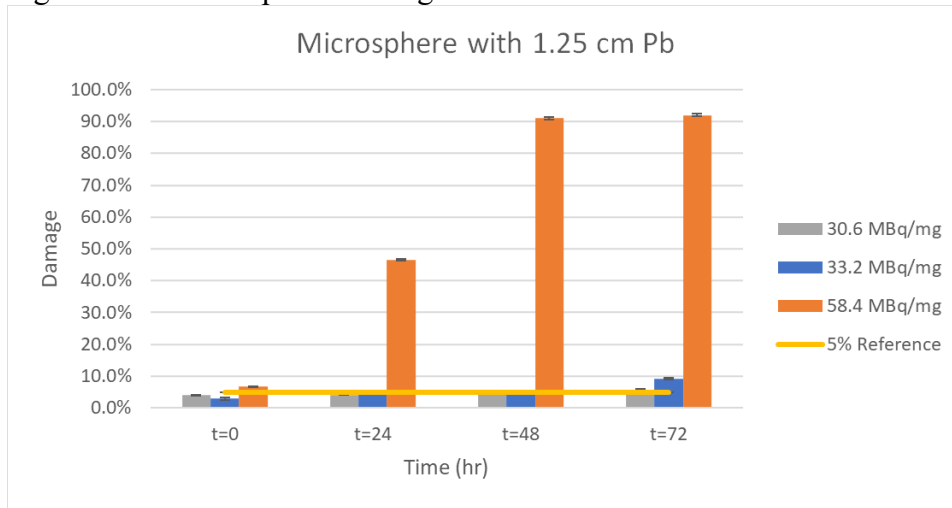
Figure 5.10: Microsphere Damage with 1.0 cm Pb



Damage trends for microspheres shielded in core with 1.0 cm Pb at various specific activities over 72 hours.

Samples with 1.25 cm of Pb were able to achieve the highest SA while passing QA. Samples in this attachment survived up to a SA of $33.2 \pm 5\%$ MBq/mg. A high SA test to $58.4 \pm 5\%$ MBq/mg was conducted but did not pass QA. The results of samples in 1.25 cm Pb are presented in Figure 5.11 below.

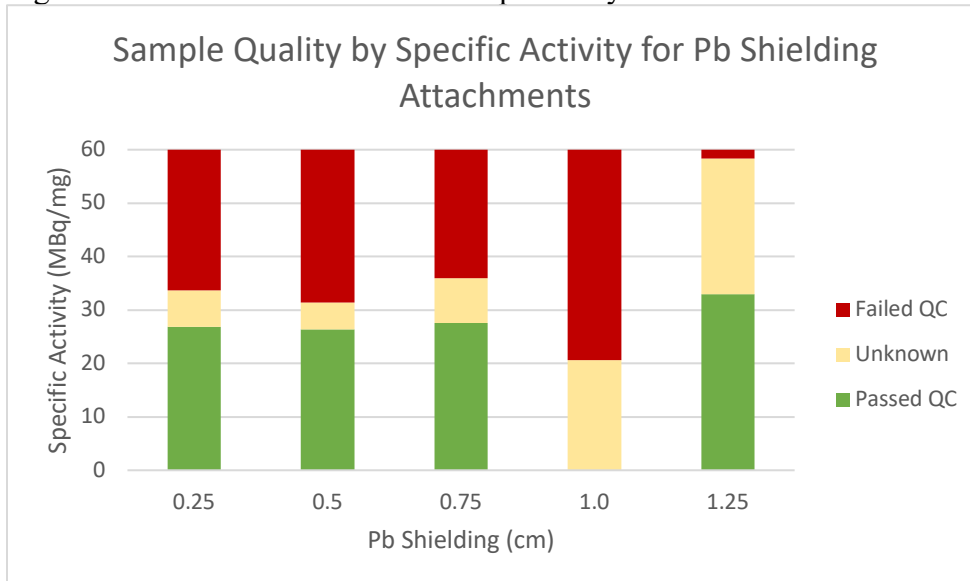
Figure 5.11: Microsphere Damage with 1.25 cm Pb



Damage trends for microspheres shielded in core with 1.25 cm Pb at various specific activities over 72 hours.

A comparison of the achievable SA and fail point for each Pb attachment is presented in Figure 5.12. Each attachment has a window of unknown quality between the highest SA that passed and the lowest SA that failed. Not surprisingly, the 1.25 cm had the best results, passing at a higher SA than all other attachments. The unknown quality region is very large and suggests this rig may be able to handle samples significantly greater than the highest SA to pass. Samples in 0.25-0.75 cm Pb have similar ranges of achievable SA. The 1.0 cm sample failed at all SA values tested. The unknown region for this attachment is therefore all SA below the lowest SA to fail in this rig.

Figure 5.12: Achievable SA of Microspheres by Pb Thickness



Quality of microspheres at specific activities measured against a 5% damage threshold.

5.4 Discussion

The tests described here allowed for characterization of the impact Pb shielding has on conditions experienced by samples in-core. The various attachments of Pb had significantly different conditions in the sample chamber. These tests analyzed temperature, fast/thermal neutron flux, and sample quality.

The temperature decreased for thicker Pb shielding. The difference was found to be ~ 17 °C from the smallest to largest attachment, only a 1 cm difference. The significant improvement with relatively small additions of Pb makes it feasible to mitigate damage even in sites with minimal space for added material. Temperature is known to have significant impact on samples from previous tests. This factor suggests it is advantageous to have larger quantities of Pb shielding to keep samples below the damage threshold, found earlier to be the glass transition temperature. As shown in Chapter 3, the glass transition temperature decreases with gamma radiation exposure and reached ~ 58 °C for exposures of 600 kGy. A minimum thickness of 0.75 cm of Pb is needed to reduce ambient temperature to below T_g in MNR site 9C/9E when operating at 3 MW. To account for microspheres self-insulating and heating during neutron capture reactions, >1.0 cm should be used.

The ratio of fast to thermal neutrons is a variable that had not been previously explored for Ho-166/PLLA microsphere damage. Studies assessing the impact of fast neutrons have shown the interactions can result in oxidation of the chain backbone for many polymer species. The modification of chemical structure by fast neutrons alters the physical properties of polymers and can contribute to degradation. The change in morphology has also been shown to alter the glass transition temperature (Rivaton & Arnold, 2008). The damage to microspheres in attachments with the highest fast neutron flux suggest that fast neutrons may play a role in causing microsphere degradation.

The 4th Pb attachment, with 1.0 cm of Pb, had unexpected results in microsphere damage. The 1.0 cm Pb piece has a significantly higher ratio of fast:thermal neutrons than all other attachments. Samples irradiated in with this attachment were significantly more damaged and microsphere quality was very poor even at low specific activities. The temperature value for this attachment was acceptably low so damage appears to be caused by the fast neutron and gamma exposure in-core. The low thermal neutron flux in this site resulted in samples needing to be exposed to the conditions in-core for longer to achieve the same SA. This increased time in-core may have contributed to the poor outcomes since it would result in a larger accumulated gamma radiation dose and additional gamma-induced heating. There is not a clear reason for the odd thermal:fast neutron ratio that occurred at the 1.0 cm shield. Alternatively, the poor results may indicate a flaw in the Pb shield.

We theorize the changes in neutron flux for various attachments may be due to displacement of water, the neutron moderator, and/or scattering effects of the neutrons on the Pb creating a focal point. Since the outer radius of Pb expands to accommodate the shield thickness this decreases the volume of water from the core to the sample and increases the distance from the shield edge to sample. Water acts as the neutron moderator at MNR and slows fast neutrons to a thermal energy. The displacement of water (reducing the volume of water from core to sample) may have two different impacts, altering the flux in opposite ways. First the reduction of moderator

pathlength would result in less fast neutrons being thermalized, thereby reducing thermal flux. This aligns with trends seen for thermal neutron flux from 0.25-1.0 cm. Alternatively, less water would result in fewer neutron scattering interactions that could absorb the neutron, contributing to a higher thermal neutron flux.

The second theory focuses on how neutrons may be interacting with the Pb shield. Neutrons scatter when interacting with materials (Latham & Cassels, 1948). The predominant angle of scatter is dependent on the molecular structure of the target material and neutron energy (Moore et al., 1968). The curved exterior of the shield may have the ability to act as a focusing lens for neutrons due to preferential angles of scatter. This could therefore produce a focal point with increased neutron flux. The focal point would change depth based on the distance from the edge of the Pb to the sample cavity. This phenomenon could therefore explain an increase or decrease in flux relative to its location in proximity to the sample. Additionally, due to the energy dependence of cross sections for each scattering angle, a spread of neutron energies may occur. This phenomenon may act in the same way as a prism spreading light by incident wavelength. Focal points with increased neutron flux of a particular energy would therefore occur. This may explain the various ratios of fast:thermal neutron flux experienced by different Pb shields. This theory could be further tested by measuring neutron energy spectrums with rectangular block Pb shields of varying thickness to determine if the phenomenon ceases.

Overall, the 1.25 cm attachment performed the best. This supports theories that increasing Pb shielding in-core positively impacts microsphere quality. This attachment had the lowest temperature, and highest thermal neutron flux. This allowed shorter irradiations resulting in less exposure to the in-core environment. This site also had the lowest ratio of fast:thermal neutrons out of all sites. Samples in this attachment maintained adequate quality at the highest SA of all attachments.

5.5 Significance & Impact on Production

New facilities looking to irradiate Ho-166/PLLA microspheres in nuclear reactors should be very thoughtful when choosing a site. The environmental conditions of the site have drastic impacts on sample quality and if microspheres can be used for patient treatment. These findings suggest that a site should be selected with a low ratio of fast:thermal neutrons. The temperature of the site should be below 60 °C at minimum to avoid the glass transition temperature. Temperature can be reduced by adding additional Pb shielding to the sample chamber. The external radius of Pb shielding appears to impact the thermal and fast neutron flux within a site. Testing should be conducted with shielding in-place to measure the unique neutron spectrum. The addition of Pb is favourable for its ability to reduce temperature and gamma radiation exposure without generating unwanted activation products (i.e. radioisotopes of Pb) that contribute their own gamma radiation to the sample environment. Linear blocks of Pb may remove some of the challenges associated with neutron scatter focal points, leading to a more uniform energy distribution on the sample.

6. Conclusions

This research studied the impact of various factors present during in-core irradiation and following suspension on Ho-166/PLLA microsphere integrity. The findings presented in this thesis provide critical insights into ideal production facilities and equipment design. The need for scientific understanding of damaging factors increases as the number of nuclear facilities neutron irradiating or processing Ho-166/PLLA samples expands.

One of the most notable findings in this research is the damage threshold associated with heating to the glass transition temperature of PLLA. Reaching this temperature alters polymer morphology and results in unsustainable levels of damage. To limit the maximum temperature exposure of samples, sites should be temperature tested during initial assessment with a denaturing temperature strip. Lead shielding was seen to reduce sample heating in-core and should be added to production sites in nuclear reactors with temperatures at or near 60 °C. Temperatures in this range cannot be tolerated even for very short times. It should be noted that exposure to gamma radiation in large accumulated doses (several hundred kGy) reduces the glass transition temperature. Gamma radiation and temperature therefore worsen damage when combined.

Gamma radiation in the absence of other variables only showed damage to microspheres at extreme doses ~1200 kGy. Prior to this, chain scissions are assumed to be occurring but do not visibly alter microspheres. Gamma radiation in-core of a nuclear reactor is difficult to measure due to the extreme conditions.

Hypotheses on the damaging effect of reactive oxygen species produced by holmium radiation emissions once suspended in MSM showed promising initial results. The addition of radioactive holmium to MSM with microspheres did show increasing damage beyond control values. There were mild trends of damage progressing during the imaging period, a previously unexplained characteristic of radioactive samples. The testing conducted also proposed a possible strategy for mitigating ROS damage through the addition of a free radical scavenger. Samples containing both radioactive holmium and a free radical scavenger had better outcomes. Although it was found that free radical scavengers can have a damaging effect on microspheres when not paired with an appropriate source of radioactivity. Further testing should be conducted with holmium chloride at a higher specific activity to reduce any negative impacts of the ionic concentration in the MSM.

Physically altering the thickness of Pb shielding for samples in core showed notable changes to temperature, neutron spectrum, neutron flux, and sample quality. Further, these tests indicate a potential degrading factor of fast neutrons. Previously fast neutrons had been assumed to have no interaction with samples and had not readily been tested. Additional study of fast neutron degradation of the microspheres independent of all other variables should be conducted. The changes to neutron energy spectrum suggest the curvature of the Pb shield surrounding the sample tube may act as a curved lens, creating regions of focused neutron flux specific to the incident energy. To further assess the possible impact of Pb shielding geometry and thickness impacts, testing should be conducted with linear Pb sheets or a neutron generator to assess energy dependence.

7. Bibliography

- Adam, R., Lucidi, V., & Bismuth, H. (2004). Hepatic colorectal metastases: methods of improving resectability. *Surgical Clinics of North America*, 84(2), 659–671. <https://doi.org/10.1016/J.SUC.2003.12.005>
- Alizadeh, E., Orlando, T. M., & Sanche, L. (2015). Biomolecular Damage Induced by Ionizing Radiation: The Direct and Indirect Effects of Low-Energy Electrons on DNA. *Annual Review of Physical Chemistry*, 66(1), 379–398. <https://doi.org/10.1146/annurev-physchem-040513-103605>
- Allred, J. D., Niedbala, J., Mikell, J. K., Owen, D., Frey, K. A., & Dewaraja, Y. K. (2018). The value of 99mTc-MAA SPECT/CT for lung shunt estimation in 90Y radioembolization: a phantom and patient study. *EJNMMI Research*, 8(1), 50. <https://doi.org/10.1186/s13550-018-0402-8>
- Alqahtani, M., Buijs, A., & ALQahtani, M. (2022). A Study of Gamma Heating, Neutron Flux, and Gamma Flux Under Several Reactor Core Conditions in the McMaster Nuclear Reactor. *Nuclear Science and Engineering*, 196(5), 614–622. <https://doi.org/10.1080/00295639.2021.2003651>
- Alqahtani, M., Buijs, A., & Day, S. E. (2020). Experimental measurement and Monte Carlo code simulation of the gamma heating at different irradiation sites in a nuclear research reactor. *Nuclear Engineering and Design*, 364, 110690. <https://doi.org/10.1016/J.NUCENGDES.2020.110690>
- American Cancer Society. (2022). *Cancer Facts & Figures 2022*.
- Androsch, R., & Di Lorenzo, M. L. (2013). Kinetics of crystal nucleation of poly(L-lactic acid). *Polymer*, 54(26), 6882–6885. <https://doi.org/10.1016/j.polymer.2013.10.056>
- Armstrong, A., Naperstkw, Z., Heysel, C., Duivenvoorde, N., Sigger, J., & Nijsen, F. (2019). Development of a North American supply of holmium-166 microspheres for Selective Internal Radiation Therapy (SIRT) of liver malignancies. *Journal of Nuclear Medicine*, 60, 631.
- Arnold, C. A., Pezhouh, M. K., Lam-Himlin, D., Pittman, M. E., Vandenbussche, C., & Voltaggio, L. (2019). *Y-TheraSpheres The New Look of Yttrium-90*. www.ajsp.com
- Arranja, A. G., Hennink, W. E., Chassagne, C., Denkova, A. G., & Nijsen, J. F. W. (2020). Preparation and characterization of inorganic radioactive holmium-166 microspheres for internal radionuclide therapy. *Materials Science and Engineering C*, 106(September 2019), 110244. <https://doi.org/10.1016/j.msec.2019.110244>
- Bai, L., Zhao, X., Bao, R. Y., Liu, Z. Y., Yang, M. B., & Yang, W. (2018). Effect of temperature, crystallinity and molecular chain orientation on the thermal conductivity of polymers: a case study of PLLA. *Journal of Materials Science*, 53(14), 10543–10553. <https://doi.org/10.1007/s10853-018-2306-4>
- Barros, E. C., Sene, F. F., & Martinelli, J. R. (2014). Development of phosphate glass microspheres containing holmium for selective internal radiotherapy. *Materials Science Forum*, 775–776, 34–38. <https://doi.org/10.4028/www.scientific.net/MSF.775-776.34>
- Bastian, P., Bartkowski, R., Köhler, H., & Kissel, T. (1998). Chemo-embolization of experimental liver metastases. Part I: distribution of biodegradable microspheres of different sizes in an animal model for the locoregional therapy. *European Journal of Pharmaceutics and Biopharmaceutics*, 46(3), 243–254. [https://doi.org/10.1016/S0939-6411\(98\)00047-2](https://doi.org/10.1016/S0939-6411(98)00047-2)
- Bayr, H. (2005). Reactive oxygen species. *Critical Care Medicine*, 33(Suppl), S498–S501. <https://doi.org/10.1097/01.CCM.0000186787.64500.12>
- Bé, M.-M., Chisté, V., Dulieu, C., Browne, E., Baglin, C., Chechev, V. P., Egorov, A., Kuzmenko, N. K., Sergeev, V. O., Kondev, F. G., Luca, A., Galán, M., Huang, X., Wang, B., Helmer, R. G., Schönfeld, E., Dersch, R., Vanin, V. R., De Castro, R. M., ... Wu, S. C. (n.d.). *Monographie BIPM-5 Table of Radionuclides (Comments on evaluation)*.

- Bednarek, M., Borska, K., & Kubisa, P. (2020). Crosslinking of Polylactide by High Energy Irradiation and Photo-Curing. *Molecules*, 25(21), 4919. <https://doi.org/10.3390/molecules25214919>
- Bengtsson, G., Carlsson, G., Hafström, L., & Jönsson, P. E. (1981). Natural history of patients with untreated liver metastases from colorectal cancer. *The American Journal of Surgery*, 141(5), 586–589. [https://doi.org/10.1016/0002-9610\(81\)90057-X](https://doi.org/10.1016/0002-9610(81)90057-X)
- Burrel, M., Reig, M., Forner, A., Barrufet, M., Lope, C. R. de, Tremosini, S., Ayuso, C., Llovet, J. M., Real, M. I., & Bruix, J. (2012). Survival of patients with hepatocellular carcinoma treated by transarterial chemoembolisation (TACE) using Drug Eluting Beads. Implications for clinical practice and trial design. *Journal of Hepatology*, 56(6), 1330–1335. <https://doi.org/10.1016/j.jhep.2012.01.008>
- Butler, J. P., & Santry, D. C. (1963). EXCITATION CURVES FOR THE REACTIONS Al-27(n, α)Na-24 AND Mg-24(n, p)Na-24. *Canadian Journal of Physics*, 41(2), 372–383. <https://doi.org/10.1139/p63-039>
- Cabrera, R., Pannu, D. S., Caridi, J., Firpi, R. J., Soldevila-Pico, C., Morelli, G., Clark, V., Suman, A., George Jr., T. J., & Nelson, D. R. (2011). The combination of sorafenib with transarterial chemoembolisation for hepatocellular carcinoma. *Alimentary Pharmacology & Therapeutics*, 34(2), 205–213. <https://doi.org/10.1111/j.1365-2036.2011.04697.x>
- Chargari, C., Deutsch, E., Blanchard, P., Gouy, S., Martelli, H., Guérin, F., Dumas, I., Bossi, A., Morice, P., Viswanathan, A. N., & Haie-Meder, C. (2019). Brachytherapy: An overview for clinicians. *CA: A Cancer Journal for Clinicians*, 69(5), 386–401. <https://doi.org/10.3322/caac.21578>
- CIAAW. (2021). *Isotopic compositions of the elements*. Pure and Applied Chemistry.
- de Azevedo, M. de B. M., de Melo, V. H. S., Soares, C. R. J., Miyamoto, D. M., Katayama, R. A., Squair, P. L., Barros, C. H. N., & Tasic, L. (2018). Development and characterisation of polymeric microparticle of poly(D,L-lactic acid) loaded with holmium acetylacetonate. *Journal of Microencapsulation*, 35(3), 281–291. <https://doi.org/10.1080/02652048.2018.1477843>
- Dedukh, N. V., Makarov, V. B., & Pavlov, A. D. (2021). Polylactide-based biomaterial and its use as bone implants (analytical literature review). *PAIN, JOINTS, SPINE*, 9(1), 28–35. <https://doi.org/10.22141/2224-1507.9.1.2019.163056>
- Donahue, W., Bongiorno, P., Hearn, R., Rodgers, J., Nath, R., & Chen, Z. (2012). SU-E-T-112: Experimental Characterization of a Novel Thermal Reservoir for Consistent and Accurate Annealing of High-Sensitivity TLDs. *Medical Physics*, 39(6Part11), 3728–3729. <https://doi.org/10.1118/1.4735170>
- Elias, D., Cavalcanti, A., Sabourin, J. C., Lassau, N., Pignon, J. P., Ducreux, M., Coyle, C., & Lasser, P. (1998). Resection of liver metastases from colorectal cancer: the real impact of the surgical margin. *European Journal of Surgical Oncology (EJSO)*, 24(3), 174–179. [https://doi.org/10.1016/S0748-7983\(98\)92878-5](https://doi.org/10.1016/S0748-7983(98)92878-5)
- Endovascular Today. (2021, March 22). Sirtex Medical Receives FDA Approval to Conduct DOORwaY90 Study of SIR-Spheres in Unresectable HCC. *Endovascular Today*.
- Eriksson, D., & Stigbrand, T. (2010). Radiation-induced cell death mechanisms. *Tumor Biology*, 31(4), 363–372. <https://doi.org/10.1007/s13277-010-0042-8>
- Food and Drug Administration. (2021). *TheraSphere™ – P200029*. U.S Food and Drug Administration.
- Foyer, C. H. (1993). Ascorbic Acid. In *Antioxidants in Higher Plants* (1st ed.). CRC Press.

- Gaba, R. C., Lokken, R. P., Hickey, R. M., Lipnik, A. J., Lewandowski, R. J., Salem, R., Brown, D. B., Walker, T. G., Silberzweig, J. E., Baerlocher, M. O., Echenique, A. M., Midia, M., Mitchell, J. W., Padia, S. A., Ganguli, S., Ward, T. J., Weinstein, J. L., Nikolic, B., & Dariushnia, S. R. (2017). Quality Improvement Guidelines for Transarterial Chemoembolization and Embolization of Hepatic Malignancy. *Journal of Vascular and Interventional Radiology*, 28(9), 1210-1223.e3. <https://doi.org/10.1016/j.jvir.2017.04.025>
- Gianfaldoni, S., Gianfaldoni, R., Wollina, U., Lotti, J., Tchernev, G., & Lotti, T. (2017). An Overview on Radiotherapy: From Its History to Its Current Applications in Dermatology. *Open Access Macedonian Journal of Medical Sciences*, 5(4), 521–525. <https://doi.org/10.3889/oamjms.2017.122>
- Goode, J. A. (2004). Embolisation of cancer: what is the evidence? *Cancer Imaging*, 4(2), 133–141. <https://doi.org/10.1102/1470-7330.2004.0021>
- Hashikin, N. Ab. A., Yeong, C.-H., Abdullah, B. J. J., Ng, K.-H., Chung, L.-Y., Dahalan, R., & Perkins, A. C. (2015). Neutron Activated Samarium-153 Microparticles for Transarterial Radioembolization of Liver Tumour with Post-Procedure Imaging Capabilities. *PLOS ONE*, 10(9), e0138106. <https://doi.org/10.1371/journal.pone.0138106>
- Heinrich, S., & Lang, H. (2017). Hepatic resection for primary and secondary liver malignancies. *Innovative Surgical Sciences*, 2(1), 1–8. <https://doi.org/10.1515/iss-2017-0009>
- Hess, K. R., Varadhachary, G. R., Taylor, S. H., Wei, W., Raber, M. N., Lenzi, R., & Abbruzzese, J. L. (2006). Metastatic patterns in adenocarcinoma. *Cancer*, 106(7), 1624–1633. <https://doi.org/10.1002/cncr.21778>
- Heysel, C., Armstrong, A., Bennett, J., Werger, E., Naperstkow, Z., & Pasuta, R. (2018). CUSTOMIZED IRRADIATION SITES FOR MEDICAL ISOTOPE PRODUCTION. *Annual Conference of the Canadian Nuclear Society*, 1–15.
- IAEA. (2018). *Nuclear Data Sheets*. International Atomic Energy Agency.
- IAEA. (2010). *Atlas of Neutron Capture Cross Sections*. International Atomic Energy Agency.
- Ikemoto, T., Shimada, M., & Yamada, S. (2017). Pathophysiology of recurrent hepatocellular carcinoma after radiofrequency ablation. *Hepatology Research*, 47(1), 23–30. <https://doi.org/10.1111/hepr.12705>
- Iwatsuki, S., Dvorchik, I., Madariaga, J. R., Wallis Marsh, J., Dodson, F., Bonham, A. C., Geller, D. A., Gayowski, T. J., Fung, J. J., & Starzl, T. E. (1999). Hepatic resection for metastatic colorectal adenocarcinoma: a proposal of a prognostic scoring system. *Journal of the American College of Surgeons*, 189(3), 291–299. [https://doi.org/10.1016/S1072-7515\(99\)00089-7](https://doi.org/10.1016/S1072-7515(99)00089-7)
- Jia, Z., & Wang, W. (2018). Yttrium-90 radioembolization for unresectable metastatic neuroendocrine liver tumor: A systematic review. *European Journal of Radiology*, 100, 23–29. <https://doi.org/10.1016/j.ejrad.2018.01.012>
- Katz, S. C., Hardaway, J., Prince, E., Guha, P., Cunetta, M., Moody, A., Wang, L. J., Armenio, V., Espot, N. J., & Junghans, R. P. (2020). HITM-SIR: phase Ib trial of intraarterial chimeric antigen receptor T-cell therapy and selective internal radiation therapy for CEA+ liver metastases. *Cancer Gene Therapy*, 27(5), 341–355. <https://doi.org/10.1038/s41417-019-0104-z>
- Klaassen, N. J. M., Arntz, M. J., Gil Arranja, A., Roosen, J., & Nijssen, J. F. W. (2019a). The various therapeutic applications of the medical isotope holmium-166: a narrative review. *EJNMMI Radiopharmacy and Chemistry*, 4(1), 19. <https://doi.org/10.1186/s41181-019-0066-3>
- Klaassen, N. J. M., Arntz, M. J., Gil Arranja, A., Roosen, J., & Nijssen, J. F. W. (2019b). The various therapeutic applications of the medical isotope holmium-166: a narrative review. *EJNMMI Radiopharmacy and Chemistry*, 4(1), 19. <https://doi.org/10.1186/s41181-019-0066-3>

- Kopecky, J. (2001). *Atlas of Neutron Capture Cross Sections*. International Atomic Energy Agency Nuclear Data Section.
- Kulik, L. M., Atassi, B., van Holsbeeck, L., Souman, T., Lewandowski, R. J., Mulcahy, M. F., Hunter, R. D., Nemcek, A. A., Abecassis, M. M., Haines, K. G., & Salem, R. (2006). Yttrium-90 microspheres (TheraSphere®) treatment of unresectable hepatocellular carcinoma: Downstaging to resection, RFA and bridge to transplantation. *Journal of Surgical Oncology*, *94*(7), 572–586. <https://doi.org/10.1002/jso.20609>
- Künzli, B. M., Abitabile, P., & Maurer, C. A. (2011). Radiofrequency ablation of liver tumors: Actual limitations and potential solutions in the future. *World Journal of Hepatology*, *3*(1), 8. <https://doi.org/10.4254/wjh.v3.i1.8>
- LATHAM, R., & CASSELS, J. M. (1948). Scattering of Neutrons by Lead. *Nature*, *161*(4086), 282–283. <https://doi.org/10.1038/161282a0>
- Lobo, V., Patil, A., Phatak, A., & Chandra, N. (2010). Free radicals, antioxidants and functional foods: Impact on human health. *Pharmacognosy Reviews*, *4*(8), 118. <https://doi.org/10.4103/0973-7847.70902>
- Loo, J. S. C., Ooi, C. P., & Boey, F. Y. C. (2005). Degradation of poly(lactide-co-glycolide) (PLGA) and poly(L-lactide) (PLLA) by electron beam radiation. *Biomaterials*, *26*(12), 1359–1367. <https://doi.org/10.1016/j.biomaterials.2004.05.001>
- McCaffrey, J. P., Shen, H., Downton, B., & Mainegra-Hing, E. (2007). Radiation attenuation by lead and nonlead materials used in radiation shielding garments. *Medical Physics*, *34*(2), 530–537. <https://doi.org/10.1118/1.2426404>
- Milicevic, D., Trifunovic, S., Dojcilovic, J., Ignjatovic, N., & Suljovrujic, E. (2010). The influence of gamma radiation on the molecular weight and glass transition of PLLA and HAp/PLLA nanocomposite. *Nuclear Instruments and Methods in Physics Research, Section B: Beam Interactions with Materials and Atoms*, *268*(17–18), 2744–2749. <https://doi.org/10.1016/j.nimb.2010.06.036>
- Minami, Y. (2014). Therapeutic response assessment of RFA for HCC: Contrast-enhanced US, CT and MRI. *World Journal of Gastroenterology*, *20*(15), 4160. <https://doi.org/10.3748/wjg.v20.i15.4160>
- Moharram, B. M., Nagy, M. E., Shaat, M. K., El Sayed, A. R., Fayiz, M., Dwidar, S. A., & Dorrah, M. E. (2020). Performance of lead and iron oxides nanoparticle materials on shielding properties for γ -rays. *Radiation Physics and Chemistry*, *173*, 108880. <https://doi.org/10.1016/J.RADPHYSICHEM.2020.108880>
- Moore, S., Brookhaven National Laboratory, & U.S Atomic Energy Commission. (1968). *Optical model analysis of the elastic scattering of neutrons by the lead isotopes and bismuth at 0.5, 1.0, and 2.5 MeV*. Brookhaven National Laboratory.
- Murariu, M., & Dubois, P. (2016). PLA composites: From production to properties. *Advanced Drug Delivery Reviews*, *107*, 17–46. <https://doi.org/10.1016/j.addr.2016.04.003>
- Nakafuku, C., & Takehisa, S. Y. (2004). Glass transition and mechanical properties of PLLA and PDLLA-PGA copolymer blends. *Journal of Applied Polymer Science*, *93*(5), 2164–2173. <https://doi.org/10.1002/app.20687>
- Nakagawa, T., Chiba, S., Hayakawa, T., & Kajino, T. (2005). Maxwellian-averaged neutron-induced reaction cross sections and astrophysical reaction rates for $kT=1\text{keV}$ to 1MeV calculated from microscopic neutron cross section library JENDL-3.3. *Atomic Data and Nuclear Data Tables*, *91*(2), 77–186. <https://doi.org/10.1016/j.adt.2005.08.002>

- Nascimento, N., Hugo, V., Melo, S. De, & Kodama, Y. (2011). MICROSPHERES OF POLYESTHER LOADED WITH HOLMIUM-165 : EFFECT OF GAMMA IRRADIATION ON THE POLYMERIC STRUTURE. *International Nuclear Atlantic Conference - INAC 2011*.
- Nesmerak, K. (2013). Lanthanide/Actinide Toxicity. In *Encyclopedia of Metalloproteins* (pp. 1098–1103). Springer New York. https://doi.org/10.1007/978-1-4614-1533-6_151
- Nijsen, F., Rook, D., Brandt, C., Meijer, R., Dullens, H., Zonnenberg, B., de Klerk, J., van Rijk, P., Hennink, W., & van het Schip, F. (2001). Targeting of liver tumour in rats by selective delivery of holmium-166 loaded microspheres: a biodistribution study. *European Journal of Nuclear Medicine*, 28(6), 743–749. <https://doi.org/10.1007/s002590100518>
- Nijsen, J. F. W., Zonnenberg, B. A., Woittiez, J. R. W., Rook, D. W., Swildens-Van Woudenberg, I. A., Van Rijk, P. P., & Van het Schip, A. D. (1999). Holmium-166 poly lactic acid microspheres applicable for intra-arterial radionuclide therapy of hepatic malignancies: Effects of preparation and neutron activation techniques. *European Journal of Nuclear Medicine*, 26(7), 699–704. <https://doi.org/10.1007/s002590050440>
- Nijsen, J. F. W., Zonnenberg, B. A., Woittiez, J. R. W., Rook, D. W., Swildens-van Woudenberg, I. A., van Rijk, P. P., & van het Schip, A. D. (1999). Holmium-166 poly lactic acid microspheres applicable for intra-arterial radionuclide therapy of hepatic malignancies: effects of preparation and neutron activation techniques. *European Journal of Nuclear Medicine and Molecular Imaging*, 26(7), 699–704. <https://doi.org/10.1007/s002590050440>
- Nuszkiewicz, J., Woźniak, A., & Szewczyk-Golec, K. (2020). Ionizing Radiation as a Source of Oxidative Stress—The Protective Role of Melatonin and Vitamin D. *International Journal of Molecular Sciences*, 21(16), 5804. <https://doi.org/10.3390/ijms21165804>
- Prasad, S. G., De, A., & De, U. (2011). Structural and Optical Investigations of Radiation Damage in Transparent PET Polymer Films. *International Journal of Spectroscopy*, 2011, 1–7. <https://doi.org/10.1155/2011/810936>
- Raoul, J.-L., Forner, A., Bolondi, L., Cheung, T. T., Kloeckner, R., & de Baere, T. (2019). Updated use of TACE for hepatocellular carcinoma treatment: How and when to use it based on clinical evidence. *Cancer Treatment Reviews*, 72, 28–36. <https://doi.org/10.1016/j.ctrv.2018.11.002>
- Ray, P. D., Huang, B.-W., & Tsuji, Y. (2012). Reactive oxygen species (ROS) homeostasis and redox regulation in cellular signaling. *Cellular Signalling*, 24(5), 981–990. <https://doi.org/10.1016/j.cellsig.2012.01.008>
- Reinders, M. T. M., Smits, M. L. J., van Roekel, C., & Braat, A. J. A. T. (2019). Holmium-166 Microsphere Radioembolization of Hepatic Malignancies. *Seminars in Nuclear Medicine*, 49(3), 237–243. <https://doi.org/10.1053/j.semnuclmed.2019.01.008>
- Reinders, M. T. M., van Erpecum, K. J., Smits, M. L. J., Braat, A. J. A. T., Bruijne, J. de, Bruijnen, R., Sprengers, D., Man, R. A. de, Vegt, E., IJzermans, J. N. M., Moelker, A., & Lam, M. G. E. H. (2022). Safety and Efficacy of 166-Ho Radioembolization in Hepatocellular Carcinoma: The HEPAR Primary Study. *Journal of Nuclear Medicine*, 63(12), 1891–1898. <https://doi.org/10.2967/jnumed.122.263823>
- Rivaton, A., & Arnold, J. (2008). Structural modifications of polymers under the impact of fast neutrons. *Polymer Degradation and Stability*, 93(10), 1864–1868. <https://doi.org/10.1016/j.polymdegradstab.2008.07.015>
- Rumgay, H., Arnold, M., Ferlay, J., Lesi, O., Cabasag, C. J., Vignat, J., Laversanne, M., McGlynn, K. A., & Soerjomataram, I. (2022). Global burden of primary liver cancer in 2020 and predictions to 2040. *Journal of Hepatology*, 77(6), 1598–1606. <https://doi.org/10.1016/j.jhep.2022.08.021>

- Salem, R., Lewandowski, R. J., Atassi, B., Gordon, S. C., Gates, V. L., Barakat, O., Sergie, Z., Wong, C.-Y. O., & Thurston, K. G. (2005). Treatment of Unresectable Hepatocellular Carcinoma with Use of 90Y Microspheres (TheraSphere): Safety, Tumor Response, and Survival. *Journal of Vascular and Interventional Radiology*, 16(12), 1627–1639. <https://doi.org/10.1097/01.RVI.0000184594.01661.81>
- Sato, K. T., Lewandowski, R. J., Mulcahy, M. F., Atassi, B., Ryu, R. K., Gates, V. L., Nemcek, A. A., Barakat, O., Benson, A., Mandal, R., Talamonti, M., Wong, C.-Y. O., Miller, F. H., Newman, S. B., Shaw, J. M., Thurston, K. G., Omary, R. A., & Salem, R. (2008). Unresectable Chemorefractory Liver Metastases: Radioembolization with 90Y Microspheres—Safety, Efficacy, and Survival. *Radiology*, 247(2), 507–515. <https://doi.org/10.1148/radiol.2472062029>
- Singhvi, M. S., Zinjarde, S. S., & Gokhale, D. V. (2019). Polylactic acid: synthesis and biomedical applications. *Journal of Applied Microbiology*, 127(6), 1612–1626. <https://doi.org/10.1111/jam.14290>
- Sjoquist, K. M., Goldstein, D., & Bester, L. (2010). A Serious Complication of Selected Internal Radiation Therapy: Case Report and Literature Review. *The Oncologist*, 15(8), 830–835. <https://doi.org/10.1634/theoncologist.2010-0074>
- Smits, M. L., Nijssen, J. F., van den Bosch, M. A., Lam, M. G., Vente, M. A., Huijbregts, J. E., van het Schip, A. D., Elschot, M., Bult, W., de Jong, H. W., Meulenhoff, P. C., & Zonnenberg, B. A. (2010). Holmium-166 radioembolization for the treatment of patients with liver metastases: design of the phase I HEPAR trial. *Journal of Experimental & Clinical Cancer Research*, 29(1), 70. <https://doi.org/10.1186/1756-9966-29-70>
- Stubbs, R. (2001). Selective internal radiation therapy with 90yttrium microspheres for extensive colorectal liver metastases. *Journal of Gastrointestinal Surgery*, 5(3), 294–302. [https://doi.org/10.1016/S1091-255X\(01\)80051-2](https://doi.org/10.1016/S1091-255X(01)80051-2)
- Tanase, C. E., & Spiridon, I. (2014). PLA/chitosan/keratin composites for biomedical applications. *Materials Science and Engineering: C*, 40, 242–247. <https://doi.org/10.1016/j.msec.2014.03.054>
- Terumo. (2017). *Terumo Launches QuiremSpheres® Microspheres in Europe*.
- Tsilimigras, D. I., Brodt, P., Clavien, P.-A., Muschel, R. J., D’Angelica, M. I., Endo, I., Parks, R. W., Doyle, M., de Santibañes, E., & Pawlik, T. M. (2021). Liver metastases. *Nature Reviews Disease Primers*, 7(1), 27. <https://doi.org/10.1038/s41572-021-00261-6>
- Valery, P. C., Laversanne, M., Clark, P. J., Petrick, J. L., McGlynn, K. A., & Bray, F. (2018). Projections of primary liver cancer to 2030 in 30 countries worldwide. *Hepatology*, 67(2), 600–611. <https://doi.org/10.1002/hep.29498>
- van Nimwegen, S. A., Bakker, R. C., Kirpensteijn, J., van Es, R. J. J., Koole, R., Lam, M. G. E. H., Hesselink, J. W., & Nijssen, J. F. W. (2018). Intratumoral injection of radioactive holmium (166Ho) microspheres for treatment of oral squamous cell carcinoma in cats. *Veterinary and Comparative Oncology*, 16(1), 114–124. <https://doi.org/10.1111/vco.12319>
- Vente, M. a D. (2009). *Proefschrift - Preclinical studies on holmium-166 poly (L-lactic acid) microspheres for hepatic arterial radioembolization*.
- Vente, M. A. D., Nijssen, J. F. W., de Roos, R., van Steenberg, M. J., Kaaijk, C. N. J., Koster-Ammerlaan, M. J. J., de Lege, P. F. A., Hennink, W. E., van het Schip, A. D., & Krijger, G. C. (2009). Neutron activation of holmium poly(L-lactic acid) microspheres for hepatic arterial radioembolization: A validation study. *Biomedical Microdevices*, 11(4), 763–772. <https://doi.org/10.1007/s10544-009-9291-y>
- Vente, M. A. D., Nijssen, J. F. W., de Wit, T. C., Seppenwoolde, J. H., Krijger, G. C., Seevinck, P. R., Huisman, A., Zonnenberg, B. A., van den Ingh, T. S. G. A. M., & van het Schip, A. D. (2008).

- Clinical effects of transcatheter hepatic arterial embolization with holmium-166 poly(l-lactic acid) microspheres in healthy pigs. *European Journal of Nuclear Medicine and Molecular Imaging*, 35(7), 1259–1271. <https://doi.org/10.1007/s00259-008-0747-8>
- Wáng, Y. X. J., De Baere, T., Idée, J. M., & Ballet, S. (2015). Transcatheter embolization therapy in liver cancer: An update of clinical evidences. In *Chinese Journal of Cancer Research* (Vol. 27, Issue 2, pp. 96–121). AME Publishing Company. <https://doi.org/10.3978/j.issn.1000-9604.2015.03.03>
- Westcott, M. A., Coldwell, D. M., Liu, D. M., & Zikria, J. F. (2016). The development, commercialization, and clinical context of yttrium-90 radiolabeled resin and glass microspheres. *Advances in Radiation Oncology*, 1(4), 351–364. <https://doi.org/10.1016/j.adro.2016.08.003>
- World Health Organization. (2022, February). *Cancer*.
- Winkler, S. R., Eigl, R., Forstner, O., Martschini, M., Steier, P., Sterba, J. H., & Golser, R. (2015). Using the nuclear activation AMS method for determining chlorine in solids at ppb-levels and below. *Nuclear Instruments and Methods in Physics Research Section B: Beam Interactions with Materials and Atoms*, 361, 649–653. <https://doi.org/10.1016/j.nimb.2015.06.003>
- Yamazaki, I. M., Koskinas, M. F., Moreira, D. S., Semmler, R., Brancaccio, F., & Dias, M. S. (2020). Primary standardization and determination of gamma ray emission intensities of Ho-166: Disintegration rate and gamma-ray of Ho-166. *Applied Radiation and Isotopes*, 164(March 2019), 109237. <https://doi.org/10.1016/j.apradiso.2020.109237>
- Yoshino, H., & Kashiwakura, I. (2017). Involvement of reactive oxygen species in ionizing radiation-induced upregulation of cell surface Toll-like receptor 2 and 4 expression in human monocytic cells. *Journal of Radiation Research*, 58(5), 626–635. <https://doi.org/10.1093/jrr/rrx011>
- Zielhuis, S. W., Nijsen, J. F. W., Krijger, G. C., van het Schip, A. D., & Hennink, W. E. (2006). Holmium-Loaded Poly(L-lactic Acid) Microspheres: In Vitro Degradation Study. *Biomacromolecules*, 7(7), 2217–2223. <https://doi.org/10.1021/bm060230r>
- Zolotarev, K. I. (2009). EVALUATION OF CROSS-SECTION DATA FROM THRESHOLD TO 40-60 MeV FOR SPECIFIC NEUTRON REACTIONS IMPORTANT FOR NEUTRON DOSIMETRY APPLICATIONS. *International Nuclear Data Committee*.

8. Appendix A -Data

Gamma-Temperature Microsphere Data

21C 0kGy	total	damaged	Percentage	uncertainty
t=0	912	11	1.2%	0.001
t=24	901	22	2.4%	0.001
t=48	549	23	4.2%	0.002
t=72	559	26	4.7%	0.002
t=96	349	14	4.0%	0.003

average uncertainty
3.3% 0.014

21C 50 kGy	total	damaged	Percentage	uncertainty
t=0	729	15	2.1%	0.001
t=24	766	20	2.6%	0.001
t=48	431	18	4.2%	0.002
t=72	612	25	4.1%	0.002
t=96	899	30	3.3%	0.001

average uncertainty
3.3% 0.009

21C 100 kGy	total	damaged	Percentage	uncertainty
t=0	858	15	1.7%	0.001
t=24	557	14	2.5%	0.002
t=48	635	25	3.9%	0.002
t=72	872	36	4.1%	0.001
t=96	564	20	3.5%	0.002

average uncertainty
3.2% 0.010

21C 200 kGy	total	damaged	Percentage	uncertainty
t=0	786	13	1.7%	0.001
t=24	692	21	3.0%	0.001
t=48	427	19	4.4%	0.002
t=72	467	17	3.6%	0.002

t=96	286	10	3.5%	0.003
			average	uncertainty
			3.3%	0.010

21C 400 kGy	total	damaged	Percentage	uncertainty
t=0	474	13	2.7%	0.002
t=24	680	14	2.1%	0.001
t=48	680	23	3.4%	0.001
t=72	496	14	2.8%	0.002
t=96	483	23	4.8%	0.002
			average	uncertainty
			3.2%	0.010

21C 600 kGy	total	damaged	Percentage	uncertainty
t=0	488	10	2.0%	0.002
t=24	1058	34	3.2%	0.001
t=48	288	17	5.9%	0.003
t=72	402	28	7.0%	0.002
t=96	195	12	6.2%	0.005
			average	uncertainty
			4.9%	0.021

21C 800 kGy	total	damaged	Percentage	uncertainty
t=0	942	30	3.2%	0.001
t=24	538	23	4.3%	0.002
t=48	545	23	4.2%	0.002
t=72	361	26	7.2%	0.003
t=96	442	22	5.0%	0.002
			average	uncertainty
			4.8%	0.015

35C 0kGy	total	damaged	Percentage	uncertainty
t=0	894	13	1.5%	0.001
t=24	385	7	1.8%	0.003
t=48	842	16	1.9%	0.001
t=72	791	17	2.1%	0.001
t=96	641	14	2.2%	0.002

average uncertainty
 1.9% 0.002

35C 50 kGy	total	damaged	Percentage	uncertainty
t=0	564	8	1.4%	0.002
t=24	335	10	3.0%	0.003
t=48	985	19	1.9%	0.001
t=72	787	28	3.6%	0.001
t=96	555	21	3.8%	0.002

average uncertainty
 2.7% 0.010

35C 100 kGy	total	damaged	Percentage	uncertainty
t=0	408	7	1.7%	0.002
t=24	583	17	2.9%	0.002
t=48	789	17	2.2%	0.001
t=72	328	12	3.7%	0.003
t=96	576	14	2.4%	0.002

average uncertainty
 2.6% 0.007

35C 200 kGy	total	damaged	Percentage	uncertainty
t=0	456	7	1.5%	0.002
t=24	313	17	5.4%	0.003
t=48	367	9	2.5%	0.003

t=72	958	19	2.0%	0.001
t=96	473	15	3.2%	0.002
			average	uncertainty
			2.9%	0.015

35C 400 kGy	total	damaged	Percentage	uncertainty
t=0	583	8	1.4%	0.002
t=24	463	13	2.8%	0.002
t=48	549	14	2.6%	0.002
t=72	1182	40	3.4%	0.001
t=96	490	14	2.9%	0.002
			average	uncertainty
			2.6%	0.007

35C 600 kGy	total	damaged	Percentage	uncertainty
t=0	439	4	0.9%	0.002
t=24	290	11	3.8%	0.003
t=48	221	4	1.8%	0.005
t=72	319	23	7.2%	0.003
t=96	869	26	3.0%	0.001
			average	uncertainty
			3.3%	0.024

35C 800 kGy	total	damaged	Percentage	uncertainty
t=0	404	4	1.0%	0.002
t=24	224	5	2.2%	0.004
t=48	979	28	2.9%	0.001
t=72	360	13	3.6%	0.003
t=96	635	18	2.8%	0.002
			average	uncertainty
			2.5%	0.009

45C 0kGy	total	damaged	Percentage	uncertainty
t=0	258	8	3.1%	0.004
t=24	467	10	2.1%	0.002
t=48	649	22	3.4%	0.002
t=72	484	14	2.9%	0.002
t=96	387	10	2.6%	0.003
			average	uncertainty
			2.8%	0.005

45C 50 kGy	total	damaged	Percentage	uncertainty
t=0	377	24	6.4%	0.003
t=24	388	15	3.9%	0.003
t=48	551	22	4.0%	0.002
t=72	429	16	3.7%	0.002
t=96	310	12	3.9%	0.003
			average	uncertainty
			4.4%	0.011

45C 100 kGy	total	damaged	Percentage	uncertainty
t=0	602	19	3.2%	0.002
t=24	416	13	3.1%	0.002
t=48	666	21	3.2%	0.002
t=72	227	7	3.1%	0.004
t=96	509	11	2.2%	0.002
			average	uncertainty
			2.9%	0.004

45C 200 kGy	total	damaged	Percentage	uncertainty
t=0	310	10	3.2%	0.003
t=24	349	10	2.9%	0.003

t=48	342	13	3.8%	0.003
t=72	468	16	3.4%	0.002
t=96	482	13	2.7%	0.002
			average	uncertainty
			3.2%	0.004

45C 400 kGy	total	damaged	Percentage	uncertainty
t=0	707	32	4.5%	0.001
t=24	517	23	4.4%	0.002
t=48	451	20	4.4%	0.002
t=72	492	22	4.5%	0.002
t=96	720	23	3.2%	0.001
			average	uncertainty
			4.2%	0.006

45C 600 kGy	total	damaged	Percentage	uncertainty
t=0	352	7	2.0%	0.003
t=24	364	13	3.6%	0.003
t=48	252	10	4.0%	0.004
t=72	415	18	4.3%	0.002
t=96	479	19	4.0%	0.002
			average	uncertainty
			3.6%	0.009

45C 800 kGy	total	damaged	Percentage	uncertainty
t=0	459	10	2.2%	0.002
t=24	228	10	4.4%	0.004
t=48	293	14	4.8%	0.003
t=72	742	28	3.8%	0.001
t=96	208	7	3.4%	0.005
			average	uncertainty

3.7% 0.010

55C 0kGy	total	damaged	Percentage	uncertainty
t=0	1070	7	0.7%	0.001
t=24	576	12	2.1%	0.002
t=48	530	6	1.1%	0.002
t=72	893	8	0.9%	0.001
t=96	1146	8	0.7%	0.001

average uncertainty
1.1% 0.006

55C 50 kGy	total	damaged	Percentage	uncertainty
t=0	900	21	2.3%	0.001
t=24	2074	24	1.2%	0.000
t=48	1180	21	1.8%	0.001
t=72	620	14	2.3%	0.002
t=96	796	15	1.9%	0.001

average uncertainty
1.9% 0.005

55C 100 kGy	total	damaged	Percentage	uncertainty
t=0	1048	12	1.1%	0.001
t=24	570	11	1.9%	0.002
t=48	351	11	3.1%	0.003
t=72	908	21	2.3%	0.001
t=96	772	16	2.1%	0.001

average uncertainty
2.1% 0.007

55C 200 kGy	total	damaged	Percentage	uncertainty
t=0	1054	5	0.5%	0.001

t=24	378	5	1.3%	0.003
t=48	661	8	1.2%	0.002
t=72	977	15	1.5%	0.001
t=96	1060	9	0.8%	0.001

average uncertainty
1.1% 0.004

55C 400 kGy	total	damaged	Percentage	uncertainty
t=0	1029	25	2.4%	0.001
t=24	308	7	2.3%	0.003
t=48	491	18	3.7%	0.002
t=72	310	10	3.2%	0.003
t=96	866	23	2.7%	0.001

average uncertainty
2.8% 0.006

55C 600 kGy	total	damaged	Percentage	uncertainty
t=0	1244	14	1.1%	0.001
t=24	251	9	3.6%	0.004
t=48	678	19	2.8%	0.001
t=72	399	8	2.0%	0.003
t=96	528	14	2.7%	0.002

average uncertainty
2.4% 0.009

55C 800 kGy	total	damaged	Percentage	uncertainty
t=0	814	14	1.7%	0.001
t=24	869	11	1.3%	0.001
t=48	632	11	1.7%	0.002
t=72	818	15	1.8%	0.001
t=96	758	20	2.6%	0.001

		average	uncertainty	
		1.8%	0.005	
65C 0kGy	total	damaged	Percentage	uncertainty
t=0	458	22	4.8%	0.002
t=24	667	31	4.6%	0.001
t=48	481	30	6.2%	0.002
t=72	363	16	4.4%	0.003
t=96	355	18	5.1%	0.003
		average	uncertainty	
		5.0%	0.007	

65C 50 kGy	total	damaged	Percentage	uncertainty
t=0	324	22	6.8%	0.003
t=24	581	24	4.1%	0.002
t=48	211	14	6.6%	0.005
t=72	689	24	3.5%	0.001
t=96	402	36	9.0%	0.002
		average	uncertainty	
		6.0%	0.022	

65C 100 kGy	total	damaged	Percentage	uncertainty
t=0	401	23	5.7%	0.002
t=24	434	15	3.5%	0.002
t=48	260	19	7.3%	0.004
t=72	559	29	5.2%	0.002
t=96	670	40	6.0%	0.001
		average	uncertainty	
		5.5%	0.014	

65C 200 kGy	total	damaged	Percentage	uncertainty
t=0	369	28	7.6%	0.003

t=24	332	15	4.5%	0.003
t=48	205	17	8.3%	0.005
t=72	316	20	6.3%	0.003
t=96	649	81	12.5%	0.002
			average	uncertainty
			7.8%	0.030

65C 400 kGy	total	damaged	Percentage	uncertainty
t=0	817	139	17.0%	0.001
t=24	261	49	18.8%	0.004
t=48	353	100	28.3%	0.003
t=72	321	79	24.6%	0.003
t=96	325	156	48.0%	0.003
			average	uncertainty
			27.3%	0.124

65C 600 kGy	total	damaged	Percentage	uncertainty
t=0	412	70	17.0%	0.002
t=24	417	181	43.4%	0.002
t=48	897	813	90.6%	0.001
t=72	388	338	87.1%	0.003
t=96	231	213	92.2%	0.004
			average	uncertainty
			66.1%	0.341

65C 800 kGy	total	damaged	Percentage	uncertainty
t=0	785	91	11.6%	0.001
t=24	402	38	9.5%	0.002
t=48	254	68	26.8%	0.004
t=72	398	64	16.1%	0.003
t=96	179	34	19.0%	0.006

average uncertainty
 16.6% 0.068

75C 0kGy	total	damaged	Percentage	uncertainty
t=0	291	264	90.7%	0.003
t=24	334	306	91.6%	0.003
t=48	580	533	91.9%	0.002
t=72	363	321	88.4%	0.003
t=96	192	174	90.6%	0.005

average uncertainty
 90.7% 0.013

75C 50 kGy	total	damaged	Percentage	uncertainty
t=0	359	304	84.7%	0.003
t=24	235	179	76.2%	0.004
t=48	128	98	76.6%	0.008
t=72	515	413	80.2%	0.002
t=96	349	314	90.0%	0.003

average uncertainty
 81.5% 0.058

75C 100 kGy	total	damaged	Percentage	uncertainty
t=0	258	257	99.6%	0.004
t=24	100	100	100.0%	0.010
t=48	100	100	100.0%	0.010
t=72	100	100	100.0%	0.010
t=96	100	100	100.0%	0.010

average uncertainty
 99.9% 0.002

75C 200 kGy	total	damaged	Percentage	uncertainty
-------------	-------	---------	------------	-------------

t=0	202	195	96.5%	0.005
t=24	336	319	94.9%	0.003
t=48	183	173	94.5%	0.005
t=72	196	181	92.3%	0.005
t=96	245	230	93.9%	0.004
			average	uncertainty
			94.4%	0.015

75C 400 kGy	total	damaged	Percentage	uncertainty
t=0	378	372	98.4%	0.003
t=24	100	100	100.0%	0.010
t=48	100	100	100.0%	0.010
t=72	100	100	100.0%	0.010
t=96	100	100	100.0%	0.010
			average	uncertainty
			99.7%	0.007

75C 600 kGy	total	damaged	Percentage	uncertainty
t=0	210	188	89.5%	0.005
t=24	454	404	89.0%	0.002
t=48	364	319	87.6%	0.003
t=72	165	145	87.9%	0.006
t=96	304	284	93.4%	0.003
			average	uncertainty
			89.5%	0.023

75C 800 kGy	total	damaged	Percentage	uncertainty
t=0	100	100	100.0%	0.010
t=24	100	100	100.0%	0.010
t=48	100	100	100.0%	0.010
t=72	100	100	100.0%	0.010

t=96	100	100	100.0%	0.010
			average	uncertainty
			100.0%	0

100C 0kGy	total	damaged	Percentage	uncertainty
t=0	738	692	93.8%	0.001
t=24	384	376	97.9%	0.003
t=48	127	125	98.4%	0.008
t=72	100	100	100.0%	0.010
t=96	100	100	100.0%	0.010
			average	uncertainty
			98.0%	0.025

100C 50 kGy	total	damaged	Percentage	uncertainty
t=0	506	495	97.8%	0.002
t=24	434	430	99.1%	0.002
t=48	100	100	100.0%	0.010
t=72	100	100	100.0%	0.010
t=96	100	100	100.0%	0.010
			average	uncertainty
			99.4%	0.009

100C 100 kGy	total	damaged	Percentage	uncertainty
t=0	40	40	100.0%	0.025
t=24	100	100	100.0%	0.010
t=48	100	100	100.0%	0.010
t=72	100	100	100.0%	0.010
t=96	100	100	100.0%	0.010
			average	uncertainty
			100.0%	0

100C 200 kGy	total	damaged	Percentage	uncertainty
t=0	242	226	93.4%	0.004
t=24	318	311	97.8%	0.003
t=48	100	100	100.0%	0.010
t=72	100	100	100.0%	0.010
t=96	100	100	100.0%	0.010
			average	uncertainty
			98.2%	0.028

100C 400 kGy	total	damaged	Percentage	uncertainty
t=0	177	177	100.0%	0.006
t=24	100	100	100.0%	0.010
t=48	100	100	100.0%	0.010
t=72	100	100	100.0%	0.010
t=96	100	100	100.0%	0.010
			average	uncertainty
			100.0%	0

100C 600 kGy	total	damaged	Percentage	uncertainty
t=0	239	229	95.8%	0.004
t=24	283	271	95.8%	0.004
t=48	76	75	98.7%	0.013
t=72	100	100	100.0%	0.010
t=96	100	100	100.0%	0.010
			average	uncertainty
			98.1%	0.021

100C 800 kGy	total	damaged	Percentage	uncertainty
t=0	100	100	100.0%	0.010
t=24	100	100	100.0%	0.010

t=48	100	100	100.0%	0.010
t=72	100	100	100.0%	0.010
t=96	100	100	100.0%	0.010
			average	uncertainty
			100.0%	0

45C 400	total	damaged	Percentage	uncertainty
t=0	1230	37	3.0%	0.001
t=24	694	28	4.0%	0.001
t=48	473.5	13	2.7%	0.002
t=72	313	8	2.6%	0.003
t=96	292	14	4.8%	0.003
			average	uncertainty
			3.4%	0.010

45C 800	total	damaged	Percentage	uncertainty
t=0	1046.5	27	2.6%	0.001
t=24	1457.5	31	2.1%	0.001
t=48	438	23	5.3%	0.002
t=72	624.5	31	5.0%	0.002
t=96	482.5	5	1.0%	0.002
			average	uncertainty
			3.2%	0.018

55C 400	total	damaged	Percentage	uncertainty
t=0	786	60	7.6%	0.001
t=24	778	39	5.0%	0.001
t=48	579	18	3.1%	0.002
t=72	748	18	2.4%	0.001
t=96	548	26	4.7%	0.002
			average	uncertainty
			4.6%	0.020

55C 800	total	damaged	Percentage	uncertainty
t=0	476	22	4.6%	0.002
t=24	809	19	2.3%	0.001
t=48	474	20	4.2%	0.002
t=72	521	12	2.3%	0.002
t=96	499	16	3.2%	0.002

			average	uncertainty
			3.3%	0.011

60C 400	total	damaged	Percentage	uncertainty
t=0	895	56	6.3%	0.001
t=24	360	19	5.3%	0.003
t=48	255	13	5.1%	0.004
t=72	381	19	5.0%	0.003
t=96	324	24	7.4%	0.003
			average	uncertainty
			5.8%	0.010

60C 800	total	damaged	Percentage	uncertainty
t=0	815	36	4.4%	0.001
t=24	506	25	4.9%	0.002
t=48	342	15	4.4%	0.003
t=72	121	9	7.4%	0.008
t=96	188	9	4.8%	0.005
			average	uncertainty
			5.2%	0.013

65C 400	total	damaged	Percentage	uncertainty
t=0	462	102	22.1%	0.002
t=24	263	60	22.8%	0.004
t=48	357	52	14.6%	0.003
t=72	274	60	21.9%	0.004
t=96	306	50	16.3%	0.003
			average	uncertainty
			19.5%	0.038

65C 800	total	damaged	Percentage	uncertainty
t=0	384	358	93.2%	0.003
t=24	142	129	90.8%	0.007
t=48	66	64	97%	0.015
t=72	111	105	94.6%	0.009
t=96	79	72	91%	0.013
			average	uncertainty
			93.4%	0.025

70C 400	total	damaged	Percentage	uncertainty
t=0	969	832	85.9%	0.001
t=24	109	102	93.6%	0.009
t=48	47	43	91%	0.02
t=72	88	82	93%	0.01
t=96	71	66	93%	0.01
			average	uncertainty
			91.4%	0.032

70C 800	total	damaged	Percentage	uncertainty
t=0	105	103	98%	0.01
t=24	100	100	100%	0.01
t=48	100	100	100%	0.01
t=72	100	100	100%	0.01
t=96	100	100	100%	0.01
			average	uncertainty
			99.6%	0.009

75C 400	total	damaged	Percentage	uncertainty
t=0	100	100	1.00	0.01
t=24	100	100	1.00	0.01
t=48	100	100	1.00	0.01
t=72	100	100	1.00	0.01
t=96	100	100	1.00	0.01
			average	uncertainty
			100.0%	0

75C 800	total	damaged	Percentage	uncertainty
t=0	100	100	100%	0.01
t=24	100	100	100%	0.01
t=48	100	100	100%	0.01
t=72	100	100	100%	0.01
t=96	100	100	100%	0.01
			average	uncertainty
			100.0%	0

21C / 600	total	damaged	Percentage	uncertainty
Slow				
t=0	170	10	5.9%	0.006

t=24	340	16	4.7%	0.003
t=48	122	8	6.6%	0.008
t=72	340	26	7.6%	0.003
t=96	264	15	5.7%	0.004

average uncertainty
6.1% 0.01091818

21C / 600 Fast	total	damaged	Percentage	uncertainty
t=0	233	15	6.4%	0.004
t=24	318	22	6.9%	0.003
t=48	249	17	6.8%	0.004
t=72	288	13	4.5%	0.003
t=96	344	22	6.4%	0.003

average uncertainty
6.2% 0.00980476

45C/ 600 Slow	total	damaged	Percentage	uncertainty
t=0	196	14	7.1%	0.00510204
t=24	323	20	6.2%	0.00309598
t=48	340	21	6.2%	0.00294118
t=72	414	33	8.0%	0.00241546
t=96	333	24	7.2%	0.003003

average uncertainty
6.9% 0.00761261

45C / 600 Fast	total	damaged	Percentage	uncertainty
t=0	350	21	6.0%	0.00285714
t=24	418	22	5.3%	0.00239234
t=48	227	17	7.5%	0.00440529
t=72	251	13	5.2%	0.00398406
t=96	316	26	8.2%	0.00316456

average uncertainty
6.4% 0.01366053

55C/ 600 Slow	total	damaged	Percentage	uncertainty
t=0	231	10	4.3%	0.004329

t=24	209	12	5.7%	0.00478469
t=48	295	17	5.8%	0.00338983
t=72	291	15	5.2%	0.00343643
t=96	277	10	3.6%	0.00361011

average uncertainty
4.9% 0.00936133

55C/ 600 Fast	total	damaged	Percentage	uncertainty
t=0	345	23	6.7%	0.00289855
t=24	467	43	9.2%	0.00214133
t=48	197	11	5.6%	0.00507614
t=72	238	18	7.6%	0.00420168
t=96	247	16	6.5%	0.00404858

average uncertainty
7.1% 0.01372117

60C/ 600 Slow	total	damaged	Percentage	uncertainty
t=0	93	9	9.7%	0.01075269
t=24	236	14	5.9%	0.00423729
t=48	213	12	5.6%	0.00469484
t=72	256	16	6.3%	0.00390625
t=96	417	15	3.6%	0.00239808

average uncertainty
6.2% 0.02194343

60 C / 600 Fast	total	damaged	Percentage	uncertainty
t=0	350	17	4.9%	0.00285714
t=24	213	10	4.7%	0.00469484
t=48	285	16	5.6%	0.00350877
t=72	397	24	6.0%	0.00251889
t=96	510	18	3.5%	0.00196078

average uncertainty
4.9% 0.00965984

65C / 600 Slow	total	damaged	Percentage	uncertainty
t=0	210	25	11.9%	0.0047619

t=24	107	17	15.9%	0.00934579
t=48	297	38	12.8%	0.003367
t=72	233	31	13.3%	0.00429185
t=96	394	26	6.6%	0.00253807

average uncertainty
12.1% 0.03412511

65C / 600	total	damaged	Percentage	uncertainty
Fast				
t=0	253	25	9.9%	0.00395257
t=24	268	19	7.1%	0.00373134
t=48	203	29	14.3%	0.00492611
t=72	306	34	11.1%	0.00326797
t=96	293	31	10.6%	0.00341297

average uncertainty
10.6% 0.02582885

70C / 600	total	damaged	Percentage	uncertainty
Slow				
t=0	216	66	30.6%	0.00462963
t=24	88	43	48.9%	0.01136364
t=48	202	93	46.0%	0.0049505
t=72	192	87	45.3%	0.00520833
t=96	150	74	49.3%	0.00666667

average uncertainty
44.0% 0.07725493

70C / 600	total	damaged	Percentage	uncertainty
Fast				
t=0	311	186	59.8%	0.00321543
t=24	123	69	56.1%	0.00813008
t=48	242	119	49.2%	0.00413223
t=72	188	101	53.7%	0.00531915
t=96	219	107	48.9%	0.00456621

average uncertainty
53.5% 0.04659223

21 C / 1264	total	damaged	Percentage	uncertainty
t=0	329	35	0.10638298	0.00303951

t=24	188	135	0.71808511	0.00531915
t=48	87	71	0.81609195	0.01149425
t=72	NA	NA		
t=96	NA	NA		

average uncertainty
54.7% 0.38459322

60 C / 10 min	total	damaged	Percentage	uncertainty
t=0	452	28	6.2%	0.002
t=24	201	8	4.0%	0.005
t=48	306	14	4.6%	0.003
t=72	203	17	8.4%	0.005
t=96	522	25	4.8%	0.002

60 C / 30 min	total	damaged	Percentage	uncertainty
t=0	456	23	5.0%	0.002
t=24	438	24	5.5%	0.002
t=48	355	16	4.5%	0.003
t=72	242	13	5.4%	0.004
t=96	443	23	5.2%	0.002

60 C / 1 hr	total	damaged	Percentage	uncertainty
t=0	157	12	7.6%	0.006
t=24	336	16	4.8%	0.003
t=48	487	20	4.1%	0.002
t=72	377	21	5.6%	0.003
t=96	337	14	4.2%	0.003

65 c / 10 min	total	damaged	Percentage	uncertainty
t=0	266	20	7.5%	0.004
t=24	390	23	5.9%	0.003
t=48	372	19	5.1%	0.003
t=72	253	12	4.7%	0.004
t=96	362	26	7.2%	0.003

65 C / 30 min	total	damaged	Percentage	uncertainty
---------------	-------	---------	------------	-------------

t=0	198	19	9.6%	0.005
t=24	198	19	9.6%	0.005
t=48	280	21	7.5%	0.004
t=72	201	15	7.5%	0.005
t=96	271	18	6.6%	0.004

65 C / 1 hr	total	damaged	Percentage	uncertainty
t=0	144	16	11.1%	0.007
t=24	330	25	7.6%	0.003
t=48	533	29	5.4%	0.002
t=72	454	31	6.8%	0.002
t=96	459	15	3.3%	0.002

70 C / 10 min	total	damaged	Percentage	uncertainty
t=0	451	21	4.7%	0.002
t=24	426	26	6.1%	0.002
t=48	428	29	6.8%	0.002
t=72	181	13	7.2%	0.006
t=96	334	15	4.5%	0.003

70 C / 30 min	total	damaged	Percentage	uncertainty
t=0	156	18	11.5%	0.006
t=24	98	4	4.1%	0.010
t=48	403	21	5.2%	0.002
t=72	235	13	5.5%	0.004
t=96	542	36	6.6%	0.002

70 C / 1 hr	total	damaged	Percentage	uncertainty
t=0	262	19	7.3%	0.004
t=24	198	11	5.6%	0.005
t=48	407	26	6.4%	0.002
t=72	190	21	11.1%	0.005
t=96	400	33	8.3%	0.003

400 kGy in MSM	total	damaged	Percentage	uncertainty
t=0	252	7	2.8%	0.004

t=24	205	12	5.9%	0.005
t=48	222	12	5.4%	0.005

600 kGy in MSM	total	damaged	Percentage	uncertainty
t=0	421	69	16.4%	0.002
t=24	174	30	17.2%	0.006
t=48	351	47	13.4%	0.003

800 kGy in MSM	total	damaged	Percentage	uncertainty
t=0	278	16	5.8%	0.004
t=24	250	16	6.4%	0.004
t=48	279	24	8.6%	0.004

400 kGy in MSM with AA	total	damaged	Percentage	uncertainty
t=0	240	22	9.2%	0.004
t=24	219	26	11.9%	0.005
t=48	243	20	8.2%	0.004

600 kGy in MSM with AA	total	damaged	Percentage	uncertainty
t=0	255	12	4.7%	0.004
t=24	275	20	7.3%	0.004
t=48	232	19	8.2%	0.004

800 kGy in MSM with AA	total	damaged	Percentage	uncertainty
t=0	306	36	11.8%	0.003
t=24	220	21	9.5%	0.005
t=48	249	24	9.6%	0.004

ROS Testing

Ho(166)Cl ₃ 3.9 MBq/uL	total	mechanical damage	percentage	uncertainty
t=0	855	17	2.0%	0.001
t=24	462	10	2.2%	0.002
t=48	225	6	2.7%	0.004
t=72	476	27	5.7%	0.002
t=96	406	22	5.4%	0.002
t=120	214	15	7.0%	0.005
t=144	746	32	4.3%	0.001

Ho(165)Cl ₃ Control	total	mechanical damage	percentage	uncertainty	dimpling damage	percentage	uncertainty
t=0	370	5	1.4%	0.003	6	1.6%	0.003
t=24	275	9	3.3%	0.004	62	22.5%	0.004
t=48	297	8	2.7%	0.003	199	67.0%	0.003
t=72	180	6	3.3%	0.006	136	75.6%	0.006
t=96	148	3	2.0%	0.007	129	87.2%	0.007

Ho(166)Cl ₃ 2.2 MBq/uL in 1.0M AA	total	mechanical damage	percentage	uncertainty
t=0	528	5	0.9%	0.002
t=24	616	6	1.0%	0.002
t=48	443	4	0.9%	0.002
t=72	337	8	2.4%	0.003
t=96	294	4	1.4%	0.003

Ho(166)Cl ₃ 0.4 MBq/uL in 0.5 M AA	total	mechanical damage	percentage	uncertainty
t=0	305	8	2.6%	0.003
t=24	222	7	3.2%	0.005
t=48	232	4	1.7%	0.004
t=72	290	7	2.4%	0.003
t=96	253	6	2.4%	0.004

Ho(166)Cl ₃ 0.5 MBq/uL in 0.25 M AA	total	mechanical damage	percentage	uncertainty
t=0	147	5	3.4%	0.007
t=24	208	8	3.8%	0.005
t=48	188	6	3.2%	0.005
t=72	259	9	3.5%	0.004
t=96	250	7	2.8%	0.004

Ho(166)Cl ₃ 0.5 MBq/uL in 0.1 M AA	total	mechanical damage	percentage	uncertainty
t=0	386	6	1.6%	0.003
t=24	377	16	4.2%	0.003
t=48	427	7	1.6%	0.002
t=72	685	7	1.0%	0.001
t=96	351	5	1.4%	0.003

Ho(165)Cl ₃ 0.5 MBq/uL in 1.1 M AA Control	total	mechanical damage	percentage	uncertainty
t=0	275	3	1.1%	0.004
t=24	160	8	5.0%	0.006
t=48	265	10	3.8%	0.004
t=72	222	8	3.6%	0.005
t=96	151	10	6.6%	0.007

Double stack Test 1 -Immediate Suspension	total	damaged	%	uncert.
t=0	777	21	2.7%	0.001
t=24	442	15	3.4%	0.002
t=48	609	25	4.1%	0.002
t=72	1023	32	3.1%	0.001

Double stack Test 1 -Delayed Suspension	total	damaged	%	uncert.
t=0	986	44	4.5%	0.001
t=24	137	6	4.4%	0.007
t=48	355	18	5.1%	0.003

t=72	495	15	3.0%	0.002
t=96	652	41	6.3%	0.002

Double stack Test 2 -Immediate Suspension	total	damaged	%	uncert.
t=0	141	22	15.6%	0.007
t=24	220	16	7.3%	0.005
t=48	297	17	5.7%	0.003
t=72	422	28	6.6%	0.002
t=96	456	21	4.6%	0.002

Double stack Test 2 -Delayed Suspension	total	damaged	%	uncert.
t=0	562	49	8.7%	0.002
t=24	513	22	4.3%	0.002
t=48	251	14	5.6%	0.004
t=72	451	37	8.2%	0.002

Ho(166)Cl ₃ 2.02 MBq/uL	total	mechanical damage	percentage	uncertainty
t=0	200	7	3.5%	0.005
t=24	75	3	4.0%	0.013
t=48	146	4	2.7%	0.007
t=72	118	5	4.2%	0.008
t=96	135	9	6.7%	0.007
t=120	267	16	6.0%	0.004

Ho(166)Cl ₃ 3.8 MBq/uL	total	mechanical damage	percentage	uncertainty
t=0	105	4	3.8%	0.010
t=24	194	8	4.1%	0.005
t=48	188	10	5.3%	0.005
t=72	188	11	5.9%	0.005
t=96	135	12	8.9%	0.007
t=120	160	12	7.5%	0.006

Ho(166)Cl ₃ 3.3 MBq/uL	total	mechanical damage	percentage	uncertainty
---	-------	----------------------	------------	-------------

t=0	222	3	1.4%	0.005
t=24	193	7	3.6%	0.005
t=48	258	11	4.3%	0.004
t=72	258	11	4.3%	0.004
t=96	140	17	12.1%	0.007
t=120	117	13	11.1%	0.009

Ho(166)Cl ₃ 5.08 MBq/uL	total	mechanical damage	percentage	uncertainty
t=0	190	5	2.6%	0.005
t=24	93	4	4.3%	0.011
t=48	141	7	5.0%	0.007
t=72	145	10	6.9%	0.007
t=96	70	7	10.0%	0.014
t=120	71	8	11.3%	0.014

Ho(166)Cl ₃ 5.25 MBq/uL	total	mechanical damage	percentage	uncertainty
t=0	244	9	3.7%	0.004
t=24	64	3	4.7%	0.016
t=48	153	9	5.9%	0.007
t=72	98	4	4.1%	0.010
t=96	88	7	8.0%	0.011
t=120	70	10	14.3%	0.014

Ho(166)Cl ₃ 4.04 MBq/uL	total	mechanical damage	percentage	uncertainty
t=0	124	4	3.2%	0.008
t=24	95	3	3.2%	0.011
t=48	99	5	5.1%	0.010
t=72	99	5	5.1%	0.010
t=96	85	10	11.8%	0.012
t=120	130	14	10.8%	0.008

Pb Variable Thickness Rig

CoAl Wire Data -HPGe Counting
0.25 cm Pb

Co-Al	1173.1		1332.5		1368.44		2753.48	
P2	Net cps	Uncert (%)						
10 min	304.06	0.5	273.34	0.5	241.47	0.54	126.092	0.7

0.5 cm Pb

Co-Al	1173.1		1332.5		1368.44		2753.48	
P2	Net cps	Uncert (%)						
10 min	183.48	0.65	167.43	0.6	142.958	0.7	74.48	0.96

0.75 cm Pb

Co-Al	1173.1		1332.5		1368.44		2753.48	
P2	Net cps	Uncert (%)						
10 min	195.97	0.6	177.65	0.57	187.95	0.65	95.29	0.8

1.0 cm Pb

Co-Al	1173.1		1332.5		1368.44		2753.48	
P2	Net cps	Uncert (%)						
10 min	214.82	0.61	192.622	0.6	190.553	0.6	98.089	0.84

1.25 cm Pb

Co-Al	1173.1		1332.5		1368.44		2753.48	
P2	Net cps	Uncert (%)						
10 min	296.24	0.51	265.737	0.51	125.969	0.75	65.0975	1.03

Microsphere Data

0.25 cm Pb – SA 34.6

	total	damaged	Percentage	uncertainty
t=0	458	23	5.0%	0.002
t=24	377	24	6.4%	0.003
t=48	306	20	6.5%	0.003
t=72	261	18	6.9%	0.004

0.25 cm Pb -SA 33.7

	total	damaged	Percentage	uncertainty
--	-------	---------	------------	-------------

t=0	233	17	7.3%	0.004
t=24	268	27	10.1%	0.004
t=48	226	69	30.5%	0.004
t=72	40	30	75.0%	0.025
t=96	32	32	100.0%	0.031

0.25 cm Pb – Sa 26.9

	total	damaged	Percentage	uncertainty
t=0	190	5	2.6%	0.005
t=24	350	14	4.0%	0.003
t=48	219	8	3.7%	0.005
t=72	191	14	7.3%	0.005

0.25 cm Pb - SA 41.2

	total	damaged	Percentage	uncertainty
t=0	129	64	49.6%	0.008
t=24	126	95	75.4%	0.008
t=48	230	200	87.0%	0.004
t=72	166	135	81.3%	0.006
t=96	130	106	81.5%	0.008

0.5 cm Pb – SA 31.3

	total	damaged	Percentage	uncertainty
t=0	569	33	5.8%	0.002
t=24	361	15	4.2%	0.003
t=48	334	12	3.6%	0.003
t=72	321	17	5.3%	0.003

0.5 cm Pb – SA 26.4

	total	damaged	Percentage	uncertainty
t=0	854	24	2.8%	0.001
t=24	216	10	4.6%	0.005
t=48	386	16	4.1%	0.003
t=72	286	16	5.6%	0.003
t=96	706	35	5.0%	0.001

0.5 cm Pb – SA 41.7

	total	damaged	Percentage	uncertainty
--	-------	---------	------------	-------------

t=0	354	17	4.8%	0.003
t=24	581	30	5.2%	0.002
t=48	497	29	5.8%	0.002
t=72	485	82	16.9%	0.002

0.5 cm Pb – SA 34.7

	total	damaged	Percentage	uncertainty
t=0	221	15	6.8%	0.005
t=24	237	31	13.1%	0.004
t=48	252	16	6.3%	0.004
t=72	398	55	13.8%	0.003
t=96	331	46	13.9%	0.003

0.75 cm Pb – SA 27.7

	total	damaged	Percentage	uncertainty
t=0	308	14	4.5%	0.003
t=24	227	9	4.0%	0.004
t=48	251	11	4.4%	0.004
t=72	248	12	4.8%	0.004

0.75 cm Pb – SA 26.6

	total	damaged	Percentage	uncertainty
t=0	215	11	5.1%	0.005
t=24	456	19	4.2%	0.002
t=48	300	14	4.7%	0.003
t=72	366	18	4.9%	0.003
t=96	181	18	9.9%	0.006

0.75 cm Pb – SA 23.7

	total	damaged	Percentage	uncertainty
t=0	643	19	3.0%	0.002
t=24	223	8	3.6%	0.004
t=48	314	14	4.5%	0.003
t=72	591	29	4.9%	0.002

0.75 cm Pb – SA 36

	total	damaged	Percentage	uncertainty
t=0	270	65	24.1%	0.004

t=24	168	141	83.9%	0.006
t=48	125	109	87.2%	0.008
t=72	153	137	89.5%	0.007

1.0 cm Pb – SA 21.8

	total	damaged	Percentage	uncertainty
t=0	427	19	4.4%	0.002
t=24	166	11	6.6%	0.006
t=48	311	27	8.7%	0.003
t=72	152	12	7.9%	0.007
t=96	107	8	7.5%	0.009

1.0 cm Pb – SA24.6

	total	damaged	Percentage	uncertainty
t=0	237	13	5.5%	0.004
t=24	469	21	4.5%	0.002
t=48	242	15	6.2%	0.004
t=72	420	26	6.2%	0.002
t=96	406	26	6.4%	0.002

1.0 cm Pb – SA 20.6

	total	damaged	Percentage	uncertainty
t=0	184	7	3.8%	0.005
t=24	530	29	5.5%	0.002
t=48	387	75	19.4%	0.003
t=72	354	129	36.4%	0.003

1.0 cm Pb – SA 39.7

	total	damaged	Percentage	uncertainty
t=0	213	194	91.1%	0.005
t=24	227	212	93.4%	0.004
t=48	291	279	95.9%	0.003
t=72	100	96	96.0%	0.010

1.25 cm Pb – SA 33.2

	total	damaged	Percentage	uncertainty
t=0	240	7	2.9%	0.004

t=24	234	11	4.7%	0.004
t=48	383	19	5.0%	0.003
t=72	372	34	9.1%	0.003
t=96	191	25	13.1%	0.005

1.25 cm Pb – SA 58.4

	total	damaged	Percentage	uncertainty
t=0	467	31	6.6%	0.002
t=24	290	135	46.6%	0.003
t=48	355	323	91.0%	0.003
t=72	224	206	92.0%	0.004

1.25 cm Pb – SA 30.6

	total	damaged	Percentage	uncertainty
t=0	504	20	4.0%	0.002
t=24	477	20	4.2%	0.002
t=48	464	21	4.5%	0.002
t=72	385	22	5.7%	0.003
t=96	478	22	4.6%	0.002